Estimation of Effective Thermal Conductivity of Graphite flakes/Al Composites by Using Two-Dimensional Microstructure Images

（二次元微細組織画像を用いたグラファイトフレーク/ Al 複合材料の有効熱伝導率の推定）

Department of Mechanical Science and Engineering
Graduate School of Engineering
Hiroshima University, Japan

Advisor: Prof. Kenjiro Sugio

Zhao Yan

CONTENTS

Chapter 1 Background and Objective

Chapter 2 Fabrication and Thermal Properties of GFs/Al composites

Chapter 3 Relationship between the thermal conductivity of GFs in 3D and 2D microstructure images

Chapter 4 Effect of the orientation of GFs and interfacial thermal resistance on the effective thermal conductivity of GFs/Al composites

List of Figures

Figure 3-10. A SEM image of the microstructure at the Al-GFs interface.

Figure 4-1. The shape of the sample sintered by SPS; P1, P2, and P3 at the A plane denotes the regions corresponding to the optical micrographs. The grey arrow illustrates that the heat flow was from B to D during ETC measurement, C is the plane bearing the pressure during sintering.

Figure 4-2. Schematic diagram of heat flow at the interface. The dashed line denotes the Al–GF interface, q^{n} denotes the heat flow in the direction of the dashed arrows.

Figure 4-3 Simulation model for the ETC calculation.

Figure 4-4 TC of GFs as a function of the angle (θ). The nominal TC of the Al matrix, λ_{Al}, was 236 W m^{-1} K^{-1} (grey horizontal dotted line).

Figure 4-5 Optical micrographs of Samples 1–4. Regions P1, P2, and P3 correspond to the black circles at the A-plane in Figure 1. The grey arrow represents the heat flow direction during the ETC measurements. The brighter phases correspond to the Al matrix, and the elongated dark phases to the GFs.

Figure 4-6 Distribution of the GF orientations in the Al matrix. Gray and white rectangles in (a) and (b) represented the smallest circumscribed rectangles and were used to measure the angle (θ) between the basal plane of GFs and the heat flow direction; in case $-90 < \theta < 0$, θ was taken as the absolute value.

Figure 4-7 TC values of GFs in Samples1-4. Regions denoted as P1, P2, and P3 correspond to the microstructures in Figure 5; the color bar shows the TCs of GFs in different orientations.

Figure 4-8 ETCs of the composite samples. λ_{eff} denotes the measured ETC, λ_{ROM} is the ETC calculated using the rule of mixture, and $\lambda_{s\text{-}eff}$ is the ETC calculated using the 2D image-based simulation considering GF orientations.

Figure 4-9 ETC as a function of the heat transfer coefficient, *h*. The dashed lines represent the experimental ETCs, and the arrows denote the *h* value at the Al-GF interface.

List of Tables

Chapter 1

Background and Objective

1.1 Introduction

Today is an era of the rapid development of electronic technology. As shown in Figure 1-1, various electronic products are gradually integrated into people's daily lives, making people's lives convenient, comfortable, and safe. Therefore, ensuring the electronic products' efficiency, stability, and safety is essential to people's lives.

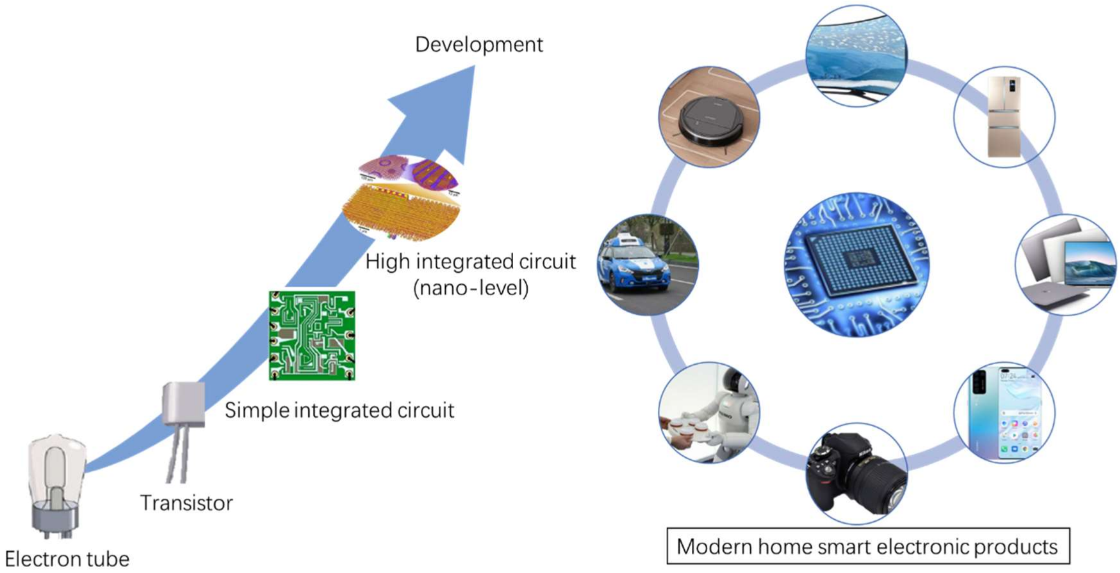

Figure 1-1 The development of microelectronics and modern smart products.

However, with the rapid development of electronic technology in the direction of high power, high frequency, miniaturization, and integration, the heat generated by the increase in the power density of electronic components is increased dramatically. As a result, the generated heat would heat electronic components, affecting their working effectiveness and life span, and even resulting in a malfunction of the device if not dissipation in time[1]. In other words, the mismatch in the heat dissipation performance and the thermal expansion coefficient between the materials used to make the components cause the electronic components' damage and failure. The key to solving this problem is to develop new electronic materials with high thermal conductivity (TC) and lower coefficient of thermal expansion (CTE) [2]. Semiconductors are the core component of electronic products; hence, electronic packaging materials must match thermal properties to semiconductors. Table 1-1 lists the thermal properties of semiconductors materials.

Table 1-1 thermal properties of semiconductor materials [1, 3-5].

Materials	Density / g·m^{-3}	TC / W·m^{-1}·K^{-1}	CTE /10^{-6} /K^{-1}
Silicon (Si)	2.3-2.34	139-150	2.8-4.2
Silicon carbide (SiC)	3.1-3.21	80-490	2.8-5.0
Gallium arsenide (GaAs)	5.3	46-58	5.8-5.9
Gallium nitride (GaN)	6.1	150	3.2

Traditional electronic packaging materials contain metals, ceramics, and composite materials. Table1-2 shows the TC and CTE of traditional electronic packaging materials. However, the traditional electronic packaging materials, such as Copper (Cu), Argentum (Ag), Aurum (Au), Alumina (Al_2O_3), W-Cu, etc., all have high density or high TC or high CTE. As a result, they can no longer meet electronic products' current comprehensive development requirements, such as high integration, efficient heat dissipation, and green environmental protection[6, 7].

Table 1-2 thermal properties of traditional electronic packaging materials.

Materials	Density / g·m^{-3}	TC / W·m^{-1}·K^{-1}	CTE /10^{-6} /K^{-1}
Al	2.7	236	23.0
Cu	8.9	400	17.0
Ag	10.49	429	18.9
Au	19.3	318	14.2
Al_2O_3	3.9	20	6.5-6.7
BeO	2.9	250-275	6.7-8.0
SiC	3.2	270	4.5
AlN	3.3-4.5	220	3.3-4.5
W-Cu	8.4	167	6.5
Mo-Cu		220-270	7.9-9.3

To cater for the future development characteristics of electronic products: e.g., high integration of integrated circuits and the miniaturization, portability, efficiency, high power, high stability, and low cost, the new generation of electronic packaging materials is required to have the following mechanical and thermal properties [8]:

1, High TC: Timely homogenize and dissipate the heat generated by the semiconductor.

2, Low CTE: Reduce the thermal stress between the semiconductor and electronic packaging materials.

3, Sufficient strength, stiffness, and toughness: Play a good role in supporting and protecting semiconductors and devices.

4, Lightweight: The density is as low as possible to facilitate the lightweight design of the device structure.

5, Cost control and competitive requirements: high yield, suitable for mass production, low price.

Metal-matrix composites have a high TC, low expansion of non-metallic reinforcement, easy processing of metal-matrix, and good plastic toughness. Therefore, metal matrix composites have attracted significant attention from researchers. Al is of low density, low cost, and high TC, and it is the commonly used metal matrix of the composites. The reinforcements include mainly carbon materials (carbon fiber, graphite, diamond), silicon carbide particles (SiC), silicon particles (Si), etc. Table 1-3 shows the TC, CTE, and density of those reinforcements.

SiC/Al, Si/Al, Diamond/Al are the most mature metal matrix composites. These composites have been widely used in the world and have gradually replaced the traditional electronic packaging materials. However, the metal matrix composites currently used in electronic packaging, e.g., SiC/Al, Si/Al, Diamond/Al, show high prices and TC lower than expected in large-scale industrial production. Figure 1-2 shows the density, TC, and CTE of the composites used in electronic packaging.

Table 1-3 Thermal properties of reinforcements[1, 7, 9-11].

Materials	**Density/ g·cm^{-3}**	**TC / W·m^{-1}·K^{-1}**	**CTE / 10^{-6}/ K**
Carbon fiber	1.75 ~ 2.19	530-1200	-1.45 ~ 7
Graphite	2.23	~3000 (*xy*) 6 ~ 38 (*z*)	-1.5 ~ -1.0 (*xy*) 29 (*z*)
Diamond	3.51	~2500	1.3
SiC	3.2	270	4.5
Si	2.3	150	4.1
BeO	2.9	250	6.7

Where a and b: the TC and ETC could be less than those of crystalline graphite due to the defects and impurities.

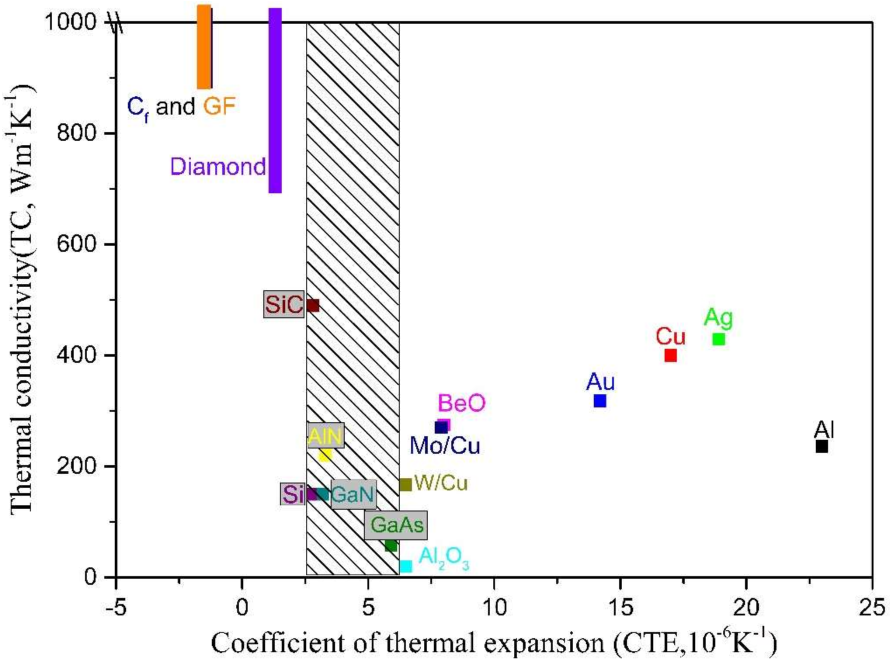

Figure 1-2 TC as a function of CTE for composites.

It is fortunate that carbon fibers and graphite flakes also have excellent thermal properties and are low-cost. Particularly for graphite flake, their TCs are values (~2200, ~38) W m^{-1} K^{-1} [9, 12, 13] in the basal-plane and the out-plane, respectively, and their CTE are (- 1.0, 8) × 10^{-6} K^{-1} [10, 14, 15] in the basal-plane and the out-plane, respectively. In view of GFs' excellent thermal properties, GFs/Al composites are considered to be one of the most promising candidates for electronic packaging. Many experimental studies of the effective thermal conductivity (ETC) of GFs/Al composites have been conducted extensively, e.g., Chen et al. [14] reported that the ETC of 80 vol.% GFs/Al composites (783 W m^{-1} K^{-1}) was higher than that of 80 vol.% diamond/copper composites [16] (724 W m^{-1} K^{-1}). Li et al. [17] reported that the ETC of 70 vol.% GFs (graphite flakes)/Al composite was 714 W m^{-1} K^{-1} in the plane parallel to the GFs layers. Comparison with SiC/Al, Si/Al, Diamond/Al composites, GFs/Al composites show higher TC, lower CTE, lower cost, and better machining performance. However, the ETC of GFs/Al composites is not high as the expected theoretical value due to the following deficiencies[10, 18-21]:

(1) GFs show strong anisotropic TC, resulting in the orientation of GFs has a great effect on the effective thermal conductivity (ETC) of GFs/Al composites.

(2) Interface reaction can occur readily during the fabricating process of GFs/Al composites, and the harmful formation of Al_4C_3 is often observed at the GFs-Al interface. The Al_4C_3 is a brittle compound, and it can reduce the plasticity of the composites and promote accelerated fatigue crack growth rates.

(3) The interfacial thermal resistance at the interface between GFs and Al considerably affects composites' ETC.

Additionally, to predict the ETC of composites, many theoretical models are proposed in previous studies [10, 11, 13, 14, 17, 18, 22-32]. However, those theoretical models are not suitable for calculating the ETC of GFs/Al composites due to the diversity orientation of the GFs in composites. Moreover, to evaluate the interfacial thermal resistance at the GFs-Al interface, the commonly used methods include the phonon diffuse mismatch model (DMM) [33], acoustic mismatch model (AMM)[34], etc. However, those models are based on an idea interface to calculate interfacial thermal resistance. In reality, the contact interface microstructure of two solids is extremely complex. Contact interfaces are affected by many factors, such as the thermophysical properties, the hardness, shape, roughness of the material, the gap at the interface, the roughness of the contact interface, as well as the pressure and temperature during composite fabrication. Furthermore, it is almost impossible to obtain the direct relationship between those influence factors and the contact interface microstructure. Thus, those models have specific limitations for calculating interface thermal resistance, and they are not entirely reliable for calculating interfacial thermal resistance.

This study reviews many previous studies on the ETC of GFs/Al composites and develops a new method to calculate the ETC of GFs/Al composites. Research method: a newly developed two-dimensional image-based model. Research contents: 1, Comparing the thermal conductivity of GFs in the 3D model and the 2D model, and determining the relationship between the thermal conductivity of GFs in the 3D model and the 2D model; 2, Study the effect degrees of orientation of GFs and interfacial thermal resistance on the effective thermal conductivity of GFs/Al composites using two-dimensional image-based simulations.

1.2 Experimental research on ETC of GFs/Al composites

1.2.1 Fabrication methods of GFs/Al composites

Metal matrix composites can be fabricated via a variety of methods like stir casting, squeeze casting, ultrasonic infiltration, pressure infiltration, spark plasma sintering, and hot pressing, etc. However, not all fabrication techniques are suitable for fabricating GFs/Al composites since there are some challenges to overcome, such as the oriented GFs, avoiding the formation of Al_4C_3, and reducing the interfacial thermal resistance. In this part, some common methods for fabricating GFs/Al composites are reviewed, along with their advantages and disadvantages. The fabrication methods can be classified into two routes: powder metallurgy process and liquid metallurgy process.

1.2.1.1 Powder Metallurgy Processing

The powder metallurgy process (PMP) is a low-temperature sintering technology that can effectively inhibit the interfacial reaction and the formation of Al_4C_3. The PMP methods can be divided into spark plasma sintering (SPS) [35-37] and vacuum hot pressing[14, 23, 26, 27]. Figure 1-3 shows the schematic diagram for SPS and vacuum hot pressing.

The process of using the PMP methods to prepare GFs/Al composites is to fill the mixtures of raw materials Al and GFs into a graphite mold for sintering. Some techniques in past studies were proposed to ensure GFs have a consistent orientation in composites. Such as that, to stack the GFs by layers, Chen et al. [14] tapped the graphite mold while filling naturally; Xue et al. [26] used a shaking device to vibrate the graphite mold filled with mixtures of Al and GFs, hoping to obtain the oriented GFs; Huang et al. [23] fill the graphite mold with layers of artificial graphite films, and Al foils, the orientation of graphite film and Al foil can be well controlled.

The formation of Al_4C_3 at the GFs-Al interface is thermodynamically favorable, and it can damage the mechanical and thermal properties. To avoid the formation of Al_4C_3, Chen et al. [14] used some approaches, including a lower temperature than melting point of Al during the hot-pressing process, and GFs with nearly 100% graphitization degree and a larger flat surface, to prevent the formation of Al_4C_3. Salvo [38] and Candan et al.[39] filled a certain minimum critical Si content to prevent the formation of Al_4C_3. Similarly, Xue et al. [26] coated GFs surface with Si to prevent the formation of Al_4C_3, and Kurita et al.[27] added Al-$Si_{11.3at\%}$ alloy into the raw materials Al powders to avoid the formation of Al_4C_3 during fabricated GFs/Al composites. The introduction of silicon not only prevents the formation of Al_4C_3, but silicon can effectively fill the pores at the interface between aluminum and graphite. Meanwhile, the disadvantages of the introduction of silicon were also revealed, which caused the microstructure of GFs to disarray in proximity to the GFs-Al interface, which can weaken the interlaminar strength between GF in proximity to the Al/GF interface and Al/GF interface [27].

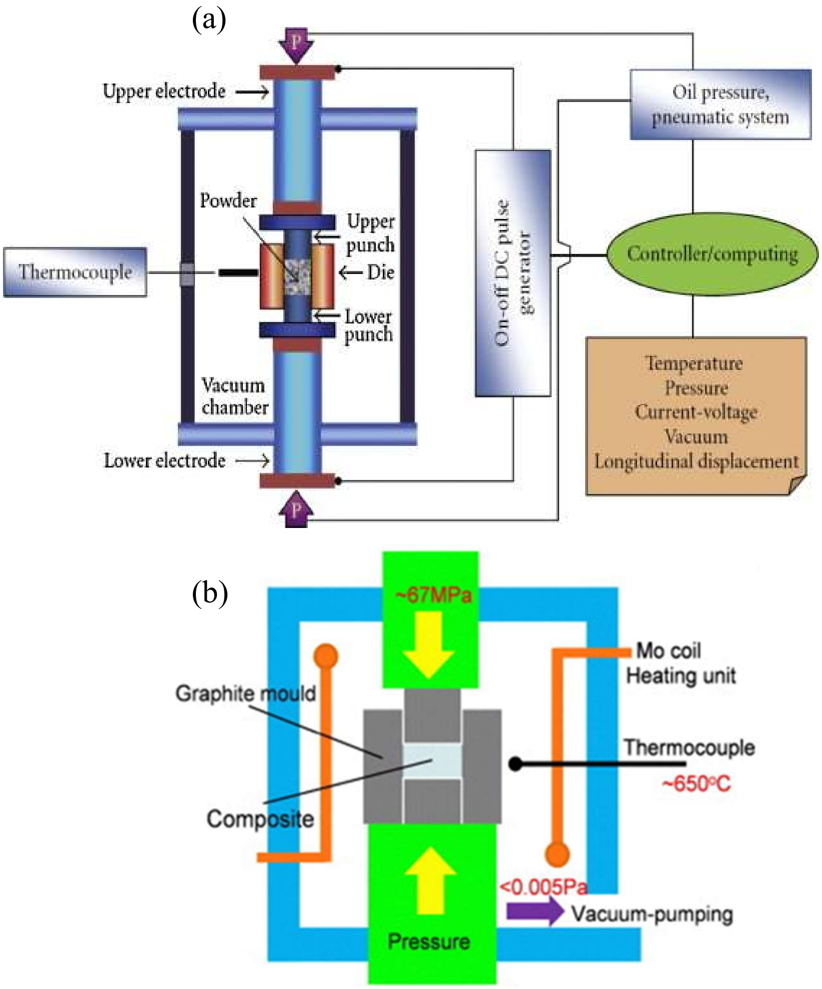

Figure 1-3 Schematic diagram for (a) spark plasma sintering [40], (b) vacuum hot pressing[41].

1.2.1.2 Liquid metallurgy processing

The liquid metallurgy process is also widely used to fabricate GFs/Al composites. The commonly used methods include gas pressure infiltration [11, 13, 31] and squeeze casting [17, 28, 29]. Figure 1-4 shows the schematic diagram of gas pressure infiltration and squeeze casting.

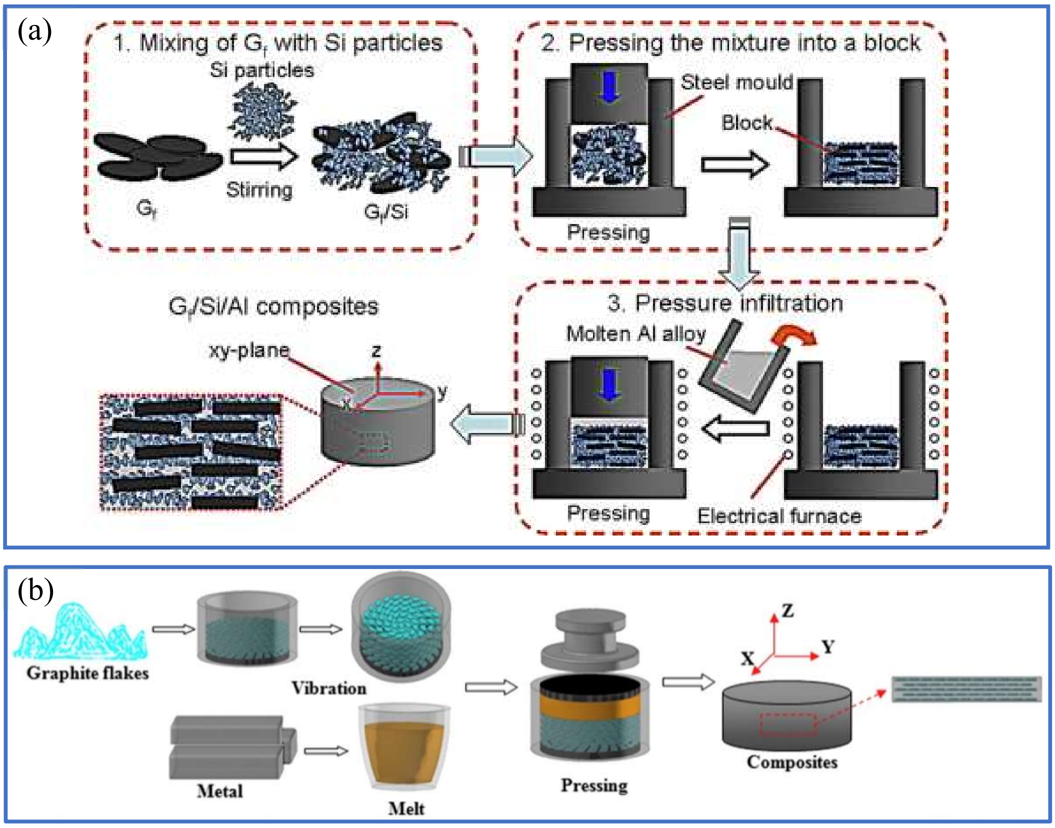

Figure 1-4 Schematic diagram of the fabrication process of GFs/Al composites, (a) gas pressure infiltration method [11], (b) squeeze casting method [17].

The common features of gas pressure infiltration and squeeze casting in GF/Al composite fabrication are: First, it is to put the raw material GFs into a mold and press GFs into preforms; Then, the molten Al is poured into a preheated mold containing the GFs preforms, and apply pressure to infiltrate the molten Al into the preforms. As a result, GFs are able to achieve uniform orientations through the fabrication of GFs preforms, and as reported in the papers [11, 13, 17, 28, 29], GFs were stacked by layers in GFs/Al composites.

As known that high temperature is an essential condition for liquid metallurgy to improve the fluidity of molten Al, but conversely, it promotes the interface reaction as well. According to Okura's studies [42] on the rate of formation of intermetallic compounds in Al matrix-carbon fiber composites, the interface reaction rate can be evaluated by: $X = [2kt\cdot exp(-Q/RT)]^{1/2}$. X is the thickness of Al_4C_3 reaction layer, k is a constant, t is heating time, Q is the activation energy, and T is temperature. The formula shows that the formation of Al_4C_3 is related to the temperature T and the heating time t. Consequently, the rapid cooling method[17, 29, 31] in the pressure infiltration process and squeeze casting process is one of the most used methods to suppress the formation of Al_4C_3. In addition, coating Si on the surface of GFs, or mixing a small amount of Si with raw GFs, or replacing pure aluminum with Al-Si alloys are also often used to prevent the formation of Al_4C_3 [11, 13, 20, 28, 29].

1.2.2 Problems of previous studies

Lots of experimental studies, as mentioned above 1.2.1 and 1.2.2, have tried to conquer the problems of the orientation of GFs and the formation of Al_4C_3. But the measured ETCs of GFs/Al composites were not as high as the expected theoretical ETC. It is evident that the high TC of GFs cannot be fully utilized in GFs/Al composites. The reasons can be analyzed from the following aspects.

Firstly, it is the method to control the orientation of GFs. The vibration method is often used to obtain oriented GFs in powder metallurgy processing. However, it is almost impossible to ensure that all the graphite flakes are entirely parallel to each other by vibrating the mold containing the mixtures of Al and GFs. Moreover, the pressure applied during the thermoforming process is usually given along one direction, the orientations of GFs cannot be well controlled, and angles between GFs basal-plane and the surface of GFs/Al composites are easy to form. Therefore, for the GFs/Al composites with a high-volume fraction of Gfs, it is more difficult to control GFs orientation by the vibration method. In the liquid metallurgy processing, obtaining the oriented GFs is to pre-press the GFs into a preform. However, the infiltration process of molten Al is challenging because the distance between GFs is minimal. Especially the prefabricated GFs preforms with a preferred orientation, and there is almost no space between GFs[10, 11, 13, 14, 17, 29]. In order to enhance the infiltration process, the third phases (SiC particles, Si particles, and short carbon fiber) were added into GFs preforms[10, 11, 13, 29, 43-46]. But the third phase would reduce the ETC of GFs/Al composites due to the low TC of the third phase itself, and it may destroy the parallel stacking of GFs in the preform.

Secondly, it is the approach to avoid the formation of Al_4C_3. There are two approaches used usually in experiments: 1 using highly graphitized GF and low sintering temperature.; 2 introducing the third phase (Si or SiC). However, according to Huang [23] and Kurita et al. [27], low sintering temperature can cause low density and more pores embedded in GFs/Al composites. The pores can reduce the ETC of composites [47]. In addition, the low TC of the third phase (Si or SiC) also lowers the ETC of GFs/Al composites.

Thirdly, it is the effect of interfacial thermal resistance on the ETC of composites. Many studies have proposed that the interfacial thermal resistance between carbon and Al dramatically affects the ETC of composites [13, 23, 29, 31, 48-54]. Besides, previous studies have investigated the effects of the shape [55-57] and size [14, 17, 18, 52, 53, 58, 59] of enhanced phase on the ETC of composites. For example, according to the studies of the effect of particle size on the ETC, the smaller filler particles can result in a lower ETC of composites because they caused a more extensive interface area [14, 17, 18].

1.3 Theoretical research on interfacial thermal resistance

Interfacial thermal resistance is derived from the Kapitsa[60] thermal resistance discovered in 1941. Interfacial thermal resistance is defined as the ratio of the temperature discontinuity at the interface to the power per unit area flowing across that interface [33]. Up to now, lots of scholars have studied the interface thermal resistance [33, 34, 61-71].

To determine interfacial thermal resistance, the commonly used experimental methods include steady-state measurement[72-74], transient measurement (such as laser photothermal measurement[75, 76] and photoacoustic method[77-79], thermal imaging method[72], “flash” flash method[80, 81], etc.), and micro/nano-scale measurement methods (such as transient thermoreflectance (TTR) technology and 3ω method [33, 82, 83]. However, those measurements are very strict, and the measurement results are not accurate enough because those measurements are susceptible to many external factors.

Therefore, many theoretical models are developed to predict interfacial thermal resistance, and interface thermal resistance is evaluated mainly from macro and micro perspectives.

1.3.1 Macro theory

At the macroscopic level, the interfacial thermal resistance comes from the incomplete contact of the material interface [84, 85]. The interfacial thermal resistance, R_c, can be expressed by $R_c = R_d + R_L$. R_d is the thermal resistance caused by heat diffusion and heat shrinkage resistance at the contact interface, R_L is the thermal resistance of the contact area at the contact interface [86]. Microstructure at the contact interface dominates the interfacial thermal resistance. However, the microstructure at the contact interface is affected by many factors, such as surface roughness, microscopic morphology, elastoplastic deformation of surface peaks, and stages in the surfaces of contact materials. Based on those influencing factors, some theoretical methods have been proposed to calculate interface thermal resistance, including CMY plastic contact model [61, 86], Multi-scale contact model [87, 88], Monte-Carlo simulation[89], Micro-scale contact model [90], etc. But those macroscopic models and simulations all have specific usage restrictions due to the complexity of the interface microstructure.

1.3.2 Micro theory

At the micro-level, heat is transferred by phonons, electrons, and photons. Therefore, the calculation mechanism of interfacial thermal resistance is to calculate phonon and electron couplings. In the past decades, different microscale models were proposed to predict interfacial thermal resistance. The common models include interfacial layer model (ILM) [91, 92], AMM model[34], DMM model and Boltzmann mesoscopic simulation[68].

ILM model considers that the contact interface consists of subsurface layers on the two sides of the contact interface and the middle contact interface layer. The thickness of the subsurface layer is 1 micron. At the contact interface, hot carriers transfer energy in the form of radiation. The subsurface layer is mainly composed of local materials, but it also contains the atoms diffused from the other side of the interface and some other microstructures such as microprotrusions, dislocations, and oxidation from the other side of the interface. These microstructures cause the hot carriers scattering, the lattice defect scattering, dislocation scattering, and others scattering. The hot carriers scattering at the interface caused the interfacial thermal resistance. The interfacial thermal resistance, R_c, can be calculated by the following formulas:

$$R_c = \sum R_{CI} + R_{Sub} \quad \text{...... (1.2.1.2-1)}$$

$$R = \frac{\Delta T}{q} \quad \text{...... (1.2.1.2-2)}$$

$$q_{CI} = \frac{K_B^4}{8\pi^2\hbar^3}\left(\sum\nolimits_{CI} V_{1,j}^{-2}\right)\alpha_{1\to2}\left(T_1^4\int_{z=0}^{-\hbar\omega/K_BT_1}\frac{z^3d_z}{\exp(z)-1} - T_2^4\int_{z=0}^{-\hbar\omega/K_BT_2}\frac{z^3d_z}{\exp(z)-1}\right)$$

…… (1.2.1.2-3)

$$q_{Sub} = \frac{-1}{3d}\,CVl\Delta T$$

…… (1.2.1.2-4)

where subscripts *CI* and *Sub* are the contact interface layer and subsurface layer, respectively; *R* is thermal resistance; $\triangle T$ and *q* are the temperature difference of the interface layer and the heat flux density through the interface, respectively; K_B is Boltzmann constant; *V* is mean sounding velocity; *α* is the transmittance of phonon; *T* is temperature; *ħ* is Planck's constant; *ω* is angular frequency; *z* is the acoustic resistance of solid materials; *d* is the thickness of the subsurface layer; *C* is volume-specific heat; *l* is the mean free path of phonon scattering process; *j* is the phonon mode for 1 and 2. However, the interface thickness *d* is closely related to the interface heat flux density, contact area, load pressure on the contact surface, and other factors. Therefore, the correlation between them cannot be obtained directly. Thus, it is not easy to obtain the interface thickness *d*.

AMM model assumes that the contact interface of two solid materials is a plane, and phonons are treated as continuous plane waves. The propagation of phonons on the interface is complete specular reflection and refraction, and the propagation is no possibility of diffuse scattering. The interfacial thermal resistance can be calculated as follows:

$$R_c = \left[\frac{\pi^2 K_B^4 \Gamma_{1\to2}}{15\hbar^3}\left(\sum_j V_{1,j}^{-2}\Gamma_{1,j}\right)\right]^{-1} T^{-3}$$

…… (1.2.1.2-5)

$$\Gamma_{1,j} = \int_0^{\pi/2} \alpha_{1\to2}(\theta,j)\sin\theta\cos\theta d_\theta$$

…… (1.2.1.2-6)

where *θ* is phonon incident angle. Under low-temperature conditions, phonon wavelength is much larger than interface roughness size and interface defect size, and the contact interface can be approximately regarded as a plane. The AMM model is reliable to calculate the interfacial thermal resistance under low-temperature conditions. However, under high-temperature conditions, the wavelength of phonons is reduced to close to the size of interface roughness, so the contact interface of two solids cannot be approximated as a plane, and the possibility of phonons scattering at the interface is very high. The interfacial thermal resistance calculated by the AMM model may have a more significant error.

DMM model assumes that phonons are completely elastically scattered at the contact interface of two solid materials, and the transmittance of phonons (α) is related to the phonon density of states of the material. Therefore, the calculation expressions of the interface thermal resistance are as follows:

$$R_c = \left(\frac{\pi^2 K_B^4 V_1^{-2} \alpha_{1\rightarrow 2}}{30\hbar^3}\right)^{-1} T_2^{-3}$$

…… (1.2.1.2 -7)

$$\alpha_{1\rightarrow 2} = \frac{\sum_j V_{2,j}^{-2}}{\sum_j V_{1,j}^{-2} + \sum_j V_{2,j}^{-2}}$$

…… (1.2.1.2-8)

Comparing with the AMM model, the DMM model can better predict the interfacial thermal resistance under high-temperature conditions. For example, Stevens [93] and Stoner[94] reported that the value of interfacial thermal resistances calculated with the DMM model under room temperature was one order of magnitude less than the experimental value of interfacial thermal resistances. AMM and DMM models both have a specific temperature range to calculate interfacial thermal resistance. The reasons are that AMM ignores the phonons scattering at the interface, while DMM assumes that phonons are completely scattered at the interface.

The heat transfer mechanism of hot carriers (phonons and electrons) at the contact interface is very complicated. Therefore, it is difficult to obtain ideal results if only the macro or micro model calculates the interface heat conduction. Fortunately, Lattice Boltzmann proposed a mesoscopic simulation at multi-scale levels. The model combines the discrete macroscopic simulation and the continuous microscopic method, and the calculation of interface thermal resistance considers the scattering and radiation of phonons and electrons. Han et al. [68, 70] calculated the interfacial thermal resistance using the thermal lattice Boltzmann method framework.

1.3.3 Theoretical calculation for the interfacial thermal resistance at GFs-Al interface

For GFs/Al composites, the interfacial thermal resistance is considered to have a considerable effect on the ETC, and the effect cannot be eliminated. The interfacial thermal resistance at the GFs-Al interface is commonly calculated using AMM and DMM models. Interfacial thermal resistance is equal to the reciprocal of interfacial thermal conductance (*h*). Chen et al. [32] obtained the experimental value of *h* to be 5.0×10^7 W m^{-2} K^{-1}, and the calculated value by the DMM model showed the same order of magnitude as 10^7. In addition, The values of *h* calculated by AMM were as 4.5×10^7 [11, 29] W m^{-2} K^{-1}, 4.8×10^7 [26] W m^{-2} K^{-1}, and 7.4×10^7 [13] W m^{-2} K^{-1}.

However, as mentioned in 1.3.1 and 1.3.2 parts, the AMM and DMM models are suitable for calculating interfacial thermal resistance in different temperature ranges. Moreover, the calculation results are not completely reliable because the calculations are based on an ideal contact interface. Therefore, it is crucial to understand how heat conducts at the interfacial surface to obtain the accurate value of interfacial thermal resistance. Researchers considered that the hot carriers of metal heat transfer are mainly electrons at the micro-level, and the hot carriers of nonmetal heat transfer are mainly phonons. Hence, the heat transfer across the metal-nonmetal interface has two possible pathways. One is the coupling between electrons of metal and phonons of nonmetal through a harmonic interaction at the contact interfaces. Another is the coupling between electrons and phonons in the metal matrix and then the couplings of the metal electrons and the nonmetal phonons [95]. As Battabyal et al.[96] reported that the heat conduction mechanisms at the diamond-Al interface were the coupling between Al electrons and Al phonons and the coupling between diamond and Al phonons that occurred at the interface. Similarly, the heat conduction mechanism at the diamond-Al should be suitable for the heat conduction at the GFs-Al interface.

1.4 Theoretical and simulation calculations for the ETC of composites

1.4.1 Theoretical calculation for the ETC of composites

The influential factors of the ETC of composite include the size, shape, volume fraction, dispersion and orientation of the filling phase, porosity, and interfacial thermal resistance. In past studies, many models were proposed to calculate the effects of those factors on the ETC of composites. The models[18, 48, 49, 57, 97-105] can be divided into theoretical and empirical models. Table 1-4 shows some summarized theoretical models.

Maxwell's model is the original theoretical model used to predict the ETC of composites [106, 107]. Maxwell's model assumes that the shape of the filled phase is spherical, the volume fraction of the filled phase is small, and the filled phases are uniform dispersion and independent of each other. However, Maxwell's model is a very simple theoretical model, and its application has significant limitations. For example, the ETC value calculated by Maxwell's model would significantly differ from the experimental ETC value if the filled phase has a high-volume fraction, or the shape of the filled phase was ellipsoid, fiber, and sheet, or considering the effects of interfacial thermal resistance and porosity. Therefore, many new theoretical models extended based on Maxwell's model were proposed, such as Bruggeman's model [58, 108], Fricke's model [109], Hamilton-Crosser's model [110], Every's model [58], Nan's model[111], etc.

For example, Bruggeman's model was developed by integrating the differential equation of Maxwell's model, and it is suitable for the ETC calculations of composites with a high-volume fraction of the filled phase. Fricke's model is suitable for the ETC calculations of composites with filled elliptical phases and a high volume fraction of filled phase. Hamilton-Crosser's model is suitable for calculating the effect of the filled phase shape on the ETC. Furthermore, Every's model was extended based on Bruggeman's model, and it further considers the effect of the interfacial thermal resistance on ETC. Nan's model can consider the effects of size, shape, orientation, dispersion, the volume fraction of filled phase, and interfacial thermal resistance on ETC.

Besides, many scholars also developed other theoretical models, such as the Cheng-Vachon model [112, 113], Nielsen model [114, 115], etc. Meanwhile, the empirical models have the Springer-Tsai model [116], Y. Agari's models[107, 117, 118], etc.

Table 1-4 Theoretical models using to calculate the ETC of composites.

Models	Equation
Maxwell	$\lambda_c = \lambda_m \frac{2\lambda_m+\lambda_p-2V_p(\lambda_m-\lambda_p)}{2\lambda_m+\lambda_p+V_p(\lambda_m-\lambda_p)}$;
Bruggeman	$(1-V_p)^3 = \frac{\lambda_m}{\lambda_c}\left(\frac{\lambda_c-\lambda_p}{\lambda_m-\lambda_p}\right)^3$;
Fricke	$\lambda_c = \lambda_m \left\{\frac{1+V_p[S(\lambda_p/\lambda_m-1)]}{1+V_p(S-1)}\right\}$; $S = \frac{1}{3}\sum_{i=1}^{3}\left[1+(\lambda_p/\lambda_m-1)f_i\right]^{-1}$; $\sum_{i=1}^{3} f_i = 1$; f_i is the half-axis length of elliptical particles.
Hamilton-Crosser	$\lambda_c = \lambda_m \left[\frac{\lambda_p+(n-1)\lambda_m+(n-1)V_p(\lambda_p-\lambda_m)}{\lambda_p+(n-1)\lambda_m-V_p(\lambda_p-\lambda_m)}\right]$; n = 3/ψ; ψ is Particle sphericity.
Every	$(1-V_P)^3 = \left(\frac{\lambda_m}{\lambda_c}\right)^{(1+2a)/(1-a)} \left[\frac{\lambda_c-\lambda_p(1-a)}{\lambda_m-\lambda_p(1-a)}\right]^{3/(1-a)}$; a is the radius of the reinforcement particles.
Cheng-Vachon	$\frac{1}{\lambda_c} = \frac{1-B}{\lambda_m} +$ $\frac{1}{\{C(\lambda_p-\lambda_m)[\lambda_m+B(\lambda_p-\lambda_m)]\}^{1/2}} \ln \frac{[\lambda_m+B(\lambda_p-\lambda_m)]^{1/2}+B/2[C(\lambda_p-\lambda_m)]^{1/2}}{[\lambda_m+B(\lambda_p-\lambda_m)]^{1/2}-B/2[C(\lambda_p-\lambda_m)]^{1/2}}$; $B = \left(\frac{3V_p}{2}\right)^{1/2}$, $C = B^{-1}$;
Nielsen	$\lambda_c = \lambda_m \frac{1+(K_E-1)\left[\left(\frac{\lambda_p}{\lambda_m}-1\right)/\left(\frac{\lambda_p}{\lambda_m}+K_E-1\right)\right]V_p}{1-\left[\left(\frac{\lambda_p}{\lambda_m}-1\right)/\left(\frac{\lambda_p}{\lambda_m}+K_E-1\right)\right]\left[1+\frac{(1-V_m)}{V_m^2}V_P\right]V_p}$; K_E is the Einstein coefficient.

where λ and V represent the TC and volume fraction; Subscript c represents composite, and m and p represent the matrix and filled phase of composites, respectively.

1.4.2 Theoretical calculation for the ETC of GFs/Al composites

As above summarized, many theoretical models have been developed to predict the ETC of composites. However, according to the structural characteristics of GFs/Al composites, the mixing rule and Nan's model are the favorite of researchers [14, 18, 26, 28, 29].

The mixing rules can be expressed:

$$\lambda_c^{x-y} = V_{GFs} \times \lambda_{GFs}^{x-y} + (1 - V_{GFs}) \times \lambda_{\mathrm{Al}} \qquad \text{…… (1.3.2-1)}$$

$$\frac{1}{\lambda_c^z} = \frac{V_{GFs}}{\lambda_{GFs}^z} + \frac{1 - V_{GFs}}{\lambda_{\mathrm{Al}}} \qquad \text{…… (1.3.2-2)}$$

where λ_c is the ETC of GFs/Al composites, λ_{GFs}^{x-y} is the TC of GFs along the basal-plane, λ_{GFs}^z is the TC of GFs along the out-plane, λ_{Al} is the TC of Al matrix, and the V_{GFs} is the volume fraction of GFs. Equation 1.3.2-1 uses to calculate the ETC of GFs/Al composites when the basal-pane of GFs is parallel to the heat flow direction; Equation 1.3.2-2 uses to calculate the ETC of GFs/Al composites when the out-pane of GFs is parallel to the heat flow direction. However, it is worth noting that the mixing rule is a simple theoretical model to calculate the ETC of composites, and the mixing rules only consider the effect of volume fraction of the filled phase on the ETC. Therefore, the ETC of GFs/Al composites calculated using the mixing rules would be higher than the ETC obtained by experiment methods, mainly attributed to the effects of the orientation and the dispersion of GFs and interfacial thermal resistance.

To consider the effect of interfacial thermal resistance, TC of GFs, $\lambda_{GFs\text{-}eff}$, can be calculated by the following equation1.3.2-3, as follows:

$$\lambda_{GFs-eff}^i = \frac{\lambda_{GFs}^i}{1 + \frac{2\lambda_{GFs}^i}{hD}} \qquad \text{…… (1.3.2-3)}$$

where *i* is the *x-y* plane or *z-axis* direction, *h* is the interfacial thermal conductance, and

D is the thickness and diameter of GFs. *h* is the reciprocal of interfacial thermal resistance (*R*), *h* = 1/ *R*. To calculate ETC of composites considering the interfacial thermal resistance, the equations can be obtained using $\lambda_{GFs\text{-}eff}$ to replace the λ_{GFs}^{x-y} and the λ_{GFs}^{z} in the mixing rules.

Nan's model[111] is an effective medium approximate model (EMA) to predict the ETC of GFs/Al composites. It includes the effects of the size, shape, and orientation [28, 29]. The equations can be expressed as:

$$\lambda_c^{x-y} = \lambda_{Al}\frac{2 + V_{GFs}\left[\lambda_{GFs}^{x-y}(1 - S_{11})(1 + \langle cos^2\theta\rangle) + \lambda_{GFs}^{z}(1 - S_{33})(1 - \langle cos^2\theta\rangle)\right]}{2 - V_{GFs}\left[\lambda_{GFs}^{x-y}S_{11}(1 + \langle cos^2\theta\rangle) + \lambda_{GFs}^{z}S_{33}(1 - \langle cos^2\theta\rangle)\right]}$$

…… (1.3.2-4)

$$\lambda_c^{z} = \lambda_{Al}\frac{1 + V_{GFs}\left[\lambda_{GFs}^{x-y}(1 - S_{11})(1 - \langle cos^2\theta\rangle) + \lambda_{GFs}^{z}(1 - S_{33})\langle cos^2\theta\rangle\right]}{1 - V_{GFs}\left[\lambda_{GFs}^{x-y}S_{11}(1 - \langle cos^2\theta\rangle) + \lambda_{GFs}^{z}S_{33}\langle cos^2\theta\rangle\right]}$$

…… (1.3.2-5)

$$\langle cos^2\theta\rangle = \frac{\int \rho(\theta)cos^2\theta\sin\theta\, d\theta}{\int \rho(\theta)\sin\theta\, d\theta}$$

…… (1.3.2-6)

where θ is the angle between heat flow direction and the basal plane of GFs; S_{ij} is the geometrical factors (such as size and shape) of GFs. To consider the effects of the geometrical factors S_{ij} of GFs on the ETC of GFs/Al composites, the thermal conductivities of GFs along the basal-plane (λ_{GFs}^{x-y}) and the out-plane (λ_{GFs}^{z}) are replaced by λ_{GFs-e}^{x-y} and λ_{GFs-e}^{z} .

$$\lambda_{GF}^{x-y} = \frac{\lambda_{GFs}^{x-y} - \lambda_{Al}}{\lambda_{Al} + S_{11}\left(\lambda_{GFs}^{x-y} - \lambda_{Al}\right)}$$

…… (1.3.2-7)

$$\lambda_{GFs-eff}^{z} = \frac{\lambda_{GFs}^{z} - \lambda_{Al}}{\lambda_{Al} + S_{33}(\lambda_{GFs}^{z} - \lambda_{Al})}$$

……. (1.3.2-8)

Assuming that GFs is an ellipsoidal shape, the semi-axes *a* and *b* of GFs on the two-dimensional plane are the same (*a* = *b*), and the thickness of GFs is *c*. According to the ratio (*p*) between *c* and semi-axes *a* or *b*, S_{ii} can be obtained using the following equations[119]:

$$S_{11} = S_{22} = \begin{cases} \frac{p^2}{2(p^2-1)} - \frac{p}{2(p^2-1)^{2/3}} cosh^{-1}p, & p > 1 \\ \frac{p^2}{2(p^2-1)} + \frac{p}{2(p^2-1)^{2/3}} cos^{-1}p, & p < 1 \end{cases}$$

…… (1.3.2-9)

If GFs are highly oriented in the Al matrix, the $<cos^2\theta>$ is infinitely close to 1. Moreover, to regard the shape of GFs as a disk, S_{ij} were calculated[119] as, $S_{11} = S_{22} = \pi p/4$ and $S_{33} = 1 - \pi p/2$.

1.4.3 Simulation calculation for the ETC of composites

With the rapid development of computer technology, simulation methods have become a new and effective research tool to calculate the ETC of composites. Many simulation methods have been developed to predict the ETC of composites, such as molecular dynamics (MD), lattice Boltzmann method (LBM), finite volume method (FVM), finite element method (FEM), etc. Those methods analyze the ETC of composites at different simulation scales from micro-scale, mesoscale, to macro-scale.

1.4.3.1 Microscale model

The microscopic simulation is an atomic level calculation, and it is used to analyzes the interaction between atoms through first principles. The calculation method's essence is to use the Monte Carlo method (MC) or MD to solve the approximate solution of the Schrödinger equation. MD is the most used model to solve the Schrödinger equation. MD includes equilibrium and non-equilibrium molecular dynamics (EMD and NEMD).

EMD calculates the ETC of composites under the steady temperature field, and its theoretical function to calculate the ETC(λ_c) is based on the Green-Kubo equation, as follow:

$$\lambda_c = \frac{1}{3VK_BT^2}\int_0^\infty \langle J(t)J(0)\rangle dt$$

…… (1.3.3.1)

where V is the volume of the system, K_B is Boltzmann constant, T is temperature, J is microscopic heat flow, and t is time. However, using EMD to calculate ETC would generate amounts of calculation and spend lots of time because of the very slow convergence calculation of J and its related functions. As a comparison with EMD, NEMD shows a better convergence calculation. NEMD establishes a non-equilibrium heat conduction process by applying disturbances to the system, and then to calculate ETC of composites using the Fourier function of heat conduction, $J = - \lambda \triangle T$. NEMD method is generally used to calculate the ETC of composites[120-124]. Tian et al[120]. studied the effects of the filled phase's orientation, dispersion, and arrangement, the interface mismatch, the interface density, and the filled phase polydispersity on the ETC of nanocomposites. Yang et al. [124] employed the NEMD method to calculate the TC of defective graphene oxide. However, NEMD also has the disadvantages, such as poor model homogeneity, momentum, energy conservation, etc. Müller-plathe et al[125]. proposed a reverse perturbation non-equilibrium molecular dynamic method (RNEMD) for calculating the thermal conductivity. RNEMD can correct the disadvantages in the momentum and energy conservation of NEMD mothed, making it more suitable for calculating ETCs.

1.4.3.2 Mesoscale model

Compared with the microscopic simulation, mesoscopic simulation models contain huge numbers of atoms (about 10^{23} /cm^3), and they are much larger than the microscopic simulation models. The theoretical equation is different from the

Schrödinger equation, and it belongs to the average basic characteristic structure relationship. Due to the complex diversity of mesoscopic scale mechanisms and constitutive laws, different mesoscopic simulation models were developed[126]: 1, Space and time discretization dislocation dynamics model; 2, Phase-field dynamics or generalized Ginzburg-Landau model; 3, Deterministic or probabilistic meta-packet automata model; 4, Polymorphic Dynamics Potts Model; 5, Geometry topology and grouping model; 6, Topological mesh and vertex model. Although the mesoscopic simulation models are diverse, they have some common characteristics. E.g., the mesoscopic model does not contain obvious atomic-scale dynamics but an idealized assumption that the material is a continuum. So, the lattice defects have a common uniform matrix, and the matrix naturally couples the interactions between lattice defects. Thus, intrinsic space and time scales are not explicitly included in the corresponding governing equations. Moreover, a continuum mesoscopic scale model containing a single lattice defect usually has a series of phenomenological partial differential rates and intrinsic structural equations. Those differential equations are usually solved by the finite difference method, finite element, or Monte Carlo method.

In the mesoscopic scale model, the determinations of space-time scale parameters and dispersion are determined by the differential equation and its coefficients and the characteristics and properties of the variables. The control of differential equations is used for local or global situations according to the interaction between lattice defects. State variables (atomic concentration, dislocation density, structural parameters, displacement, lattice orientation) are usually combined with spatial grid coordinates. Because the phenomenological equation and the law of structural evolution have been well studied on the mesoscopic scale, it is of great significance to use the continuum approximation method to predict the structural evolution on the mesoscopic scale. Additionally, the experimental data obtained from the mesoscale model is easier than the data obtained from the micro-scale, and it is more detailed than the information obtained from the macro-scale model. The methods to solve the mesoscopic scale model mainly include DM, MC, and finite element method (FEM).

Mesoscopic scale models used to calculate the ETC of composites have been developed, and the most commonly used calculation methods include dissipative particle dynamics (DPD), LBM, off-lattice MC, etc. Such as DPD was proposed by Hoogerbrugge and Koelman in the 1992 year, and it was used to solve the difference between the lattice automata method and the reality and the fluid problem on the mesoscopic time and space scale that MD cannot solve. DPD is a coarse-grained technology based on MD, which means that each particle represents one or more molecules or a fluid region of a fragment of a polymer rather than a single atom. Moreover, the particle interaction is expressed by a pair of conservative, dissipation, and random forces. R. Qiao et al. [127] calculated the TC of nanocomposites by energy-conserving DPD, and the obtained results were well agreed with the results calculated by the Maxwell-Garnett model. Bing Zhou et al.[128] studied the effect of volume fraction, alignment, dispersion and size of CNT, and polymer size on the ETC of CNT/polymer composites with random and aligned CNT by using coupling smoothed particle hydrodynamics and DPD methods.

1.4.3.3 Macroscale and multiscale model

The macroscopic simulation model treats the composite material as a single orthotropic material or completely anisotropic material. The macroscopic models of composites are commonly used to simulate the overall performances of the composites. Thus, the Non-linearity of materials and local failures are not considered. Furthermore, compared with microscopic and mesoscopic scale models, macroscopic models do not contain the calculations at the atomic and molecular level, which can save lots of calculations and calculation time. Using macroscopic models to calculate the ETC of composites, FEM[105, 129-133], FVM[49], and FDM[134] are the most used methods.

Multi-scale simulation is a combination of microsimulation and macro simulation. Macroscopic simulation has the advantage of being a small amount of calculation and saving time, but it is difficult to reflect the effect of the microscopic behavior of each material on the overall properties of the composite. On the other hand, although the microscopic simulation can well understand the influence of the micro-behavior of each material on the overall behavior of the composite material, it has a considerable amount of calculation. As a result, because of the limitation of computer computing power and the structural complexity of composites, it is only possible to establish a micro-model based on the local characteristics of the composite. In contrast, the multi-scale model can well coordinate the collaborative calculation of the micro model and the macro model to study better the influence of the micro behavior of the material on the overall behavior and the overall properties of the material. Based on those advantages, multi-scale simulation has been widely used in the ETC calculation of composites[135-140].

1.5 Objective of this thesis

GFs are low-cost, lightweight, and possess excellent thermal properties, including high thermal conductivity and low thermal expansion coefficient. GFs/Al composites are thus chosen as the candidates of thermal management materials. Many experimental and theoretical studies have been conducted to investigate the ETC of GFs/Al composites. However, previous experimental studies found that the orientation of GFs, the interface reaction, and the interfacial thermal resistance greatly affect the composites' thermal properties.

Theoretical calculations and three-dimensional(3D) simulations are used to evaluate the ETC of GFs/Al composites considering the orientation of GFs and the interfacial thermal resistance. However, both theoretical calculations and 3D simulations exhibit the disadvantages of calculating the ETC of GFs/Al composites. For theoretical calculations, it is difficult for those theoretical models to calculate the ETC of GFs/Al composites due to the diversity of GFs' orientations in composites. Additionally, the 3D simulation calculations would take lots of time and be very expensive because these 3D models are constructed using images from ultra-high-resolution X-ray computed tomography. On the other hand, although two-dimensional (2D) images simulations are low-cost and high timeliness, few studies have used 2D images simulations to calculate the ETC of GFs/Al composites. The reason can be attributed to the orientation of GFs in 2D images may not be equivalent to the orientation of GFs in the corresponding experimental samples, which can result in the ETC of GFs/Al composites calculated by 2D images simulations are not reliable.

This study aims to study the effects of the orientation of GFs and the interfacial thermal resistance on the ETC of GFs/Al composites using 2D images simulations. The following steps did the works: In the first step, GFs/Al composites were fabricated using SPS. We measured the relative density of GFs/Al composites, analyzed the distribution and orientation of GF, investigated the formation of Al_4C_3, and evaluated the ETC and thermal expansion using the experimental and theoretical methods.

Secondly, we studied the relationship between the TCs of the GFs in 3D and 2D images. As a result, we obtained a fitted function used to convert TC of GFs from 2D to 3D. ETC of 10%vol GFs/Al composite was calculated using 2D image simulations, employing the fitted function. Thirdly, the effect degrees of the orientation of GFs and the interfacial thermal resistance on the ETC of GFs/Al composites were calculated by 2D image simulations.

1.6 Outline of this thesis

Chapter 1 Background and Objective

This chapter discusses the development of electronic packaging materials, the fabrication methods of the GFs/Al composites, some experimental studies of the thermal properties of GFs/Al composites, some theoretical and simulation methods for calculating the ETC of GFs/Al composites, and the objectives of this thesis.

Chapter 2 Experiment process and Fundamental properties of GFs/Al composites

In this chapter, the process of preparing GFs/Al composites using SPS was showed. The orientation, distribution, and aspect ratio of GFs in the Al matrix were analyzed by OM images. The relative density of composite was determined by the Archimedes method. The interface reaction was checked by XRD method. The thermal expansion coefficient and the ETC of GFs/Al composite were obtained by theoretical and experimental methods.

Chapter 3 Investigation the relationships between the effective thermal conductivity of GFs in the three-dimensional and two-dimensional model

In this chapter, we constructed 3D and 2D models of GFs/Al composites. The orientations and TCs of GFs in the 3D and 2D models were compared. Furthermore, the relationships between the orientations of GFs in 3D and 2D models were analyzed. As a result, a fitted equation was derived and used to convert the TC of GFs from 2D to 3D. Moreover, the effective thermal conductivity of the graphite flake/aluminum composite with 10 vol% graphite flakes was calculated using 2D image simulation and the fitted equation.

Chapter 4 Effect of the orientation of GFs and interfacial thermal resistance on the effective thermal conductivity of GFs/Al composites

In this chapter, the ETC of GFs/Al composites were calculated by using 2D image simulations, including the effect of GFs' orientation and interfacial thermal resistance. The effect degree of the orientation of GFs and the interfacial thermal resistance on the ETC of GFs/Al composites were analyzed. The interfacial thermal resistances at the GFs-Al interface were calculated.

Chapter 5 Conclusions

The results from the studies mentioned above were summarized in this chapter.

1.7 References

[1] Zweben C. Advances in composite materials for thermal management in electronic packaging. Jom. 1998;50(6):47-51.

[2] Kidalov S, Shakhov F. Thermal Conductivity of Diamond Composites. Materials. 2009;2(4):2467-95.

[3] Jin S. Advances in thermal management materials for electronic applications. JOM. 1998;50(6):46.

[4] Barcena J, Maudes J, Vellvehi M, Jorda X, Obieta I, Guraya C, et al. Innovative packaging solution for power and thermal management of wide-bandgap semiconductor devices in space applications. Acta Astronautica. 2008;62(6-7):422-30.

[5] Lee M. Fabrication and Properties Evaluation of CF/Al Composites for High Thermal Conductivity. Doctor Thesis, Hiroshima University. 2012.

[6] Xiaoliang Z, Rong S, Shuhui Y, Jianbin X, Chingping W. The Research Development and Trend of Substrates in Electronic Packages. internation technology. 2014;3:77-83.

[7] Zhiqiang L, Zhanqiu T, Genlian F, Di Z. Progress of Metal Matrix Composites for Efficient Thermal Management Applications. Mater China. 2013;32:431-40.

[8] Di Z, Tan Z, Xiong D, Li Z. Application and prospect of metal matrix composites for thermal management: an overview. Materials China. 2019;37(12):994-1001.

[9] Norley J. technical brief: the role of natural graphite in electronics cooling. Electronics Cooling. 2001;7:50-1.

[10] Prieto R, Molina JM, Narciso J, Louis E. Fabrication and properties of graphite flakes/metal composites for thermal management applications. Scripta Materialia. 2008;59(1):11-4.

[11] Zhou C, Ji G, Chen Z, Wang M, Addad A, Schryvers D, et al. Fabrication, interface characterization and modeling of oriented graphite flakes/Si/Al composites for thermal management applications. Materials & Design. 2014;63:719-28.

[12] Zhou S, Chiang S, Xu J, Du H, Li B, Xu C, et al. Modeling the in-plane thermal

conductivity of a graphite/polymer composite sheet with a very high content of natural flake graphite. Carbon. 2012;50(14):5052-61.

[13] Prieto R, Molina JM, Narciso J, Louis E. Thermal conductivity of graphite flakes–SiC particles/metal composites. Composites Part A: Applied Science and Manufacturing. 2011;42(12):1970-7.

[14] Chen JK, Huang IS. Thermal properties of aluminum–graphite composites by powder metallurgy. Composites Part B: Engineering. 2013;44(1):698-703.

[15] Hutsch T, Schubert T, Weissgaerber T, Kieback B. Graphite metal composites with tailored physical properties. Emerging Materials Research. 2012;1(2):107-14.

[16] Yoshida K, Morigami H. Thermal properties of diamond/copper composite material. Microelectronics Reliability. 2004;44(2):303-8.

[17] Li W, Liu Y, Wu G. Preparation of graphite flakes/Al with preferred orientation and high thermal conductivity by squeeze casting. Carbon. 2015;95:545-51.

[18] Xue C, Bai H, Tao PF, Jiang N, Wang SL. Analysis on Thermal Conductivity of Graphite/Al Composite by Experimental and Modeling Study. Journal of Materials Engineering and Performance. 2016;26(1):327-34.

[19] Lambert M, Fletcher L. Thermal conductivity of graphite/aluminum and graphite/copper composites. 1996.

[20] Etter T, Schulz P, Weber M, Metz J, Wimmler M, Löffler JF, et al. Aluminium carbide formation in interpenetrating graphite/aluminium composites. Materials Science and Engineering: A. 2007;448(1-2):1-6.

[21] Huang Y, Ouyang Q, Zhang D, Zhu J, Li R, Yu H. Carbon Materials Reinforced Aluminum Composites: A Review. Acta Metallurgica Sinica (English Letters). 2014;27(5):775-86.

[22] Liu T, He X, Zhang L, Liu Q, Qu X. Fabrication and thermal conductivity of short graphite fiber/Al composites by vacuum pressure infiltration. Journal of Composite Materials. 2013;48(18):2207-14.

[23] Huang Y, Ouyang Q, Guo Q, Guo X, Zhang G, Zhang D. Graphite film/aluminum laminate composites with ultrahigh thermal conductivity for thermal management applications. Materials & Design. 2016;90:508-15.

[24] Yolshina LA, Muradymov RV, Korsun IV, Yakovlev GA, Smirnov SV. Novel aluminum-graphene and aluminum-graphite metallic composite materials: Synthesis and properties. Journal of Alloys and Compounds. 2016;663:449-59.

[25] Amateau MF. Progress in the Development of Graphite- Aluminum Composites Using Liquid Infiltration Technology. Journal of Composite Materials. 2016;10(4):279-96.

[26] Xue C, Bai H, Tao PF, Wang JW, Jiang N, Wang SL. Thermal conductivity and mechanical properties of flake graphite/Al composite with a SiC nano-layer on graphite surface. Materials & Design. 2016;108:250-8.

[27] Kurita H, Miyazaki T, Kawasaki A, Lu Y, Silvain J-F. Interfacial microstructure of graphite flake reinforced aluminum matrix composites fabricated via hot pressing. Composites Part A: Applied Science and Manufacturing. 2015;73:125-31.

[28] Zhou C, Chen D, Zhang XB, Chen Z, Zhong SY, Wu Y, et al. The roles of geometry and topology structures of graphite fillers on thermal conductivity of the graphite/aluminum composites. Physics Letters A. 2015;379(5):452-7.

[29] Zhou C, Huang W, Chen Z, Ji G, Wang ML, Chen D, et al. In-plane thermal enhancement behaviors of Al matrix composites with oriented graphite flake alignment. Composites Part B: Engineering. 2015;70:256-62.

[30] Seong HG, Lopez HF, Robertson DP, Rohatgi PK. Interface structure in carbon and graphite fiber reinforced 2014 aluminum alloy processed with active fiber cooling. Materials Science and Engineering: A. 2008;487(1-2):201-9.

[31] Chang J, Zhang Q, Lin Y, Wu G. Layer by layer graphite film reinforced aluminum composites with an enhanced performance of thermal conduction in the thermal management applications. Journal of Alloys and Compounds. 2018;742:601-9.

[32] Schmidt AJ, Collins KC, Minnich AJ, Chen G. Thermal conductance and phonon transmissivity of metal–graphite interfaces. Journal of Applied Physics. 2010;107(10):104907.

[33] Swartz ET, Pohl RO. Thermal boundary resistance. Reviews of Modern Physics. 1989;61(3):605-68.

[34] Little W. The transport of heat between dissimilar solids at low temperatures. Canadian Journal of Physics. 1959;37(3):334-49.

[35] Rubinkovskii NA, Shornikov DP, Tenishev AV, Zaluzhnyi AG, Zholnin AG. Production of Aluminum-Graphite Composite by Spark Plasma Sintering. Glass and Ceramics. 2019;76(1-2):27-32.

[36] Durowoju MO, Asafa TB, Sadiku ER, Diouf S, Shongwe MB, Olubambi PA, et al. Improving mechanical and thermal properties of graphite–aluminium composite using Si, SiC and eggshell particles. Journal of Composite Materials. 2019;54(17):2365-76.

[37] Durowoju MO, Sadiku ER, Diouf S, Shongwe MB, Olubambi PA. Spark plasma sintering of graphite–aluminum powder reinforced with SiC/Si particles. Powder Technology. 2015;284:504-13.

[38] Salvo L, L'esperance G, Suery M, Legoux J. Interfacial reactions and age hardening in Al Mg Si metal matrix composites reinforced with SiC particles. Materials Science and Engineering: A. 1994;177(1-2):173-83.

[39] Candan E, Atkinson HV, Turen Y, Salaoru I, Candan S. Wettability of Aluminum-Magnesium Alloys on Silicon Carbide Substrates. Journal of the American Ceramic Society. 2011;94(3):867-74.

[40] Tjong SC. Recent progress in the development and properties of novel metal matrix nanocomposites reinforced with carbon nanotubes and graphene nanosheets. Materials Science and Engineering: R: Reports. 2013;74(10):281-350.

[41] Tan Z, Li Z, Fan G, Kai X, Ji G, Zhang L, et al. Diamond/aluminum composites processed by vacuum hot pressing: Microstructure characteristics and thermal properties. Diamond and Related Materials. 2013;31:1-5.

[42] Okura A, Motoki K. Rate of formation of intermetallic compounds in aluminium matrix-carbon fibre composites. Composites Science and Technology. 1985;24(4):243-52.

[43] J. Narciso RP, J.M. Molina, E. Louis, inventor Producción de materiales compuestos con alta conductividad térmica. Española patent ES2304314. 2007.

[44] J. Narciso RP, J.M. Molina, E. Louis, inventor Three Phase Composite Material With High Thermal Conductivity and Its Production patent EP2130932-B1. 2007.

[45] J. Narciso RP, J.M. Molina, E. Louis, inventor Production of Composite Materials With High Thermal Conductivity. 2008.

[46] Molina J. SiC as base of composite materials for thermal management. Silicon Carbide-Materials, Processing and Applications in Electronic Devices: IntechOpen 2011, p. 115-40.

[47] Molina J, Prieto R, Narciso J, Louis E. The effect of porosity on the thermal conductivity of Al–12 wt.% Si/SiC composites. Scripta Materialia. 2009;60(7):582-5.

[48] Sugio K, Kono K, Choi YB, Sasaki G. Evaluation of Effective Thermal Conductivity of Metal Matrix Composites by Using Image-Based Calculation. Materials Science Forum: Trans Tech Publ; p. 1939-43.

[49] Sugio K, Choi Y-B, Sasaki G. Effect of the Interfacial Thermal Resistance on the Effective Thermal Conductivity of Aluminum Matrix Composites. Materials Transactions. 2016;57(5):582-9.

[50] Wang H, Xu Y, Shimono M, Tanaka Y, Yamazaki M. Computation of Interfacial Thermal Resistance by Phonon Diffuse Mismatch Model. Materials Transactions. 2007;48(9):2349-52.

[51] Beffort O, Khalid F, Weber L, Ruch P, Klotz U, Meier S, et al. Interface formation in infiltrated Al (Si)/diamond composites. Diamond and related materials. 2006;15(9):1250-60.

[52] Geiger A, Hasselman D, Donaldson K. Effect of reinforcement particle size on the thermal conductivity of a particulate silicon carbide-reinforced aluminium-matrix composite. Journal of Materials Science Letters. 1993;12(6):420-3.

[53] Hasselman D, Donaldson KY, Geiger AL. Effect of reinforcement particle size on the thermal conductivity of a particulate-silicon carbide-reinforced aluminum matrix composite. Journal of the American Ceramic Society. 1992;75(11):3137-40.

[54] Benveniste Y. Effective thermal conductivity of composites with a thermal contact resistance between the constituents: Nondilute case. Journal of Applied Physics. 1987;61(8):2840-3.

[55] Jiajun W, Xiao-Su Y. Effects of interfacial thermal barrier resistance and particle

shape and size on the thermal conductivity of AlN/PI composites. Composites Science and Technology. 2004;64(10-11):1623-8.

[56] Gan J, Zhou Z, Yu A. Effect of particle shape and size on effective thermal conductivity of packed beds. Powder Technology. 2017;311:157-66.

[57] Wang XJ, Zhang LZ, Pei LX. Thermal conductivity augmentation of composite polymer materials with artificially controlled filler shapes. Journal of Applied Polymer Science. 2014;131(8).

[58] Every AG, Tzou Y, Hasselman D, Raj R. The effect of particle size on the thermal conductivity of ZnS/diamond composites. Acta Metallurgica et Materialia. 1992;40(1):123-9.

[59] Davis LC, Artz BE. Thermal conductivity of metal-matrix composites. Journal of Applied Physics. 1995;77(10):4954-60.

[60] Kapitza PL. Heat Transfer and Superfluidity of Helium II. Physical Review. 1941;60(4):354-5.

[61] Yovanovich MM. Four decades of research on thermal contact, gap, and joint resistance in microelectronics. IEEE transactions on components and packaging technologies. 2005;28(2):182-206.

[62] Rostami A, Hassan A, Lim P. Parametric study of thermal constriction resistance. Heat and mass transfer. 2001;37(1):5-10.

[63] Hmina N, Scudeller Y. Thermal interface resistance and subsurface effusivity of submicron metallic films on dielectric substrates: an experimental method for simultaneous determination. International journal of heat and mass transfer. 1998;41(18):2781-98.

[64] Prasher R. Thermal boundary resistance and thermal conductivity of multiwalled carbon nanotubes. Physical Review B. 2008;77(7).

[65] Thomas T, Probert S. Thermal contact of solids. Chemical and Process Engineering. 1966;47(11):51-&.

[66] Prasher RS, Phelan PE. A Scattering-Mediated Acoustic Mismatch Model for the Prediction of Thermal Boundary Resistance. Journal of Heat Transfer. 2001;123(1):105-12.

[67] Chotikaprakhan S, Haj-Daoud A, Dietzel D, Meckenstock R, Neubauer E, Pelzl J, et al. Cu-C interface systems evaluated with the help of the thermal wave contrast. The European Physical Journal Special Topics. 2008;153(1):175-8.

[68] Han K, Feng YT, Owen DRJ. Modelling of thermal contact resistance within the framework of the thermal lattice Boltzmann method. International Journal of Thermal Sciences. 2008;47(10):1276-83.

[69] Stevens RJ, Norris PM, Zhigilei LV. Molecular dynamics study of thermal boundary resistance: evidence of strong inelastic scattering transport channels. ASME International Mechanical Engineering Congress and Exposition; p. 37-46.

[70] Sellan DP, Landry ES, Turney JE, McGaughey AJH, Amon CH. Size effects in molecular dynamics thermal conductivity predictions. Physical Review B. 2010;81(21).

[71] Abramson AR, Tien C-L, Majumdar A. Interface and Strain Effects on the Thermal Conductivity of Heterostructures: A Molecular Dynamics Study. Journal of Heat Transfer. 2002;124(5):963-70.

[72] Fieberg C, Kneer R. Determination of thermal contact resistance from transient temperature measurements. International Journal of Heat and Mass Transfer. 2008;51(5-6):1017-23.

[73] Standard A. Standard test method for thermal transmission properties of thermally conductive electrical insulation materials. ASTM International. 2006.

[74] Lanping XLZTZ, Yonggang LZH. USING DOUBLE HEAT FLUX METER METHOD TO MEASURE THE THERMAL CONTACT RESISTANCE OF SOLID MATERIAL AT LOW TEMPERATURE AND VACUUM [J]. GRYOGENICS. 1999(4):36.

[75] Shi L. Investigation of heat transport on the solid-solid contact interface at low temperature. Huazhong University of Science & Technology, Wuhan. 2006.

[76] Ohsone Y, Wu G, Dryden J, Zok F, Majumdar A. Optical measurement of thermal contact conductance between wafer-like thin solid samples. 1999.

[77] Pichardo J, Alvarado-Gil J. Open photoacoustic cell determination of the thermal interface resistance in two layer systems. Journal of Applied Physics. 2001;89(7):4070-

5.

[78] Balderas-Lopez JA, Mandelis A. Self-normalized photothermal techniques for thermal diffusivity measurements. Journal of Applied Physics. 2000;88(11):6815-20.

[79] Wang X, Hu H, Xu X. Photo-Acoustic Measurement of Thermal Conductivity of Thin Films and Bulk Materials. Journal of Heat Transfer. 2001;123(1):138-44.

[80] Andrew N. Smith JLH. Thermal Boundary Resistance Measurements Using a Transient Thermoreflectance Technique. Microscale Thermophysical Engineering. 2000;4(1):51-60.

[81] Milošević ND. Determination of Transient Thermal Interface Resistance Between Two Bonded Metal Bodies using the Laser-Flash Method. International Journal of Thermophysics. 2008;29(6):2072-87.

[82] Lahmar A, Nguyen T, Sakami D, Orain S, Scudeller Y, Danes F. Experimental investigation on the thermal contact resistance between gold coating and ceramic substrates. Thin Solid Films. 2001;389(1-2):167-72.

[83] Chen Z, Jang W, Bao W, Lau C, Dames C. Thermal contact resistance between graphene and silicon dioxide. Applied Physics Letters. 2009;95(16):161910.

[84] Yovanovich M. Thermal Spreading and Contact. Heat transfer handbook. 2003;1:261.

[85] Lambert M, Fletcher L. Thermal contact conductance of spherical rough metals. 1997.

[86] Bahrami M. Modeling of thermal joint resistance for sphere-flat contacts in a vacuum. 2004.

[87] Jackson RL, Bhavnani SH, Ferguson TP. A Multiscale Model of Thermal Contact Resistance Between Rough Surfaces. Journal of Heat Transfer. 2008;130(8).

[88] Jackson RL, Streator JL. A multi-scale model for contact between rough surfaces. Wear. 2006;261(11-12):1337-47.

[89] Zhong M, Cheng S-x, Sun C-w, He L-q. Monte-Carlo Simulation for Thermal Resistance of Contact Surfaces. Chinese Journal of High Pressure Physics. 2002;16(4):305-8.

[90] Zhang W, Xuan Y. the simulation of thermal contact resistance in microscale.

Chinese Engineering Thermophysics Conference. China.

[91] Huiling W, Eska G. An aluminum. heat switch made from cold-pressed Cu-Al composite. Physica B. 2000:284-8.

[92] Ling S, Xinming Y, Huiling W, Xuejun W. The investigation of solid-solid contact interface thermal transfer [J]. Cryogenics and Superconductivity. 2008;10.

[93] Stevens RJ, Smith AN, Norris PM. Measurement of Thermal Boundary Conductance of a Series of Metal-Dielectric Interfaces by the Transient Thermoreflectance Technique. Journal of Heat Transfer. 2005;127(3):315-22.

[94] Stoner RJ, Maris HJ. Kapitza conductance and heat flow between solids at temperatures from 50 to 300 K. Physical review B, Condensed matter. 1993;48(22):16373-87.

[95] Majumdar A, Reddy P. Role of electron–phonon coupling in thermal conductance of metal–nonmetal interfaces. Applied Physics Letters. 2004;84(23):4768-70.

[96] Battabyal M, Beffort O, Kleiner S, Vaucher S, Rohr L. Heat transport across the metal–diamond interface. Diamond and Related Materials. 2008;17(7-10):1438-42.

[97] Gori F, Corasaniti S. Effective thermal conductivity of composites. International Journal of Heat and Mass Transfer. 2014;77:653-61.

[98] Ngo I-L, Byon C. A generalized correlation for predicting the thermal conductivity of composite materials. International Journal of Heat and Mass Transfer. 2015;83:408-15.

[99] Nan CW, Shi Z, Lin Y. A simple model for thermal conductivity of carbon nanotube-based composites. Chemical Physics Letters. 2003;375(5-6):666-9.

[100] Song YS, Youn JR. Evaluation of effective thermal conductivity for carbon nanotube/polymer composites using control volume finite element method. Carbon. 2006;44(4):710-7.

[101] Zhai S, Zhang P, Xian Y, Zeng J, Shi B. Effective thermal conductivity of polymer composites: Theoretical models and simulation models. International Journal of Heat and Mass Transfer. 2018;117:358-74.

[102] Wejrzanowski T, Grybczuk M, Chmielewski M, Pietrzak K, Kurzydlowski KJ,

Strojny-Nedza A. Thermal conductivity of metal-graphene composites. Materials & Design. 2016;99:163-73.

[103] Zhang H, Li Y-M, Tao W-Q. Theoretical accuracy of anisotropic thermal conductivity determined by transient plane source method. International Journal of Heat and Mass Transfer. 2017;108:1634-44.

[104] Wang M, Kang Q, Pan N. Thermal conductivity enhancement of carbon fiber composites. Applied Thermal Engineering. 2009;29(2-3):418-21.

[105] Islam MR, Pramila A. Thermal conductivity of fiber reinforced composites by the FEM. Journal of Composite Materials. 1999;33(18):1699-715.

[106] Progelhof R, Throne J, Ruetsch R. Methods for predicting the thermal conductivity of composite systems: a review. Polymer Engineering & Science. 1976;16(9):615-25.

[107] Agari Y, Uno T. Estimation on thermal conductivities of filled polymers. Journal of Applied Polymer Science. 1986;32(7):5705-12.

[108] Ott H. Thermal conductivity of composite materials. 1981.

[109] Fricke H. The Maxwell-Wagner dispersion in a suspension of ellipsoids. The Journal of Physical Chemistry. 1953;57(9):934-7.

[110] Hamilton RL, Crosser O. Thermal conductivity of heterogeneous two-component systems. Industrial & Engineering chemistry fundamentals. 1962;1(3):187-91.

[111] Nan C-W, Birringer R, Clarke DR, Gleiter H. Effective thermal conductivity of particulate composites with interfacial thermal resistance. Journal of Applied Physics. 1997;81(10):6692-9.

[112] Tsao GT-N. Thermal conductivity of two-phase materials. Industrial & Engineering Chemistry. 1961;53(5):395-7.

[113] Cheng S, Law Y, Kwan C. Thermal conductivity of two-phase and three-phase heterogeneous solid mixtures. International Journal of Heat and Mass Transfer. 1972;15(2):355-8.

[114] Nielsen LE. Generalized equation for the elastic moduli of composite materials. Journal of Applied Physics. 1970;41(11):4626-7.

[115] Lewis TB, Nielsen LE. Dynamic mechanical properties of particulate-filled composites. Journal of applied polymer science. 1970;14(6):1449-71.

[116] Tavman I, Akinci H. Transverse thermal conductivity of fiber reinforced polymer composites. International Communications in Heat and Mass Transfer. 2000;27(2):253-61.

[117] Agari Y, Tanaka M, Nagai S, Uno T. Thermal conductivity of a polymer composite filled with mixtures of particles. Journal of Applied Polymer Science. 1987;34(4):1429-37.

[118] Agari Y, Ueda A, Nagai S. Thermal conductivity of a polymer composite. Journal of Applied Polymer Science. 1993;49(9):1625-34.

[119] Hiroshi H, Minoru T. Equivalent inclusion method for steady state heat conduction in composites. International Journal of Engineering Science. 1986;24(7):1159-72.

[120] Tian Z, Hu H, Sun Y. A molecular dynamics study of effective thermal conductivity in nanocomposites. International Journal of Heat and Mass Transfer. 2013;61:577-82.

[121] Wang T-Y, Tsai J-L. Investigating thermal conductivities of functionalized graphene and graphene/epoxy nanocomposites. Computational Materials Science. 2016;122:272-80.

[122] Ju S-P, Haung T-J, Liao C-H, Chang J-W. Investigation of thermal conductivity of graphite flake/poly (p-phenylene sulfide) composite by experimental measurement and non-equilibrium molecular dynamics simulation. Polymer. 2013;54(17):4702-9.

[123] He YAN, Tang Y. Thermal Conductivity Of Carbon Nanotube/Natural Rubber Composite From Molecular Dynamics Simulations. Journal of Theoretical and Computational Chemistry. 2013;12(03):1350011.

[124] Yang Y, Cao J, Wei N, Meng D, Wang L, Ren G, et al. Thermal Conductivity of Defective Graphene Oxide: A Molecular Dynamic Study. Molecules. 2019;24(6).

[125] Müller-Plathe F. A simple nonequilibrium molecular dynamics method for calculating the thermal conductivity. The Journal of chemical physics.

1997;106(14):6082-5.

[126] Bo DL. Computational Materials Science. Bei Jing: Beijing Chemical Industry Press; 2002.

[127] Qiao R, He P. Simulation of heat conduction in nanocomposite using energy-conserving dissipative particle dynamics. Molecular Simulation. 2007;33(8):677-83.

[128] Zhou B, Luo W, Yang J, Duan X, Wen Y, Zhou H, et al. Thermal conductivity of aligned CNT/polymer composites using mesoscopic simulation. Composites Part A: Applied Science and Manufacturing. 2016;90:410-6.

[129] Tsekmes IA, Kochetov R, Morshuis PHF, Smit JJ. Modeling the thermal conductivity of polymeric composites based on experimental observations. IEEE Transactions on Dielectrics and Electrical Insulation. 2014;21(2):412-23.

[130] Li X, Fan X, Zhu Y, Li J, Adams JM, Shen S, et al. Computational modeling and evaluation of the thermal behavior of randomly distributed single-walled carbon nanotube/polymer composites. Computational Materials Science. 2012;63:207-13.

[131] Tong Z, Liu M, Bao H. A numerical investigation on the heat conduction in high filler loading particulate composites. International Journal of Heat and Mass Transfer. 2016;100:355-61.

[132] Zhang Y-F, Zhao Y-H, Bai S-L, Yuan X. Numerical simulation of thermal conductivity of graphene filled polymer composites. Composites Part B: Engineering. 2016;106:324-31.

[133] Druma AM, Alam MK, Druma C. Analysis of thermal conduction in carbon foams. International journal of thermal sciences. 2004;43(7):689-95.

[134] Zhang L-Z, Wang X-J, Quan Y-Y, Pei L-X. Conjugate heat conduction in filled composite materials considering interactions between the filler and base materials. International Journal of Heat and Mass Transfer. 2013;64:735-42.

[135] Chinkanjanarot S. Multiscale Modeling: Thermal Conductivity of Graphene/Cycloaliphatic Epoxy Composites. 2017.

[136] Mortazavi B, Hassouna F, Laachachi A, Rajabpour A, Ahzi S, Chapron D, et al. Experimental and multiscale modeling of thermal conductivity and elastic properties of PLA/expanded graphite polymer nanocomposites. Thermochimica Acta.

2013;552:106-13.

[137] Montazeri A, Rafii-Tabar H. Multiscale modeling of graphene- and nanotube-based reinforced polymer nanocomposites. Physics Letters A. 2011;375(45):4034-40.

[138] Clancy TC, Frankland SJV, Hinkley JA, Gates TS. Multiscale modeling of thermal conductivity of polymer/carbon nanocomposites. International Journal of Thermal Sciences. 2010;49(9):1555-60.

[139] Chinkanjanarot S, Tomasi JM, King JA, Odegard GM. Thermal conductivity of graphene nanoplatelet/cycloaliphatic epoxy composites: Multiscale modeling. Carbon. 2018;140:653-63.

[140] Wang Y, Yang C, Mai Y-W, Zhang Y. Effect of non-covalent functionalisation on thermal and mechanical properties of graphene-polymer nanocomposites. Carbon. 2016;102:311-8.

Chapter 2

Fabrication and Thermal Properties of GFs/Al composites

2.1 Introduction

Carbon materials reinforced Al-matrix composites attract great interest from researchers of electron packaging materials due to their lightweight, superior mechanical, and thermal properties [1-7]. Especially for graphite flakes (GFs) reinforced Al-matrix composites, their excellent thermal properties, such as high thermal conductivity (TC) and low coefficient of thermal expansion [5, 8-10], are able to meet the thermal performance requirements of electron packaging materials.

Lots of experiments have been performed to study the effective thermal conductivity (ETC) of GFs/Al composites and found that the high thermal conductivity of GFs cannot be fully displayed due to the following characteristics: 1, the thermal conductivity of GFs is significant anisotropic, its orientation in the composites hinder the effective thermal conductivity of GFs/Al composites; 2, GFs tends to react with Al during the fabricating the GFs/Al composites, the formation of Al_4C_3 is bad for the mechanical properties and reduce the effective thermal conductivity of GFs/Al composites; 3, the interfacial thermal resistance is considered to have a great effect on the effective thermal conductivity of GFs/Al composites. Therefore, a suitable fabrication process of GFs/Al composites is essential to take advantage of the high thermal conductivity properties of GFs.

In previous studies on the effective thermal conductivity of GFs/Al composite, the commonly used fabrication methods of GFs/Al composite include the vacuum hot pressing[9-12], squeeze casting[13-15], and gas pressure infiltration[8, 16]. The interface reaction can be effectively avoided using those methods. For example, Chen et al. [12] fabricated the GFs/Al composites by hot pressure method, and a low sintering temperature, lower than the melting point of Al, was used to avoid the interface reaction. The ETC of GFs/Al composites with 80 vol. % GFs achieved up to 783 W m^{-1} K^{-1}. Xue et.al[10]. fabricated GFs/Al composites by vacuum hot pressing method, the surface of GFs were pre-processed with SiC particles coating to inhibit the interface reaction. The ETC of GFs/Al composites with 70 vol. % GFs was up to 735 W m^{-1} K^{-1}. Li et al.[13]

prepared GFs/Al composites by squeeze casting method, and rapid cooling method was used to hinder the interface reaction. The effective thermal conductivity of the sample with 70 vol. % GFs was as high as 714 W m^{-1} K^{-1}. Zhou et al.[8] used pressure infiltration to prepare GFs/Al composites. Si particles were introduced to suppress the interface reaction. The effective thermal conductivity of the sample with 71.1 vol. % GFs was 526 W m^{-1} K^{-1}. The interface reaction can be hinted at by low sintering temperature, rapid cooling, or adding Si or SiC particles. However, the effective thermal conductivities of GFs/Al composites were lower than the expected theoretical effective thermal conductivities. The main reasons can be attributed to the effects of the orientation of GFs and the interfacial thermal resistance between Al and GFs.

This study employed the spark plasma sintering (SPS) method to prepare GFs/Al composites. SPS is a low-temperature sintering technology. The low sintering temperature can avoid the interface reaction, and SPS can generate a plasma atmosphere to effectively destroy the oxide film on the surface of Al powders, increase new metallic contacts and necks, and reduce the porosity [17-20]. The GFs/Al composites with 10-40 vol. % of GFs were prepared. Orientations of GFs in GFs/Al composites were analyzed using the OM images; The interface reaction was detected by the XRD method; The effective thermal conductivity and the coefficient of thermal expansion of GFs/Al composites were evaluated by experimental and theoretical methods.

2.2 Experimental procedure

2.2.1 Raw materials

The raw materials consisted of Al powders and GFs. The institute of high purity chemistry offered Al powders in Japan, and Ito Graphite Industry Co., Ltd. offered the highly crystalline GFs in Japan. Figure 2-1 shows the microstructure of Al powder and GFs. Al powders show a rugby shape, and their size is uneven, while GFs show a flat surface and uniform thickness. Table 2-1 shows the chemical components of the raw materials. The purity is as high as 99.9% for Al powder and 98.8% for GFs. GFs are highly crystalline, which can hinder the chemical reaction between Al and GFs. Table 2-2 shows some physical properties and thermal conductivity of Al powder and GFs.

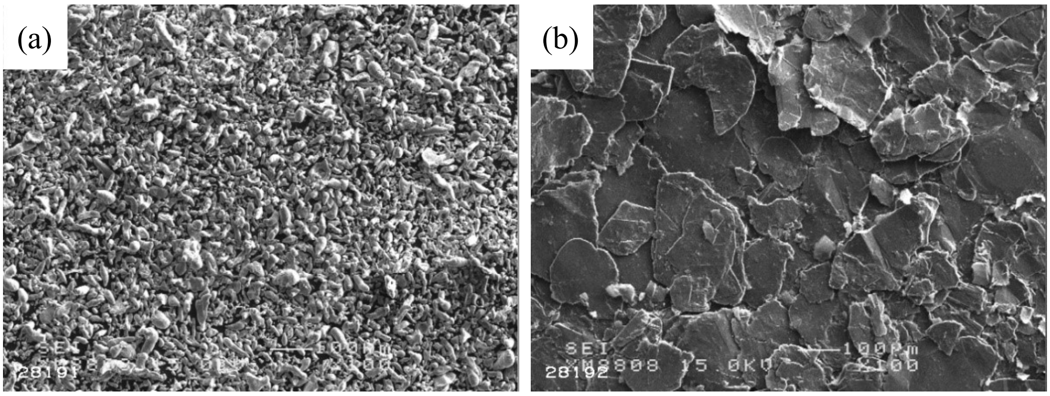

Figure 2-1 Microstructures of raw materials: (a) Al powder and (b) GFs.

Table 2 -1 Chemical components of Al and GFs.

Material	Carbon	Ash	Volatile	H_2O	Al	Cu	Fe	Si
				%				
Al					99.9	0.001	0.06	0.03
GFs (XD150)	98.78	0.61	0.61	0.27				

Table 2-2 Shape and physical properties of Al and GFs.

Materials	Shape	d	ρ	C_p	TC
		μm	g·cm^{-3}	J· kg^{-1}· K^{-1}	W·m^{-1}·K^{-1}
Al	powder	30	2.7	880	236
GFs	flake	137.02	2.23	710	880 (in-plane) 38 (out-plane)

where d is the average diameter, ρ is density, and C_p is the specific heat.

2.2.2 Preparation of graphite flakes and Al powders mixtures

The wet mixing process was used to mix Al powders and GFs. First, the Al powders, GFs, and alumina balls were filled into an aluminum jar. Subsequently, the mixtures were mixed for 2 *h* using a V-type mixer at 50rpm. Finally, the mixtures were dried in a constant temperature oven at 70 ℃. The mixing procedure of raw material Al powder and GFs was shown in Figure 2-2.

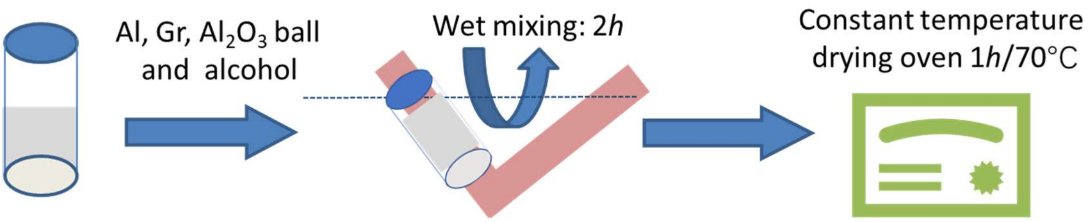

Figure 2-2 Flowchart of GFs and Al powder mixing.

According to Xu's studies [21], the morphology of the Al particle would not be destroyed when the diameter of the Alumina ball is 10 *mm*. Thus, the Alumina ball with 10 *mm* diameter was used in the mixing process of Al powder and GFs. Besides, the choice of dispersion solution is crucial for the uniform mixing of GFs and Al powder. Because the density of GFs is lower than that of Al, the low-viscosity dispersion solution may cause Al particles and GFs to separate during the mixing process; Al particles settle at the bottom of the mixed solution, while GFs are in an aggregate state. Commonly used hybrid solutions are ethanol, butanol, and acetone, and their viscosity and density are shown in Table 2-3. The sedimentation velocity (V) of Al powders with $30\mu m$ diameter in ethanol(V_e), butanol (V_b), and acetone (V_a) can be evaluated by the following equation [22]:

$$V = \ d^2 \cdot g \cdot (\rho_{Al} - \rho_s)/18\eta \qquad \ldots\ldots (2\text{-}1)$$

where the d is the diameter of Al particle, g *is* gravity, ρ_{Al} and ρ_s are the density of the Al powders and dispersion solution, and η is the viscosity of the dispersion solution.

Table 2-3 Viscosity and density of ethanol, butanol and acetone.

Dispersion solution	Butanol	ethanol	Acetone
Viscosity (η, 10^{-3} Pa·s)	2.95	1.07	0.32
Density (ρ, 10^6 g/m^3)	0.81	0.80	0.79

Figure 2-3 shows the calculated result. The sedimentation velocity is $V_b < V_e < V_a$. Therefore, butanol should be the most suitable dispersion solution in the wet mixing process. However, the higher viscosity of butanol can cause a lower drying speed of the mixed solution of GFs and Al powders, and there may be residual butanol in the mixture[21]. Moreover, the difference between V_b and V_e is not large (as shown in Figure 2-3). Thus, ethanol is used as the dispersion solution in the mixing process of GFs and Al powders.

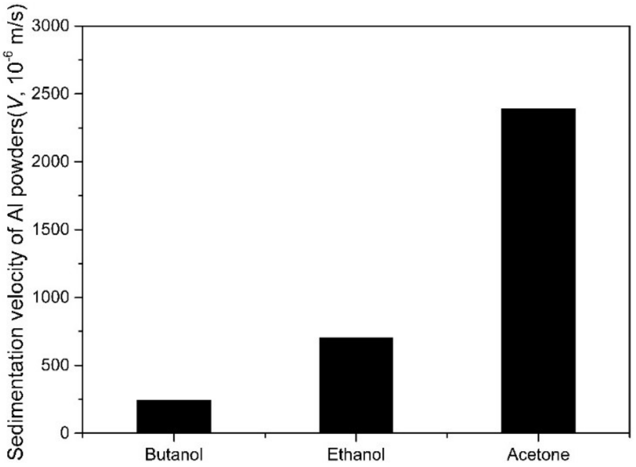

Figure 2-3 Sedimentation velocity of Al powders with $30\mu m$ diameter in ethanol, butanol, and acetone [21].

2.2.3 Fabrication of graphite flakes/Al composites by sparking plasma sintering

Figure 2-4 shows the equipment of SPS. The mixed powders were filled into a graphite mold (graphite die) to fabricate GFs/Al composites. The mold was tapped during the filling of mixed powders in order to stack GFs in layers. Then, spark plasma sintering (SPS) was conducted at 873 K, and 60 MPa pressure for 0.5 h under a vacuum of 1.3 × 10^{-2} Pa. Sintering temperature was kept below the melting point of Al to prevent the reaction between Al and GF. The temperature was increased at a rate of 200 K/min. The details of the sintering procedure were shown in Figure 2-5. A pure Al sample was fabricated by SPS under the same condition as those composites. The dimensions of the sintered GFs/Al composites were 65 × 10 × 15 mm^3.

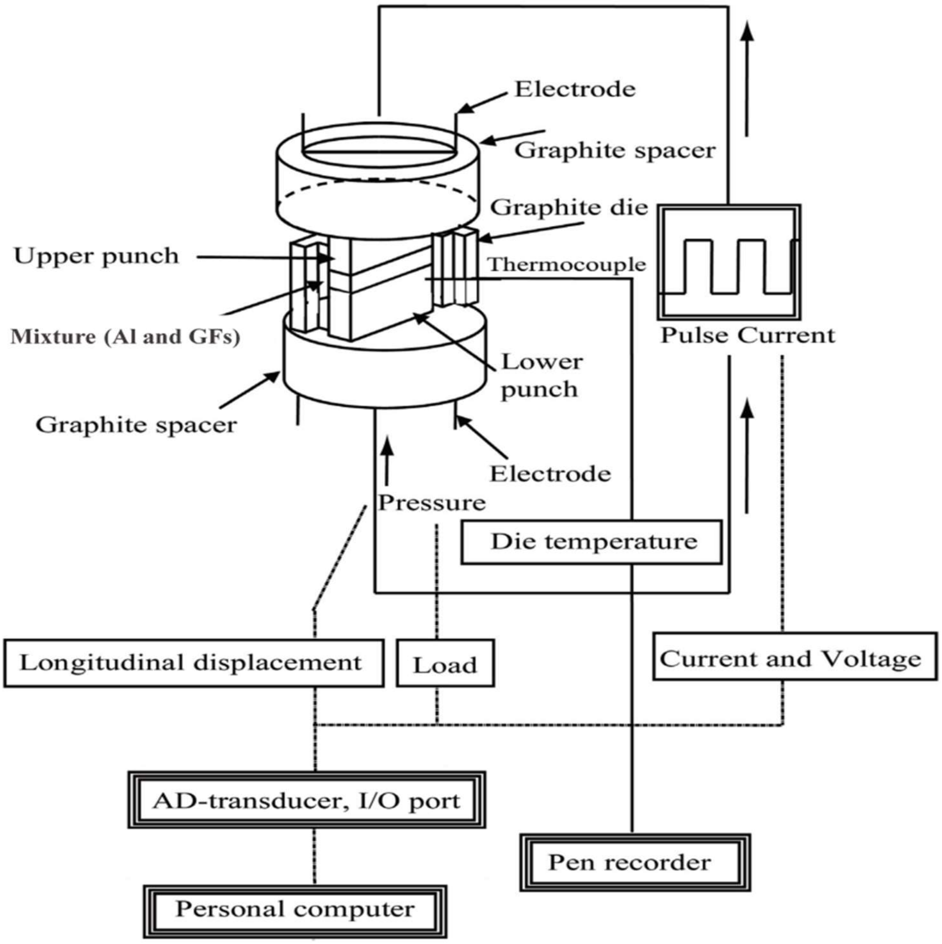

Figure 2-4 Schematic of the SPS equipment.

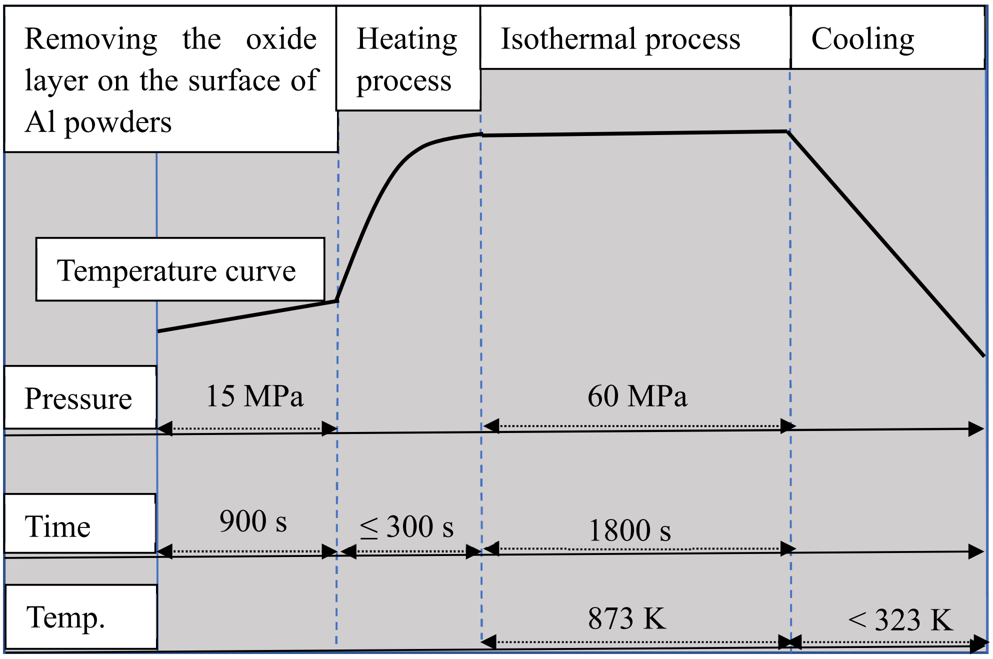

Figure 2-5 Flow chart of spark sintering process.

2.3 Evaluation methods

2.3.1 Microstructure and relative density

The electron probe micro-analyzer (EPMA) and an optical microscope (OM) were used to observe the microstructure of the composites and the mixtures of Al and GFs powders; the relative densities of composites were measured using the Archimedes method.

2.3.2 X-ray powder diffraction method

The formation of Al_4C_3 was investigated by the X-ray powder diffraction method (XRD) (D/MAX-2500/PC). The measurement conditions are listed in Table 2-4.

Table 2-4 Measurement conditions of XRD.

Target	Cu
Wavelength (10^{-10} m)	1.54056 ($K_{\alpha 1}$)
Power (kW)	≤ 18
Voltage (kV)	40
Current (mA)	200
Sampling step (degree)	0.02
Scan speed (degree/min)	1

2.3.3 Effective thermal conductivity

The effective thermal conductivities of GFs/Al composites were measured at 25 °C using a steady-state thermal-conductivity measuring device[23], as shown in Figure 2-5. The device consists of a heating end and a cooling end. The heating end includes a heating plate and a hot bar. The heating plate is connected to the cartridge heaters, and a heater controller controls the temperature (T_H). The cooling end also includes two components: a cooling plate and a cold bar. The cooling plate is connected to the water-cooled chiller through the cooling pipes. The water-cooled chiller controls the temperature of the cooling plate (T_C). There are three thermocouples fixed on the hot bar and the cold bar, respectively. The hot bar and cool bar are cylindrical copper rods with a diameter of 10 mm. When measuring the effective thermal conductivity, the sample is sandwiched between the hot bar and cold bar and contacts three thermocouples. After the temperature of the nine thermocouples reaches a steady state, the temperatures for no less than 300 seconds at a 1-second interval are collected by the data acquisition system. Subsequently, the temperature gradients of the hot bar, cold bar, and sample ($\triangle T_{\mathrm{h}}$, $\triangle T_{\mathrm{s}}$, $\triangle T_C$) are calculated by a least-square method as follows[23]:

$$\Delta T_h = \frac{\sum_{i=1}^{3} (Z_i - \bar{Z}_h)(T_i - \bar{T}_h)}{\sum_{i=1}^{3} (Z_i - \bar{Z}_h)^2}, \quad \bar{Z}_h = \frac{1}{3}\sum_{i=1}^{3} Z_i, \bar{T}_h = \frac{1}{3}\sum_{i=1}^{3} T_i$$

…… (2-2)

$$\Delta T_s = \frac{\sum_{i=4}^{6} (Z_i - Z)(T_i - \bar{T}_s)}{\sum_{i=4}^{6} (Z_i - Z_s)^2}, \quad \bar{Z}_s = \frac{1}{3}\sum_{i=4}^{6} Z_i, \quad \bar{T}_s = \frac{1}{3}\sum_{i=4}^{6} T_i$$

…… (2-3)

$$\Delta T_c = \frac{\sum_{i=7}^{9} (Z_i - \bar{Z}_c)(T_i - \bar{T}_c)}{\sum_{i=7}^{9} (Z_i - \bar{Z}_c)^2}, \quad \bar{Z}_c = \frac{1}{3}\sum_{i=7}^{9} Z_i, \quad \bar{T}_c = \frac{1}{3}\sum_{i=7}^{9} T_i$$

…… (2-4)

where Z_i is the distance between the i-th thermocouple and the heating plate, and T_i is the temperature of the i-th thermocouple. Finally, the effective thermal conductivity of the sample (λ_{eff}) can be calculated by fowling equation:

$$\lambda_{eff} = \lambda_{Cu} C(\Delta T_h + \Delta T_c)/2\Delta T_s$$

…… (2-5)

where λ_{Cu} is the thermal conductivity of copper bar (λ_{Cu} = 385 $\mathrm{Wm^{-1}K^{-1}}$); C is a correction factor, and it is a constant value (i.e., $C = 236/257$).

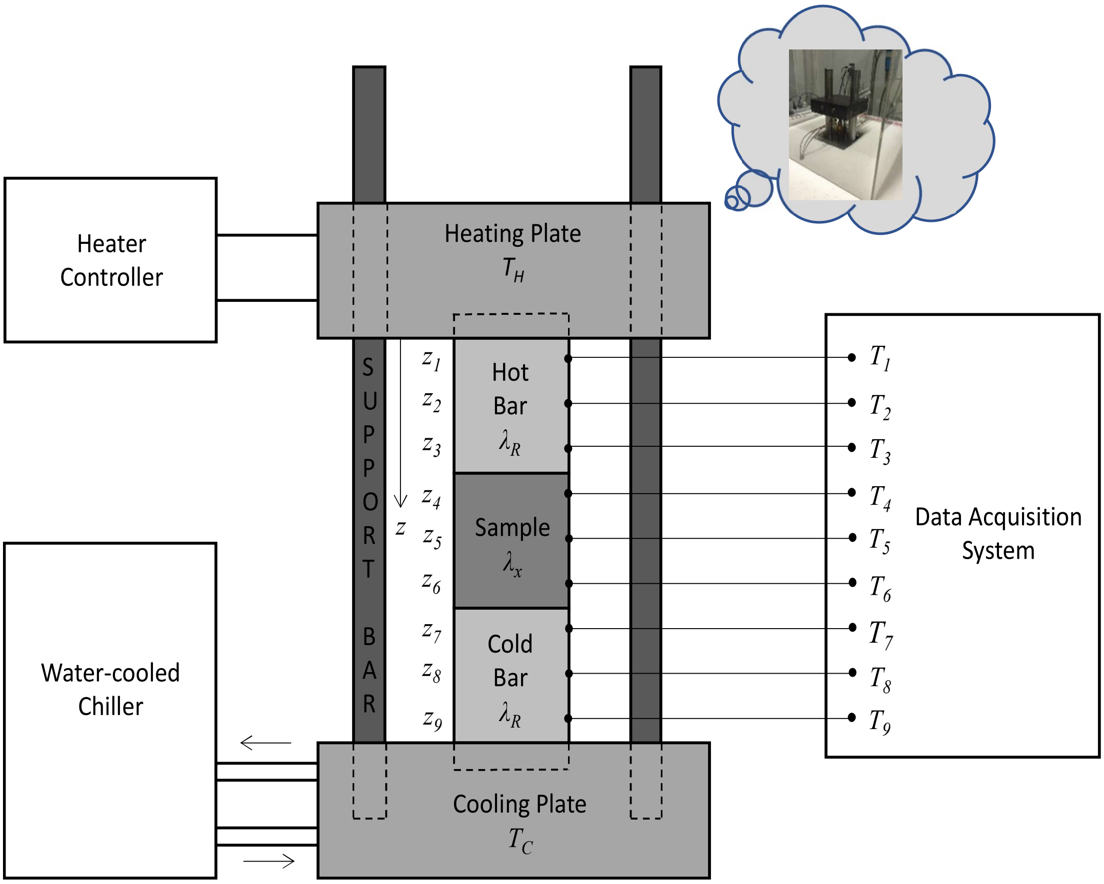

Figure 2-5 Schematic diagram of the steady-state thermal conductivity measurement device [23].

2.3.4 Coefficient of thermal expansion

The heat expansion of GFs/Al composites was measured from 25 to 200 °C by a thermal expansion meter (NETZSCH DIL 402 C).

2.4 Results and discussion

2.4.1 Microstructure characterization and orientation of GFs in composites

Figure 2-6 shows the microstructure images of the mixtures of Al and 10-40 vol.% GFs. GFs were evenly dispersed in the Al powders, and GFs in Figure 2-6 (a-d) have the same particle size. Moreover, compared with Figure 2-1, GFs did not show the obvious fracture, its average particle size was still about 130μm, and the morphology of Al powder was no obvious change.

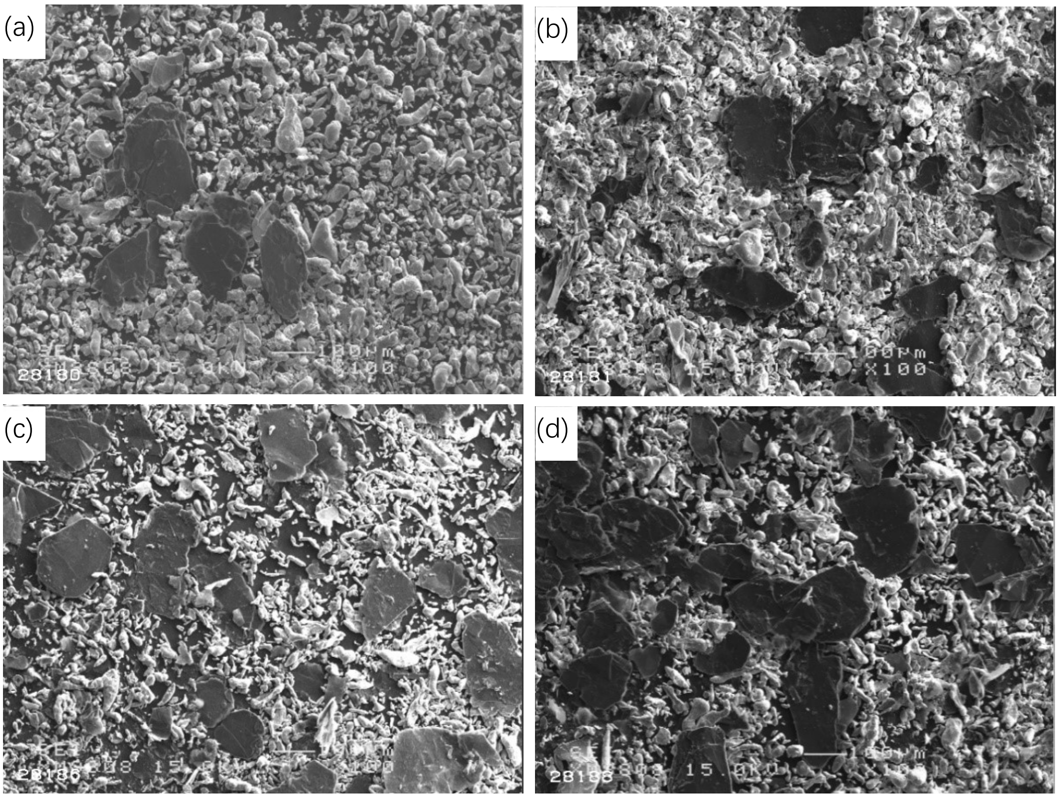

Figure 2-6 SEM images of the mixtures of Al and 10-40 vol. % GFs. 10 vol.% GFs (a), 20 vol.% GFs (b), 30 vol.% GFs (c), and 40 vol.% GFs (d).

10-40 vol. % GFs/Al composites and one pure Al sample were prepared by SPS. Their relative densities were over 98%, except for the pure Al sample being at 97%. The high relative density indicated that the fabricated GFs/Al composites were densified. The detailed values of the relative densities were listed in Table 2-5.

Table 2-5 Relative density and effective thermal conductivity (ETC) of GFs/Al composites.

Sample	Al	GFs/Al composites			
Volume fraction of GFs	0	10 vol.%	20 vol.%	30 vol.%	40 vol.%
Relative density	97.0%	99.4%	99.3%	98.6%	97.1%
ETC (λ_{eff}, $Wm^{-1}K^{-1}$)	217	248	280	313	346

Figure 2-7 depicts the shape of the samples sintered via SPS. The black arrows represent that C-plane was bearing the pressure during sintering. Therefore, GFs in the Al-matrix were stacked by layers, and the basal plane of GFs is parallel to the C surface. In order to better observe the orientation of GFs in the Al-matrix, the OM images of the GFs/Al composites were obtained from the A surface.

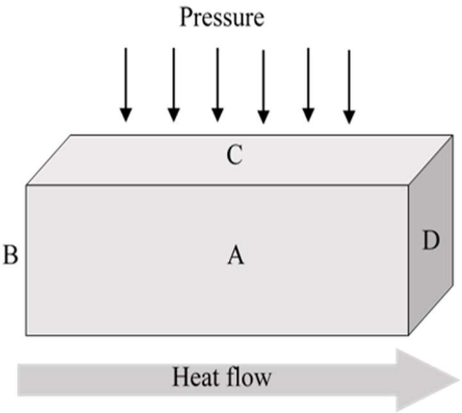

Figure 2-7 Schematic of the GFs/Al composites sintered by SPS. The grey arrow indicates that the heat flow was from B to D when measuring the ETC of the sample.

Figure 2-8 shows the OM images of 10-40 vol.% GFs/Al composites. The grey phases are of the Al matrix, and the elongated dark phases are GFs. The GFs were homogeneously distributed in the Al matrix and stacked by layers as expected. Most GFs were parallel to the heat flow direction, except for a few GFs whose basal plane direction formed an angle with the direction of the heat flow. In addition, as shown in Figure 2-8, with the increase of GFs content from 10 vol.% to 40 vol.%, GFs exhibits aggregation along the direction perpendicular to the heat flow direction, and GFs tend to form a network system by connecting GFs. As Chen et al. [12] reported, networks formed by connecting GFs can effectively improve the ETC of composites.

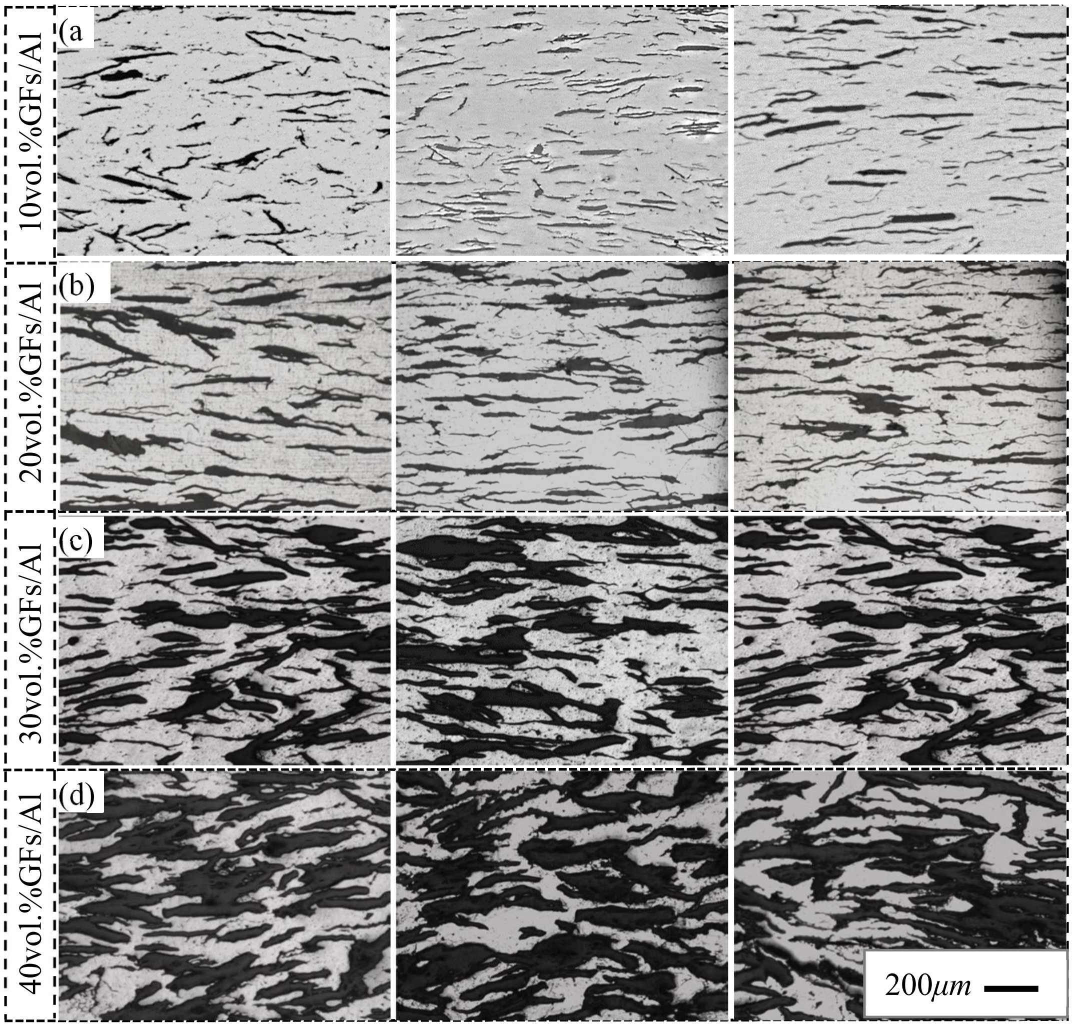

Figure 2-8 OM images of 10-40 vol.% GFs/Al composites.

An angle between GFs basal plane and heat flow direction was used to characterize the orientation of GFs in composites. The angles were counted statistically, and the results were shown in Figure 2-9. The *x*-axis showed that almost 70% of the angles were less than 10 degrees, which meant that nearly 70% of the GFs were oriented roughly parallel to the direction of heat flow. GFs parallel to each other is expected to enhance the overall thermal conduction.

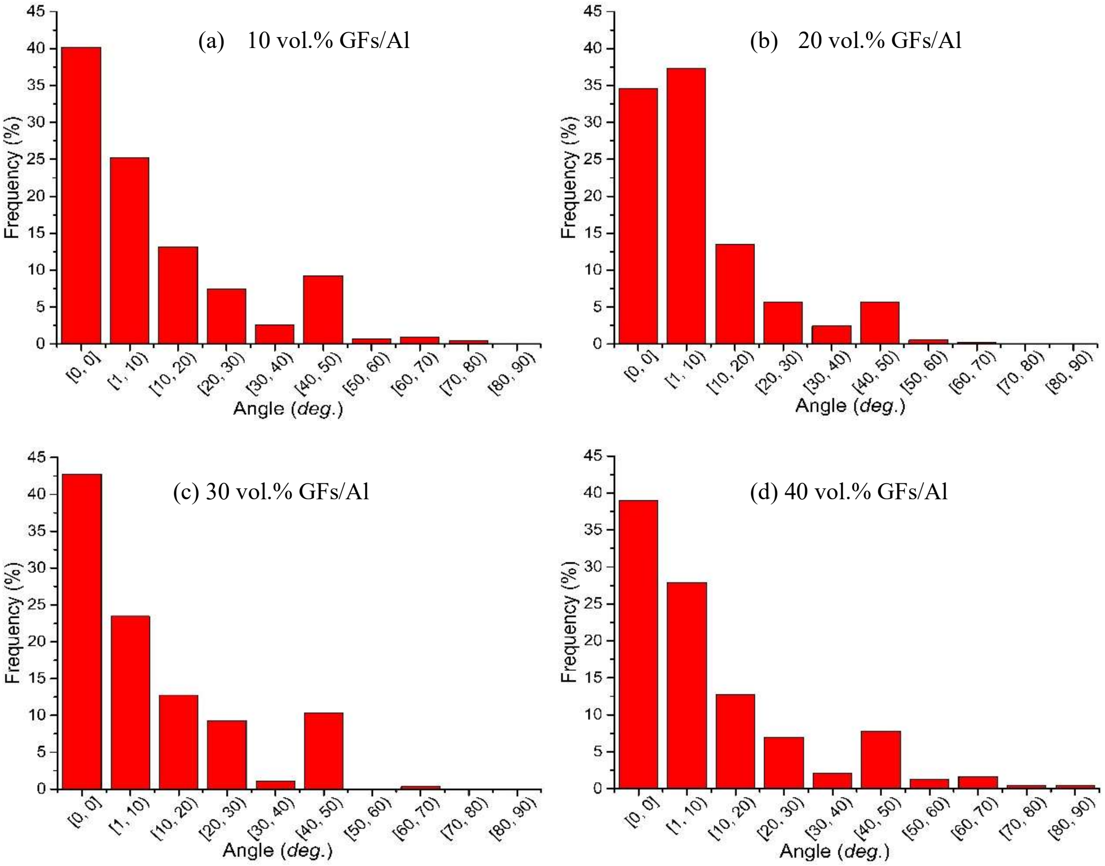

Figure 2-9 Distribution of GFs' orientation in the 10-40 vol.% GFs/Al composites, the orientation was described by the angle between GFs basal-plane direction and heat flow direction.

Figure 2-10 shows the statistical averages of the aspect ratio from the GFs in Figure 2-8. The aspect ratios values were mainly located at (1/10, 3/10]. Besides, the average diameters of GFs in composites (d) were calculated by equivalent circle area (i.e., $d = 2\sqrt{S_{GFs}/\pi}$, S is the area), the values were 1.62, 2.54, 3.89, and 5.41 *mm* in 10~40 vol.% GFs/Al composites, respectively.

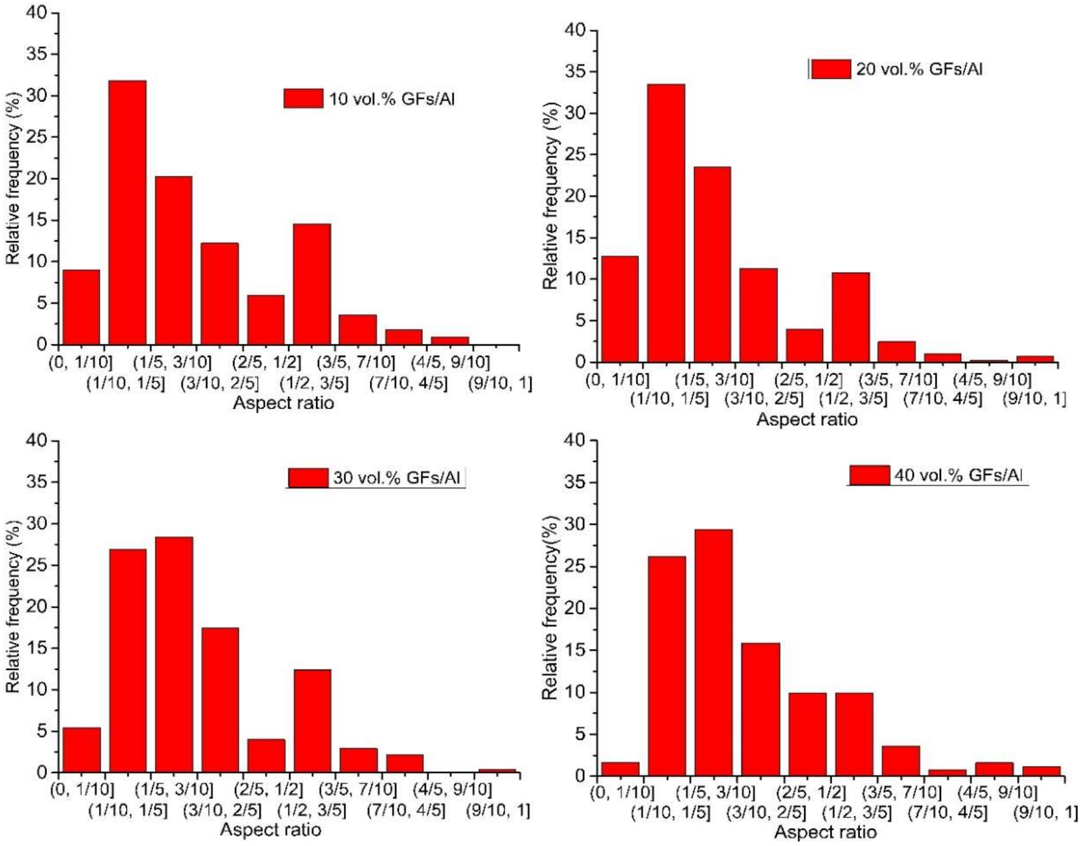

Figure 2-10 Statistical counting of the aspect ratio of GFs.

2.4.2 Interface reaction

As Etter et al. [24] reported if Al and GFs undergo a chemical reaction during the manufacturing process of GFs/Al composites, the formation of Al_4C_3 exists at the Al-GFs interface. Therefore, XRD was used to determine the interface reaction at the Al-GFs interface, as shown in Figure 2-11. The result showed that the Al_4C_3 phase was absent in 10-40 vol.% GFs/Al composites. The reason can be attributed to the following two points: first, the sintering temperature was less than the melting point of Al[25]; second, the raw material GFs was high graphitization[26]. On the other hand, high-temperature sintering methods were also commonly used to fabricate GFs/Al composites in the liquid metallurgy process. For example, Huang[9] and Chen [12] used vacuum hot pressing process to fabricate GFs/Al composites, Zhou[8] and Chang[16] used the pressure infiltration method to fabricate GFs/Al composites, and Li[13] used squeeze casting technique to fabricate GFs/Al composites. The vacuum hot pressing process, pressure infiltration, and squeeze casting belong to the liquid metallurgy process, and a higher temperature than the melting point of Al is required to fabricate GFs/Al composites. Therefore, in order to hinder the formation of Al_4C_3, a high cooling rate was used in the liquid metallurgy process to reduce the reaction time between Al and GFs. Because the formation of Al_4C_3 is associated with the reaction temperature and reaction time, according to the equation $X = \sqrt{2Kt}$, where X is the thickness of reaction layer, t is the reaction time, and K is the reaction rate related to the reaction temperature[27, 28].

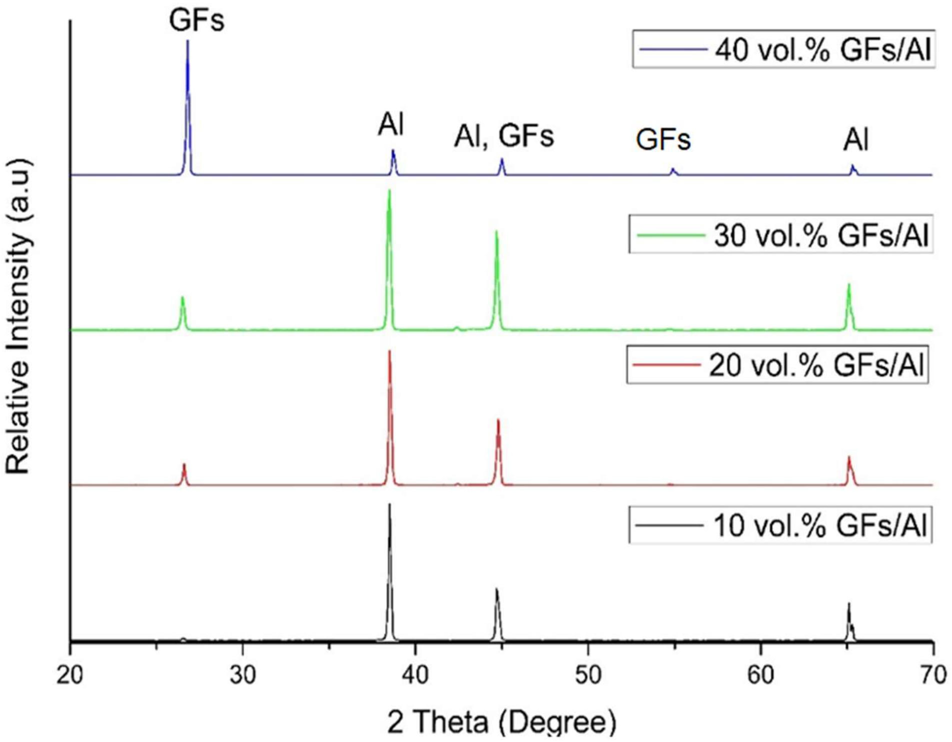

Figure 2-11 XRD analysis of GFs/Al composites.

Moreover, Huang et al. [9], Chen et al. [12], Zhou et al. [8], Chang et al. [16], and Li et al. [13] examined the microstructure and composition of the Al-GFs interface by HRTEM. Their studies revealed that an amorphous layer interface was formed at the Al-GFs interface, and the amorphous layer can be frequently observed, as shown in Figure 2-12 [9]. Therefore, we assumed the amorphous layers were formed at the Al-Gfs interfaces in the 10-40 vol.% GFs/Al composites.

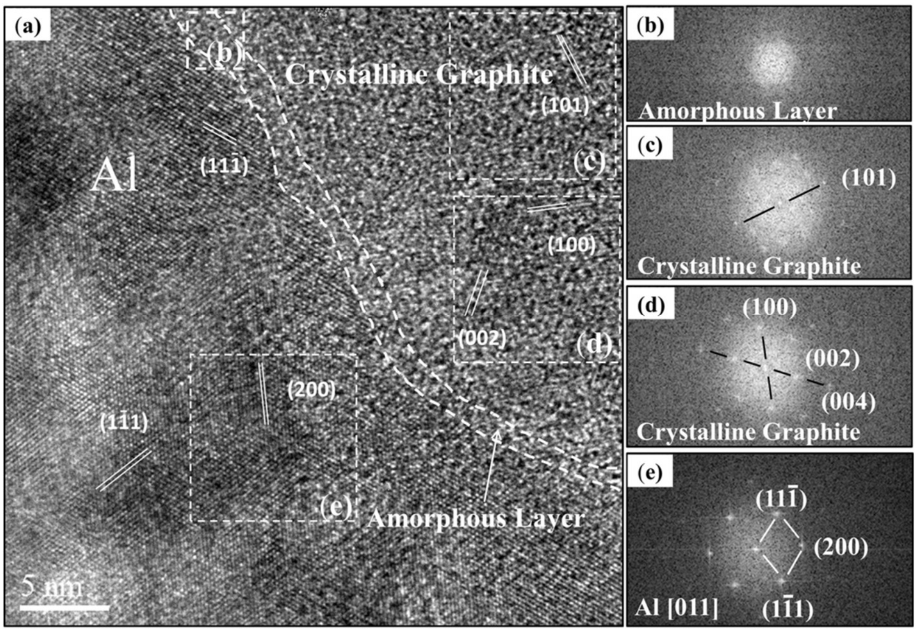

Figure 2-12 HRTEM image of the Al-GFs interface [9]: (a) HRTEM image; (b) FFT of amorphous layer; (c–d) FFT of crystalline graphite; (e) FFT aluminum.

2.4.3 Effective thermal conductivity and coefficient of thermal expansion

The effective thermal conductivities of 10-40 vol. % GFs/Al composites and the pure Al sample were measured by the steady-state thermal conductivity measuring device (see Figure 2-5). Figure 2-13 (a-d) shows the temperature variation in the ETC measurement process. The temperatures were a minor fluctuation and approximately maintained constant value, indicating that the measuring temperature was steady. Figure 2-13 (a1-d1) shows the average temperature with respect to the distance between thermocouples and the heating plate. The solid black dot is the average temperature of the thermocouples, the solid black line is the temperature gradient and is calculated using the equations (2-2) to (2-4). The dashed line is the location of the interface between the sample and hot bar or cold bar, and the corresponding temperature gap indicates the temperature difference at the interface.

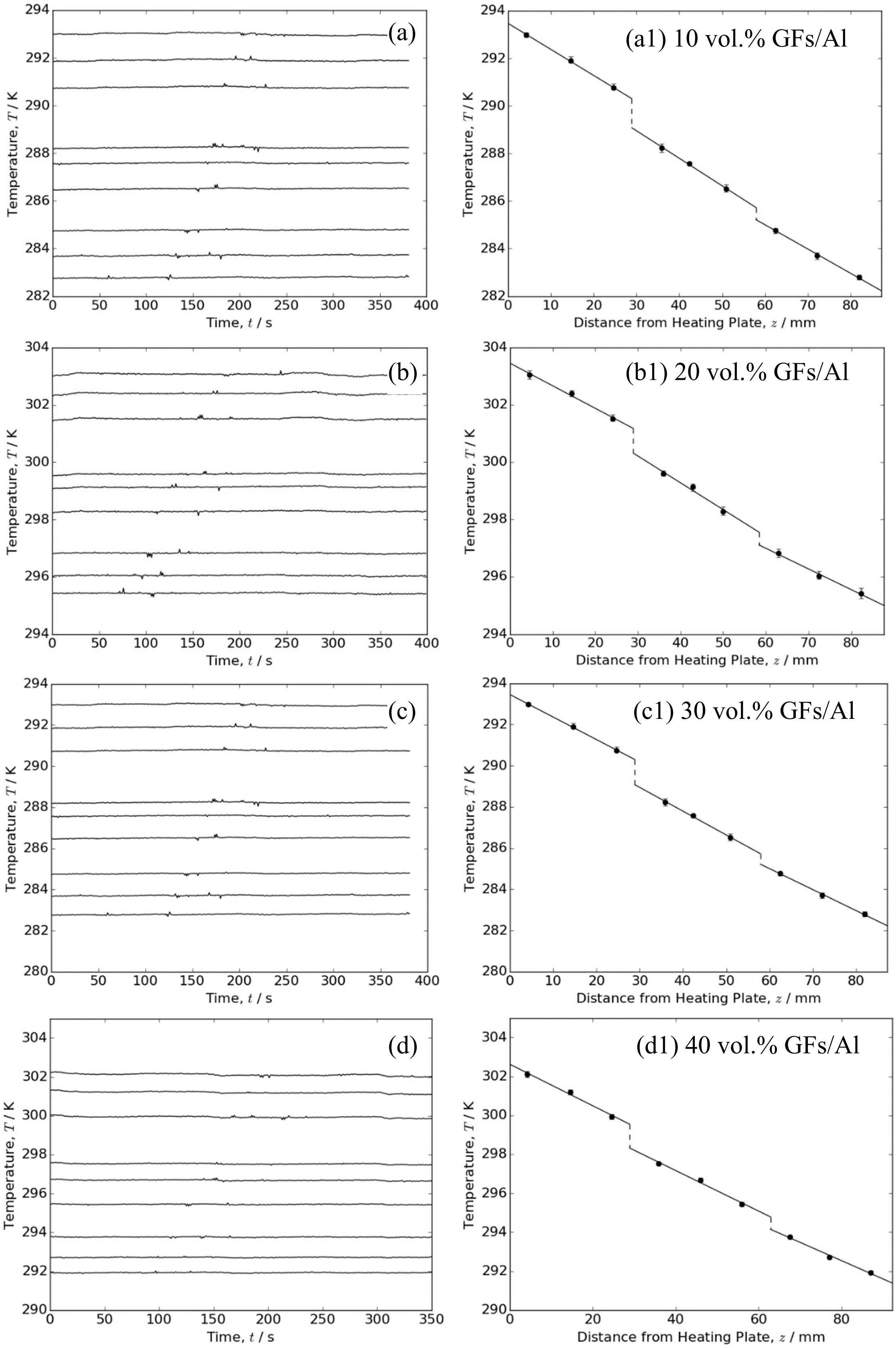

Figure 2-13 Temperature variation in the ETC measurement process of 10-40vol.%GFs/Al composites, (a-d) relationship between temperature and time, and (a1-d1) relationship between temperature and distance of the measuring points.

The ETCs of 10-40 vol.% GFs/Al composites and the pure Al sample were calculated by equations (2-2) to (2-5) and listed in Table 2-5. As a result, the TC of Al was 217 $Wm^{-1}K^{-1}$, and the ETC of GFs/Al composites λ_{eff} was increased from 248 to 346 $Wm^{-1}K^{-1}$ as GFs volume fraction increasing from 10 to 40 vol.%. Moreover, the theoretical ETC ($\lambda_{Theo.}$) of GFs/Al composites were calculated using the layer-in-parallel model[29] and the effective medium approximation (EMA) model.

The layer-in-parallel model considers the basal-plane of GFs parallel to heat flow direction, ETC ($\lambda_{Theo.}$) of GFs/Al composites is calculated as follow:

$$\lambda_{Theo.} = v_{Al\_matrix}\lambda_{Al\_matrix} + v_{GFs}\lambda_{GFs}$$

…… (2-6)

where v is volume fraction, λ is thermal conductivity, the subscript *Al_matrix* and *GFs* are Al-matrix and GFs, respectively. If to consider the effect of interfacial thermal resistance (h) on ETC, the TC of GFs (λ_{GFs}) can be replaced by λ_{GFs}^{eff}, given by[15]:

$$\lambda_{GFs}^{eff} = \lambda_{GFs}/(\frac{2\lambda_{GFs}}{hd} + 1)$$

…… (2-7)

where a value of h, 5×10^7 W m^{-2} K^{-1} [30] was used. Thus, equation (2-6) can be expressed as:

$$\lambda_{Theo.}^{h} = v_{Al\_matrix}\lambda_{Al\_matrix} + v_{GFs}\lambda_{GFs}/(\frac{2\lambda_{GFs}}{hd} + 1)$$

…… (2-8)

The EMA model considers the geometrical factor and h to evaluate the ETC of composites, and the equation can be expressed as [15]:

$$\lambda_{EMA} = \lambda_{Al}(1 + \frac{v_{GFs}}{\frac{\pi}{4p}(1 - v_{GFs}) + \frac{1}{\frac{\lambda_{GFs}^{eff}}{\lambda_{Al}} - 1}}$$

(2-9)

where p is the aspect ratio of GFs, the value was 5 (see Figure 2-10).

Moreover, the measured relative densities of GFs/Al composites and pure Al sample were less than 1, indicating that some pores were embedded in the samples. However, equations (2-6), (2-8), and (2-9) do not include the effect of pores on the ETC. Therefore, the pores in this study were presumed to be embedded within the Al matrix. The TC of the pure Al sample and the Al-matrix, λ_{Al_eff}, can be calculated by the equation derived by Landauer [31]. The equation was as follow:

$$\lambda_{Al\_eff} = \frac{1}{4}[\lambda_p(3v_p - 1) + \lambda_{Al}(3v_{Al} - 1) + \left([\lambda_p(3v_p - 1) + \lambda_{Al}(3v_{Al} - 1)]^2 + 8\lambda_p\lambda_{Al}\right)^{\frac{1}{2}}] \qquad \text{...... (2-10)}$$

where the λ_{Al} is the thermal conductivity of Al powder, λ_p is the thermal conductivity of pores, v_p and v_{Al} are the volume fraction of Al and pores. In addition, the values of λ_{Al}, λ_p, v_p, and v_{Al} were listed in Table 2-6.

Table 2-6 Calculation parameters in equation (2-7).

Samples	v_{Al}	v_p	λ_p	λ_{Al}	λ_{Al_eff}	λ_{Al_matrix}
Al	0.97	0.03	0.214	228	217	-
10 Vol.% GFs/Al	0.994	0.06	0.214	228	225.9	225.9
20 Vol.% GFs/Al	0.993	0.07	-	-	225.6	225.6
30 Vol.% GFs/Al	0.986	0.014	-	-	223.2	223.2
40 Vol.% GFs/Al	0.971	0.029	-	-	218.1	218.1

First, by substituting the measured TC (217 $Wm^{-1}K^{-1}$) and the relative density (0.97) of the pure Al sample into the equation (2-10), the TC of Al powder (λ_{Al}) was calculated for 228 $Wm^{-1}K^{-1}$. Second, the TCs of the Al-matrix for 10-40 vol.% GFs/Al composites were calculated by substituting the λ_{Al}, λ_p, v_p, and v_{Al} from Table 2-6 into equation (2-10). The calculated values of λ_{Al_eff} were 225.9, 225.6, 223.2, and 218.1 $Wm^{-1}K^{-1}$ for 10-40 vol.% GFs/Al composites, respectively. λ_{Al_eff} was equal to λ_{Al_matrix}. Therefore, the theoretical ETC of the 10-40 vol.% GFs/Al composites can be calculated by equations (2-6), (2-8) and (2-9), and the values were listed in Table 2-7.

Table 2-7 Theoretical ETC of GFs/Al composites.

ETC	GFs/Al composites			
	10 Vol.% GFs	20 Vol.% GFs	30 Vol.% GFs	40 Vol.% GFs
$\lambda_{eff.}$ ($Wm^{-1}K^{-1}$)	248	280	313	346
$\lambda_{Theo.}$ ($Wm^{-1}K^{-1}$)	291	357	420	483
$\lambda^{h}_{Theo.}$($Wm^{-1}K^{-1}$)	289	353	417	480
λ_{EMA} ($Wm^{-1}K^{-1}$)	271	320	370	422

Figure 2-14 shows a comparison between the measured and theoretical ETCs. The theoretical value was considerably higher than the measured value λ_{eff}, and the deviation between the measured and the theoretical ETCs increased with GFs content. The largest deviation between the measured and theoretical ETCs was up to 28.4%.

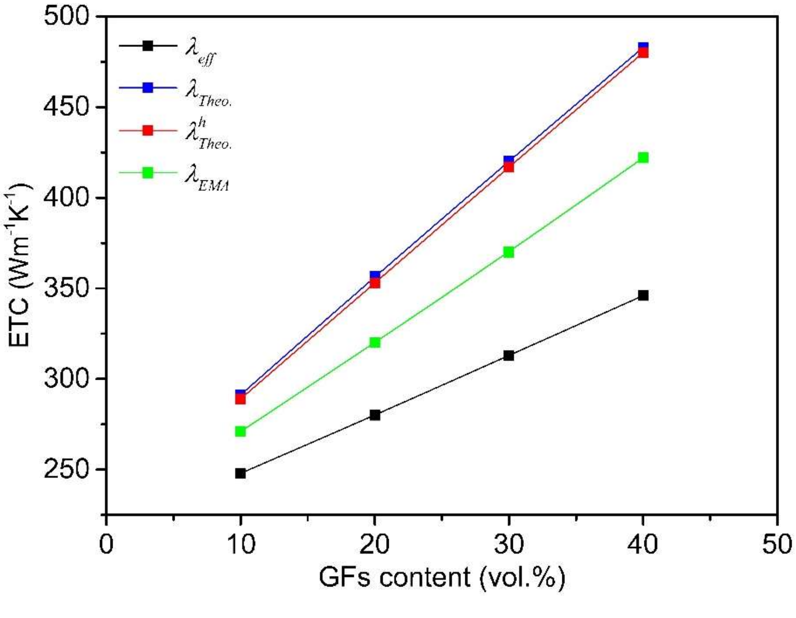

Figure 2-14 Comparison of measured and theoretical ETC of 10-40 vol.% GFs/Al composites.

The value of λ_{Theo} was approximately equal to that of λ_{Theo}^{h}, indicating that the effect of interfacial thermal resistance on the ETC was small. The deviation between λ_{Theo} and λ_{eff} can be attributed to the effects of the orientation of GFs and the interface thermal resistance. In addition, Zhou et al.[15] calculated the ETC of GFs/Al composites using the EMA approach, and the calculated values were agreed with the experimental values. However, the λ_{EMA} were greater than the λ_{eff}. The deviation between them can be attributed to the effect of the orientation of GFs.

The coefficient of thermal expansion of 10-40 vol.% GFs/Al composites were measured along the direction parallel to the basal plane of GFs, and the results were summarized in Table 2-7. Figure 2-15 (a) shows the thermal expansion at temperatures from 25 to 200 °C. The thermal expansion of GFs/Al composites decreased with the GFs content under the temperature from 25 to 200 °C, indicating that the coefficient of thermal expansion of GFs/Al composites decreases with the increase of GFs content.

Table 2-7 Coefficient of thermal expansion.

Samples	Al	GFs	GFs content (vol.%)			
			10	20	30	40
$\alpha_{Exp.}$ (ppm/K)	23.8[12]	-1.5[34-35]	26.2	24.4	23.4	22.1
$\alpha_{Com.}$ (ppm/K)			21.27	18.74	16.21	13.68
		25[37]	23.92	24.04	24.16	24.8

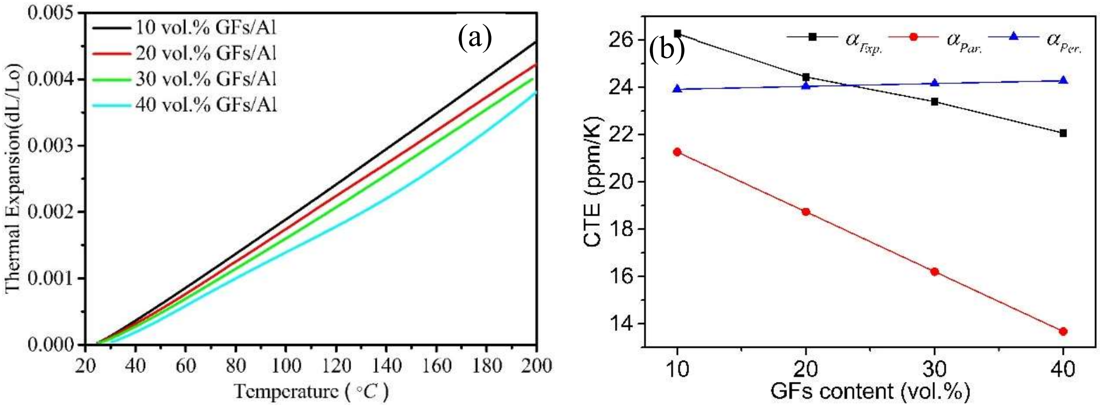

Figure 2-15 Thermal expansion variation versus temperature (a), coefficient of thermal expansion (CTE) versus GFs content (b).

To calculate the coefficient of thermal expansion of composite, the commonly used theoretical models include the rule of mixture [12], Turner model [32], Kerner model [33], and Schapery model [34]. But Chen et al.[12] and Kurita et al.[11] revealed that the Turner and Kerner models were failed to predict the coefficient of thermal expansion of 10-40 vol.% GFs/Al composites. Thus, the mixture rule here was used to evaluate the coefficient of thermal expansion of 10-40 vol.% GFs/Al composites. The rule of the mixture is described as follows:

$$\alpha_{Com.} = v_{Al\_matrix}\alpha_{Al\_matrix} + v_{GFs}\alpha_{GFs} \quad \text{…… (2-8)}$$

where α is the coefficient of thermal expansion, and the subscript *Com.* is composite. The coefficient of thermal expansion is 23.8 ppm/K[12] for Al and -1.5ppm/K[35, 36] for GFs along the basal plane direction and 25ppm/K [37] for GFs along the direction perpendicular to the basal plane. The calculated values were list in Table 2-7. Figure 2-15 (b) shows the measured and calculated coefficient of thermal expansion. The black line represents the experimental coefficient of thermal expansion, the experimental values of thermal expansion decreased with the increase of GFs content. The blue line presents the coefficient of thermal expansion parallel to GFs basal plane, the red line presents the coefficient of thermal expansion perpendicular to GFs basal plane. Because the orientations of some GFs were disorder in composites, the coefficient of thermal expansion of composite should be located between the red and bule lines. However, the black line was intersected with the blue line. The experimental values for the composites with 10-20 vol.% GFs were higher than the calculated values, and the experimental values exceeded even the coefficient of thermal expansion of Al and GFs (25 ppm/K[37] along the direction perpendicular to the basal plane). Besides, the black line was around the blue line, the reasons can be attributed to pores embedded in the composites and the disorder orientations of GFs.

2.5 Summary

GFs/Al composites with 10-40 vol.% GFs were fabricated by using spark plasma sintering in this chapter. Subsequently, the following studies on the GFs/Al composites were completed: 1) The relative density of composites was measured by the Archimedes method; 2) The microstructure images analyzed the distribution and orientation of GFs in the composites; 3) The formation of Al_4C_3 was investigated by XRD method; 4), the effective thermal conductivities of the composites were measured using a steady-state thermal conductivity measurement device and calculated by theoretical methods; 5) The coefficient of thermal expansions of the composites were measured by a thermal dilatometer (NETZSCH DIL 402 C) and calculated by the rule of mixture. Finally, the following conclusions were obtained.

1) The relative density was up to 99% for the GFs/Al composites; with the GFs content up to 40%, the relative density of composites decreased to 97.1%.
2) GFs were homogeneously distributed and stacked by layers in the Al matrix. The orientations of nearly 70% GFs were parallel to each other. Moreover, with the GFs content up to 40 vol.%, GFs exhibits aggregation and tend to form the network system by connecting GFs.
3) The formation of Al_4C_3 was absent in the 10-40 vol.% GFs/Al composites, but amorphous layers at the Al-GFs interface may be formed at the interface.
4) The measured effective thermal conductivities were 248, 280, 313, and 346 W m^{-1} K^{-1} for 10-40 vol.% GFs/Al composites, respectively. The effects of orientation of GFs and interface thermal resistance caused the ETC of GFs/Al composites to be lowered by 28.4%.
5) The experimental values of the coefficient of thermal expansion were 26.2, 24.4, 23.4, and 22.1 ppm/K for 10-40 vol.% GFs/Al composites, respectively. Moreover, because of the effects of the pores embedded in composites and the disorder orientations of GFs, the experimental values for the composites with 10-20 vol.% GFs were higher than the calculated values perpendicular to GFs basal plane, and the experimental values exceeded even the coefficient of

thermal expansion of Al and GFs (25 ppm/K along the direction perpendicular to the basal plane.

2.6 References

[1] Chung D. Properties of Carbon Fibers, Carbon Fiber Composites. Butterworth-Heinemann, Newton 1994.

[2] Miracle D. Metal matrix composites–from science to technological significance. Composites science and technology. 2005;65(15-16):2526-40.

[3] Shirvanimoghaddam K, Hamim SU, Karbalaei Akbari M, Fakhrhoseini SM, Khayyam H, Pakseresht AH, et al. Carbon fiber reinforced metal matrix composites: Fabrication processes and properties. Composites Part A: Applied Science and Manufacturing. 2017;92:70-96.

[4] Qu X-h, Zhang L, Wu M, Ren S-b. Review of metal matrix composites with high thermal conductivity for thermal management applications. Progress in Natural Science: Materials International. 2011;21(3):189-97.

[5] Inagaki M, Kaburagi Y, Hishiyama Y. Thermal management material: graphite. Advanced Engineering Materials. 2014;16(5):494-506.

[6] Biercuk M, Llaguno MC, Radosavljevic M, Hyun J, Johnson AT, Fischer JE. Carbon nanotube composites for thermal management. Applied physics letters. 2002;80(15):2767-9.

[7] Kidalov S, Shakhov F. Thermal Conductivity of Diamond Composites. Materials. 2009;2(4):2467-95.

[8] Zhou C, Ji G, Chen Z, Wang M, Addad A, Schryvers D, et al. Fabrication, interface characterization and modeling of oriented graphite flakes/Si/Al composites for thermal management applications. Materials & Design. 2014;63:719-28.

[9] Huang Y, Ouyang Q, Guo Q, Guo X, Zhang G, Zhang D. Graphite film/aluminum laminate composites with ultrahigh thermal conductivity for thermal management applications. Materials & Design. 2016;90:508-15.

[10] Xue C, Bai H, Tao PF, Wang JW, Jiang N, Wang SL. Thermal conductivity and mechanical properties of flake graphite/Al composite with a SiC nano-layer on graphite surface. Materials & Design. 2016;108:250-8.

[11] Kurita H, Miyazaki T, Kawasaki A, Lu Y, Silvain J-F. Interfacial microstructure of

graphite flake reinforced aluminum matrix composites fabricated via hot pressing. Composites Part A: Applied Science and Manufacturing. 2015;73:125-31.

[12] Chen JK, Huang IS. Thermal properties of aluminum–graphite composites by powder metallurgy. Composites Part B: Engineering. 2013;44(1):698-703.

[13] Li W, Liu Y, Wu G. Preparation of graphite flakes/Al with preferred orientation and high thermal conductivity by squeeze casting. Carbon. 2015;95:545-51.

[14] Zhou C, Chen D, Zhang XB, Chen Z, Zhong SY, Wu Y, et al. The roles of geometry and topology structures of graphite fillers on thermal conductivity of the graphite/aluminum composites. Physics Letters A. 2015;379(5):452-7.

[15] Zhou C, Huang W, Chen Z, Ji G, Wang ML, Chen D, et al. In-plane thermal enhancement behaviors of Al matrix composites with oriented graphite flake alignment. Composites Part B: Engineering. 2015;70:256-62.

[16] Chang J, Zhang Q, Lin Y, Wu G. Layer by layer graphite film reinforced aluminum composites with an enhanced performance of thermal conduction in the thermal management applications. Journal of Alloys and Compounds. 2018;742:601-9.

[17] KURAMOTO H, MATSUGI K, KAWAHARA K, YANAGISAWA O. Densification rate of Cu-Al2O3 composite in the spark sintering process. Nippon Kinzoku Gakkaishi (1952). 2003;67(10):528-37.

[18] Xu Z-F, Choi Y-B, Matsugi K, Li D-C, Sasaki G. Mechanical and thermal properties of vapor-grown carbon fiber reinforced aluminum matrix composites by plasma sintering. Materials transactions. 2010:1002010992-.

[19] Kubota M. Properties of nano-structured pure Al produced by mechanical grinding and spark plasma sintering. Journal of Alloys and Compounds. 2007;434:294-7.

[20] Xie G, Ohashi O, Yoshioka T, Song M, Mitsuishi K, Yasuda H, et al. Effect of interface behavior between particles on properties of pure Al powder compacts by spark plasma sintering. Materials transactions. 2001;42(9):1846-9.

[21] Xu Z. Fabrication and Properities Evaluations of VGCNFs/Al Composites[D]. Department of Mechanical Science and Engineering Graduate School of Engineering Hiroshima University, Japan 2010.

[22] Bochniak W. The Cottrell-Stokes law for FCC single crystals. Acta metallurgica et materialia. 1993;41(11):3133-40.

[23] Sugio K, Yamada R, Choi YB, Sasaki G. Effect of the Interfacial Thermal Resistance on Effective Thermal Conductivity of Al/SiC Particle-Dispersed Composites. Materials Science Forum. 2016;879:1889-94.

[24] Etter T, Schulz P, Weber M, Metz J, Wimmler M, Löffler JF, et al. Aluminium carbide formation in interpenetrating graphite/aluminium composites. Materials Science and Engineering: A. 2007;448(1-2):1-6.

[25] Mizuuchi K, Inoue K, Agari Y, Morisada Y, Sugioka M, Tanaka M, et al. Processing of diamond particle dispersed aluminum matrix composites in continuous solid–liquid co-existent state by SPS and their thermal properties. Composites Part B: Engineering. 2011;42(4):825-31.

[26] Maire J, Mering J. Graphitization of soft carbons. Chemistry and physics of carbon. 1970;6:125-90.

[27] Genlgl L, Chiai S, Peng H, Gao L, Sun J, Sun Z. FABRICATION OF NANOCRYSTALLINE ZrO, PARTICLE REINFORCED ALUMINUM ALLOY COMPOSITE BY SQUEEZE CASTING ROUTE. 1997.

[28] Bakshi SR, Agarwal A. An analysis of the factors affecting strengthening in carbon nanotube reinforced aluminum composites. Carbon. 2011;49(2):533-44.

[29] Truong H, Zinsmeister GE. Experimental study of heat transfer in layered composites. International Journal of Heat and Mass Transfer. 1978;21(7):905-9.

[30] Schmidt AJ, Collins KC, Minnich AJ, Chen G. Thermal conductance and phonon transmissivity of metal–graphite interfaces. Journal of Applied Physics. 2010;107(10):104907.

[31] Landauer R. The electrical resistance of binary metallic mixtures. Journal of Applied Physics. 1952;23(7):779-84.

[32] Turner PS. Thermal-Expansion Stresses in Reinforced Plastics. Research of the National Bureau of Standards. 1946;37:239-50.

[33] KERNER EH. The Elastic and Thermo-elastic Properties of Composite Media. Proc Phys Soc Sec B. 1956;69(8):808-13.

[34] Schapery RA. Thermal Expansion Coefficients of Composite Materials Based on Energy Principles. Journal of Composite Materials. 1968;2(3):380-404.

[35] Nelson J, Riley D. The thermal expansion of graphite from 15 c. to 800 c.: Part I. Experimental. Proceedings of the Physical Society. 1945;57(6):477.

[36] Riley D. The thermal expansion of graphite: part II. Theoretical. Proceedings of the Physical Society. 1945;57(6):486.

[37] Tsang DKL, Marsden BJ, Fok SL, Hall G. Graphite thermal expansion relationship for different temperature ranges. Carbon. 2005;43(14):2902-6.

Chapter 3

Relationship between the thermal conductivity of GFs in 3D and 2D microstructure images

3.1 Introduction

Graphite flakes (GFs) reinforced aluminum (Al) matrix composites (GFs/Al) are light-weight, low cost, and exhibit superior thermal properties, such as high effective thermal conductivity (ETC) and low coefficient of heat expansion (CTE). Therefore, GFs/Al composites are considered as one of the most promising thermal management materials. However, the ETCs of GFs/Al composites are affected by the orientation of GFs, the interfacial thermal resistance, and the interface reaction between Al and GFs [1-5]. In particular, the interfacial thermal resistance and the orientation of GFs have a great effect on the ETCs of GFs/Al composites, which results in lower experimental ETCs than expected.

The commonly used theoretical methods using to calculate the ETC of GFs/Al composites include mixing rules [1, 2, 6], Fricke equation[7], effective medium approach (EMA)[8], and three-dimensional simulations [9, 10]. However, the orientations of GFs in composites are uncontrollable diverse in the composites. Therefore, obtaining the reliable ETC of GFs/Al composites is challenging using those theoretical models. Three-dimensional (3D) image simulations can be used to calculate the ETC of GFs/Al composites well. But the 3D-images simulation is expensive and has low timeliness because the 3D models are constructed using the ultra-high-resolution X-ray computed tomography images [11]. In addition, two-dimensional (2D) image simulations are also often used to evaluate the ETC of composites [12, 13], and it is simple, saves time, and is low cost. However, the orientation of GFs in the 2D microstructure images may not be equivalent to that in the 3D microstructure images due to a 2D microstructure image cannot provide the information in the depth direction with respect to the viewing surface. Therefore, the ETC calculated by the 2D image-based simulation is not reliable.

In order to develop a 2D image simulation method for calculating the ETC of GFs/Al composites considering the orientation of GFs and the interfacial thermal resistance, the relationship between the orientation of GFs in 2D and 3D models was investigated. Moreover, the ETC of the 10 vol % GFs/Al composite was calculated using 2D image-based simulation, and the interfacial thermal conductance at the GFs-Al interface was calculated using the reversed method.

3.2 Calculation Procedure

3.2.1 Creating 3D and 2D models

Figure 3-1 shows the flowchart of the calculation procedure for comparing the orientations of GFs in the 2D model and the corresponding 3D model. First, some 3D models were created, as shown in Figure 3-2 (a).

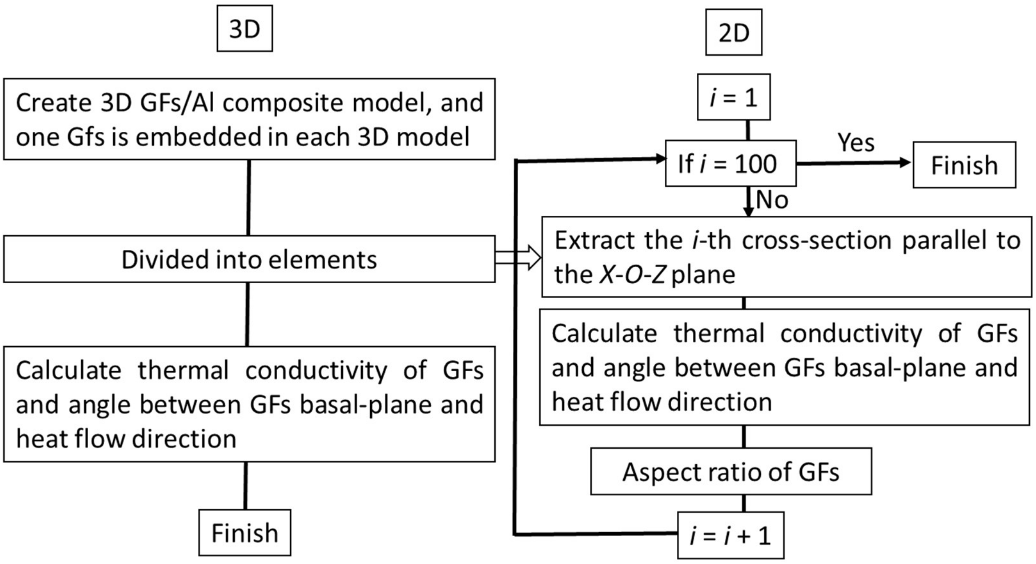

Figure 3-1. Flowchart of the calculation procedure for comparing the orientations of GFs in two- and three-dimensional models.

The dimensions of the 3D model were 110 × 100 × 100 elements in the *X*-, *Y*-, and *Z*-axis. One GFs was embedded in the center of one 3D model. The shape of GFs was an elliptical cylinder, the semi-major axis(*D*) was 40 elements, and the semi-minor axis (*d*) was 20 elements. The thickness of the ellipse (*T*) was 10 elements. As shown in Figure 3-2 (b), the GFs in the 3D model can rotate θ_x, θ_y, and θ_z around the *X*-, *Y*-, and *Z*-axis, respectively, according to the right-hand rotation rule. The rotated coordinates (x, y, z) were calculated using the following rotation matrix:

$$\begin{bmatrix} x \\ y \\ z \end{bmatrix} = \begin{bmatrix} cos\theta_z & -sin\theta_z & 0 \\ sin\theta_z & cos\theta_z & 0 \\ 0 & 0 & 1 \end{bmatrix} \begin{bmatrix} cos\theta_y & 0 & sin\theta_y \\ 0 & 1 & 0 \\ -sin\theta_y & 0 & cos\theta_y \end{bmatrix} \begin{bmatrix} 1 & 0 & 0 \\ 0 & cos\theta_x & -sin\theta_x \\ 0 & sin\theta_x & cos\theta_x \end{bmatrix} \begin{bmatrix} x_0 \\ y_0 \\ z_0 \end{bmatrix} \quad \ldots\ldots (3\text{-}1)$$

where (x_0, y_0, z_0) is the initial coordinates. The x and y are set to coincide with the semi-major axis(D) and semi-minor axis(d) of GFs, respectively. In this study, the orientation of GF in 3D models was represented by the angles α, β, and γ, which is the difference between the global coordinate X-Y-Z and the local coordinate x-y-z. In other words, α, β, and γ were the angles between the axes (X-x, Y-y, and Z-z), and their values were calculated as follows:

$$\alpha = \arccos\left(\frac{\overrightarrow{Ox}\cdot\overrightarrow{OX}}{|\overrightarrow{Ox}||\overrightarrow{OX}|}\right),\ \beta = \arccos\left(\frac{\overrightarrow{Oy}\cdot\overrightarrow{OY}}{|\overrightarrow{Oy}||\overrightarrow{OY}|}\right),\ \gamma = \arccos\left(\frac{\overrightarrow{Oz}\cdot\overrightarrow{OZ}}{|\overrightarrow{Oz}||\overrightarrow{OZ}|}\right) \quad \text{......} \ (3\text{-}2)$$

where $\overrightarrow{OX}$, $\overrightarrow{OY}$ and $\overrightarrow{OZ}$ are the unit coordinate vectors, and their values are (1,0,0), (0,1,0), and (0,0,1), respectively. $\overrightarrow{Ox}$, $\overrightarrow{Oy}$, and $\overrightarrow{Oz}$ were calculated using equation (3-1).

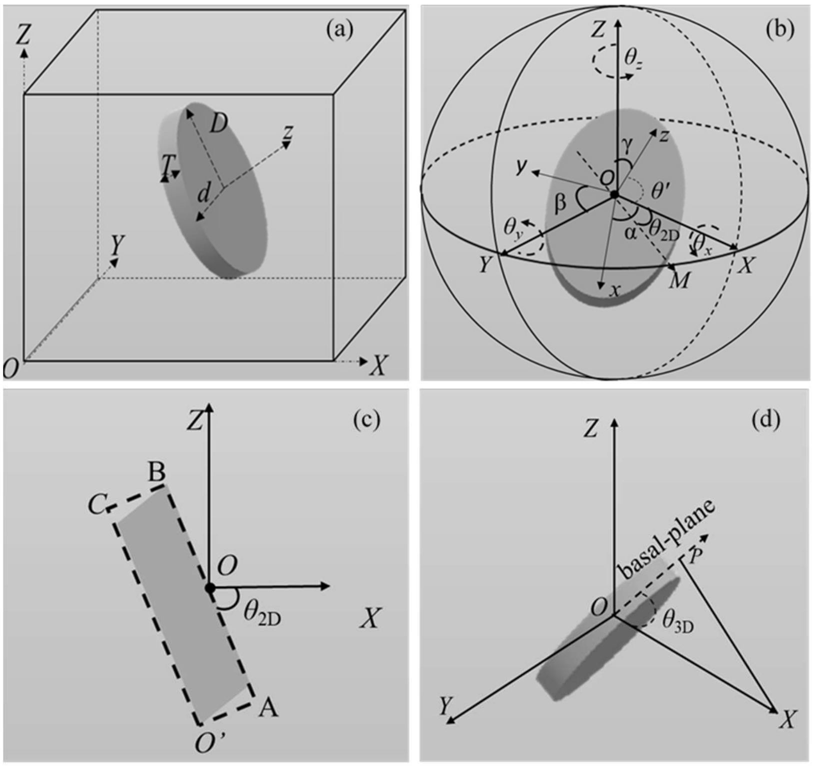

Figure 3-2. Three-dimensional model and orientation of GFs. a) 3D model of GFs/Al composites; b) Orientation of GFs in 3D model; c) Orientation of GFs in the 2D cross-sectional image; (d) Describing the angle between of GFs basal plane and heat flow; α, β, γ and θ' are the angles between the axes, x-X, y-Y, z-Z, and z-X, respectively; α, β and

γ are within [0,90°]; *OM* is the line perpendicular to *OY* and *Oz*, and θ_{2D} is the angle between *OX* and *OM*; Rectangle *O'ABC* is the minimum bounding rectangle of GFs, θ_{2D} is the angle between *X*-axis and *AB*; *XP* is perpendicular to the basal plane of GFs.

Second, as many 2D cross-sections were extracted from each 3D model as possible, the cross-sections were extracted parallel to the *X-O-Z* plane, as shown in Figure 3-2 (b). The shape of GFs may be irregular in the cross-sectional images; therefore, a minimum bounding rectangle (*O'ABC*, see Figure 3-2 (c)) of the GFs was introduced to measure the orientation of the GFs. The orientation of GFs in cross-sectional images was defined by the angle (θ_{2D}) between GFs and the *X*-axis, as shown in Figure 3-2 (c). θ_{2D} was calculated from the 2D cross-sectional images, excluding GFs smaller than 5 × 5 elements. Moreover, the aspect ratio (*R*) of GFs in each extracted 2D cross-sectional image was also calculated.

3.2.2 TC calculation of GFs

Here, the heat flow direction in the 3D model and the 2D cross-sectional image was set to be along the *X*-axis. The TC of GFs along the *X*-axis thus can be calculated as follows [14]:

$$\lambda_{//} = \lambda_a \, [1 - (1 - \frac{\lambda_c}{\lambda_a}) sin^2\theta]$$
$$\lambda_{\perp} = \lambda_a \, [1 - (1 - \frac{\lambda_c}{\lambda_a}) cos^2\theta]$$

…… (3-3)

where $\lambda_{//}$ is the TC of GFs parallel to the *X*-axis direction, λ_a is the TC of GFs in the basal-plane direction (880 W m^{-1} K^{-1}), and λ_c is the TC of GFs in the out-of-plane direction (38 W m^{-1} K^{-1}). θ in the 3D models refers to the orientations of GFs relative to the heat flow direction, which are equal to the angles between the *X*-axis and basal plane of the GFs (Figure 3-2 (d)), and it is denoted as θ_{3D}. Thus, θ_{3D} can be obtained as follows:

$$\theta_{3D} = |90-\theta'|, \ \theta' = \arccos\left(\frac{\overrightarrow{Oz}\cdot\overrightarrow{OX}}{|\overrightarrow{Oz}||\overrightarrow{OX}|}\right)$$

…… (3-4)

where *θ*’ is the angle between *X*-axis and *z*-axis (Figure 3-2 (b)). In other words, *θ*’ is the angle between the heat flow direction and the normal vector of the basal plane, and θ_{3D} is the angle between the heat flow direction and basal plane.

In the 2D cross-section images, *θ* refers to the angle between the cross-section of the GFs and the *X*-axis, i.e., $\theta = \theta_{2D}$. Therefore, θ_{2D} can be calculated mathematically, as follows:

$$\theta_{2D} = \arccos\left(\frac{\overrightarrow{OM} \cdot \overrightarrow{OX}}{|\overrightarrow{OM}||\overrightarrow{OX}|}\right)$$

…… (3-5)

where *OM* is the line perpendicular to *OY* and *Oz* (Figure 3-2 (b)), and θ_{2D} is in the range [0, 90).

3.2.3 Image-based simulation method

The finite-volume method was employed to calculate the 2D temperature distributions. The temperature of the elements can be calculated using the following equation [13]:

$$T_{x,y}^{n+1} = T_{x,y}^{n} + \frac{\Delta t}{\rho c}\left(\frac{q_{x+1,y}^{n} - q_{x-1,y}^{n}}{\Delta x} + \frac{q_{x,y+1}^{n} - q_{x,y-1}^{n}}{\Delta y}\right)$$

…… (3-6)

where $T_{x,y}^{n}$ is the temperature of the element at (*x*, *y*) coordinates, $T_{x,y}^{n+1}$ is the temperature of the element at (*x*, *y*) coordinates after a time Δt, *ρ* is the density, *c* is the specific heat, and $\triangle x$ and $\triangle y$ are the sizes of the elements. The heat flow q^{n} can be calculated as follows:

$$q_{x+1,y}^{n} = \lambda\left(\frac{T_{x+1,y}^{n} - T_{x,y}^{n}}{\Delta x}\right), \qquad q_{x-1,y}^{n} = \lambda\left(\frac{T_{x,y}^{n} - T_{x-1,y}^{n}}{\Delta x}\right)$$

$$q_{x,y+1}^{n} = \lambda\left(\frac{T_{x,y+1}^{n} - T_{x,y}^{n}}{\Delta y}\right), \qquad q_{x,y-1}^{n} = \lambda\left(\frac{T_{x,y}^{n} - T_{x,y-1}^{n}}{\Delta y}\right)$$

When the heat flow q^{n} move at the GFs-Al interface:

$$q_{x+1,y}^{n} = h(T_{x+1,y}^{n} - T_{x,y}^{n}), \qquad q_{x-1,y}^{n} = h(T_{x,y}^{n} - T_{x-1,y}^{n})$$

$$q^n_{x,y+1} = h(T^n_{x,y+1} - T^n_{x,y}), \qquad q^n_{x,y-1} = h(T^n_{x,y} - T^n_{x,y-1})$$

…… (3-7)

where h is the interfacial thermal conductance between different materials.

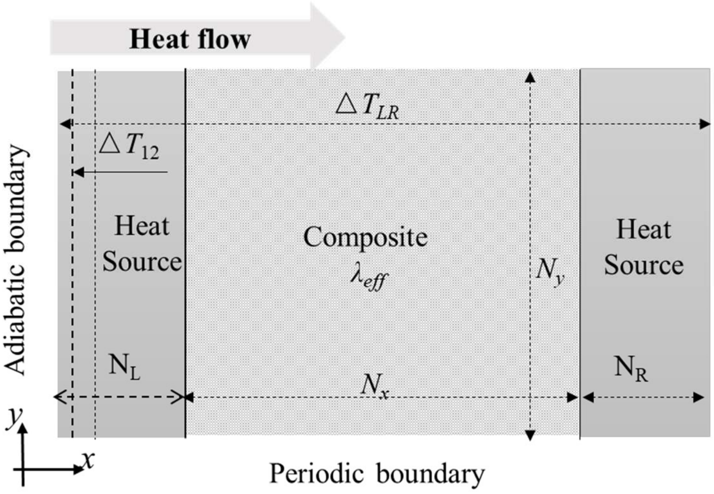

Figure 3-3 Simulation model for the ETC calculation.

Figure 3-3 shows the schematics of the simulation model. The model is a sandwich structure consisting of two heat sources and a composite part. The composite part was obtained from the microstructure image of the GFs/Al composites. The size of the composite part ($N_x \times N_y$) was 450 × 600 elements, and that of the heat source was 5 × 600 elements ($N_L = N_R = 5$ elements). The size of each element was 1.18×10^{-6} m. Both the upper and lower sides were the periodic boundary, while the left and right sides were the adiabatic boundary. The temperatures of the left and right edge elements were fixed at 301 K and 300 K, respectively. The initial temperature of the other elements was set at 300 K, and the temperature was iteratively updated until the temperature variation was lower than 10^{-13} K. The temperature distribution at this moment was in a steady state, and the ETC of the GFs/Al composite, λ_{eff}, was calculated as follows:

$$\lambda_{\text{eff}} = \frac{\lambda_{\text{Al}} \triangle T_{12} N_x}{\triangle T_{LR} - N_L \triangle T_{12} - N_R \triangle T_{12}}$$

…… (3-8)

where λ_{Al} is the TC of the Al matrix, $\triangle T_{12}$ is the average value of the temperature difference between the first and second columns, and N_L, N_R, N_x, and N_y are the number of elements along the corresponding direction.

3.3 Results and Discussions

3.3.1 Orientations of GFs in 2D and 3D models

The 2D orientations of GFs, i.e., θ_{2D}, were obtained from Equation (5) and the 2D-cross-sectional images, respectively. Moreover, the θ_{2D} from the 2D-cross-sectional images extracted from the same 3D model showed the same values. Figure 3-4 shows a comparison of θ_{2D} obtained from the mathematical calculation and the 2D-cross-sectional images. The solid line is the θ_{2D} from Equation (3-5), and the open circles are the θ_{2D} from the 2D-cross-sectional images. Thus, the open circles are on the solid line ($x = y$), confirming that the θ_{2D} values obtained from the 2D cross-sectional images were reliable.

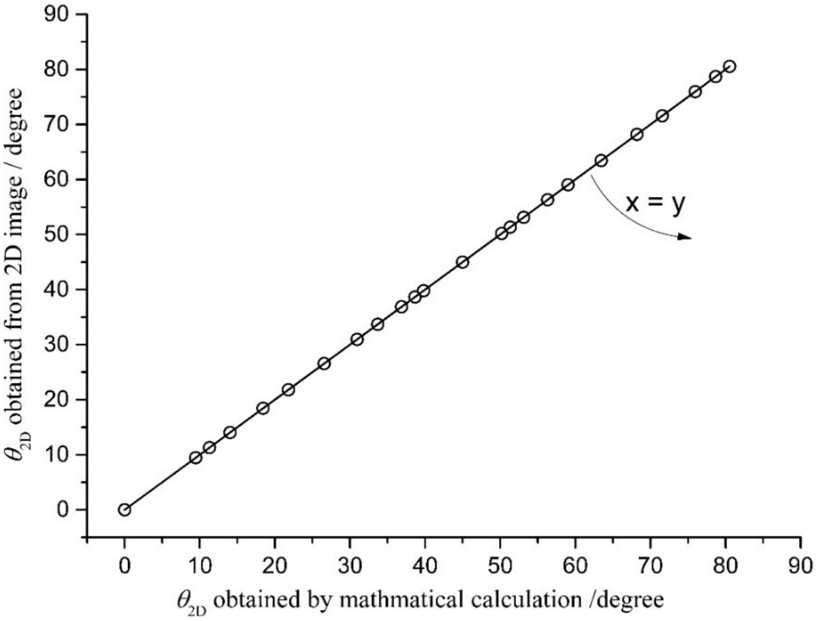

Figure 3-4 Comparison of the θ_{2D} obtained from the mathematical calculation and 2D cross-sectional image.

The angle difference between θ_{2D} and θ_{3D} ($\theta_{2D\text{-}3D}$) was calculated. Figure 3-5 (a) shows $\theta_{2D\text{-}3D}$ in a standard regular triangle. The black dots represent the calculated points. The black color indicates that the value of $\theta_{2D\text{-}3D}$ is zero. The other colors indicate that the value of $\theta_{2D\text{-}3D}$ is between 0° and 90°. A few black dots were in the black region, whereas the rest were distributed in other colored regions. In the triangle, most of the $\theta_{2D\text{-}3D}$ in the triangle was under 20°, but there were some $\theta_{2D\text{-}3D}$ that exceeded 40°. Additionally, the difference between the TCs of GFs in the 2D and 3D models (i.e., $TC_{3D\text{-}2D}$) was shown in Figures 3-5 (b). The maximum value of $TC_{3D\text{-}2D}$ was up to 840 W m^{-1} K^{-1}. Moreover, comparing Figure 3-5 (a) and Figure 3-5 (b), the value of $TC_{3D\text{-}2D}$ can be large, even if the value of $\theta_{2D\text{-}3D}$ was small in the triangle.

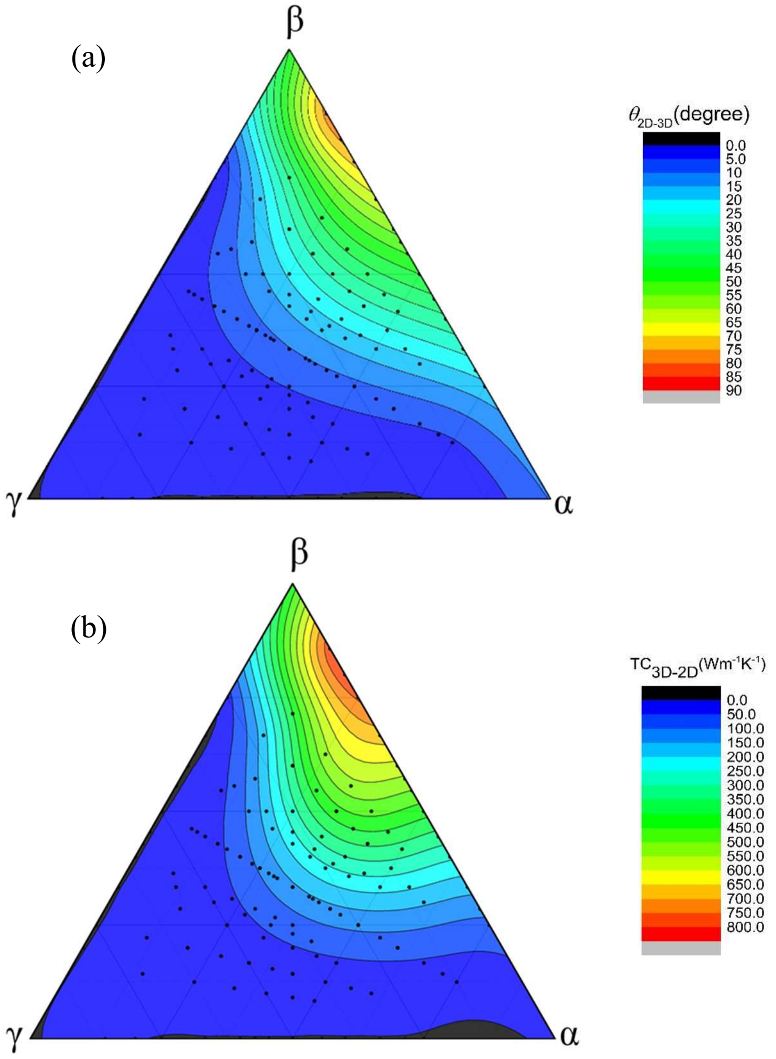

Figure 3-5. Orientation difference of GFs in the 2D cross-sections and 3D models (a); TC difference of GFs in the 2D cross-sections and 3D models (b).

3.3.2 Relationship between the aspect ratio of GFs and the orientation of GFs

The aspect ratio of the GFs (R) in each 2D cross-section extracted from the same 3D model showed different values, while the corresponding θ_{2D} was the same as each other. In order to investigate the relationship between the aspect ratios and the orientations, the average arithmetic value of R was calculated and marked as $\bar{R}$, i.e., $\bar{R} = \frac{\sum R}{\sum i}$ (i was the number of R). Figure 3-6 shows the relationships between $\theta_{2D\text{-}3D}$, $\bar{R}$,and θ_{2D}.

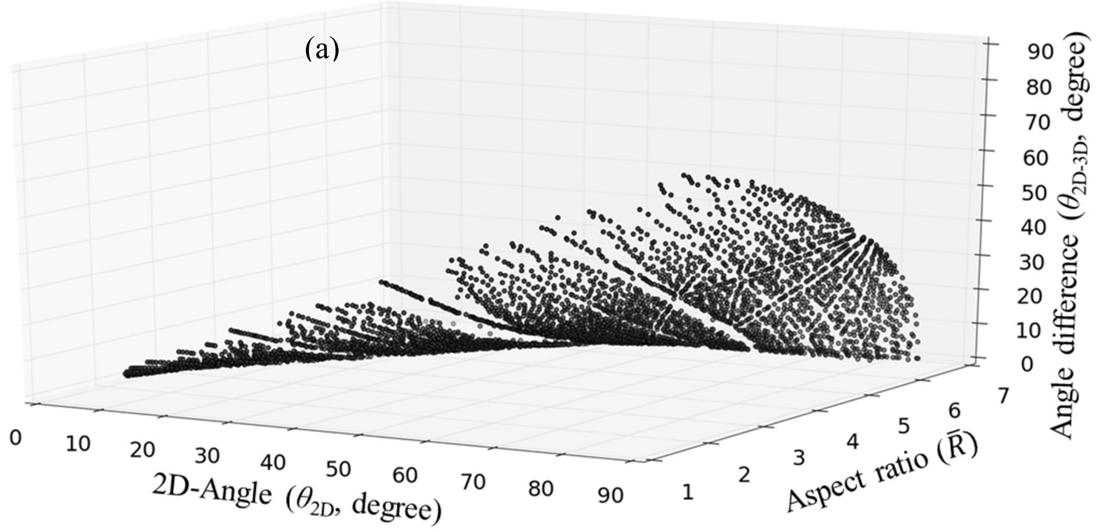

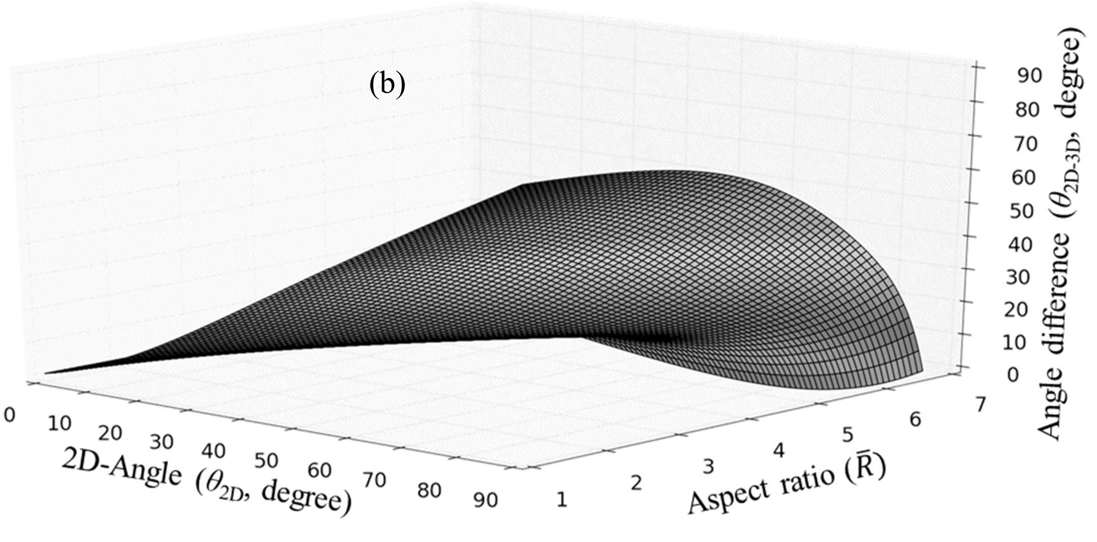

Figure 3-6. Relationship between the θ_{2D}, $\theta_{2D\text{-}3D}$ and $\bar{R}$. Scatter image (a); Nonlinear polynomial fitting surface (b).

Figure 3-6 (a) shows that all data was distributed on a curved surface, which means that anyone of the $\theta_{2D\text{-}3D}$, $\bar{R}$ and θ_{2D} can be expressed by using the curved surface function. Subsequently, a similar curved surface was obtained by the surface fitting method, as shown in Figures 3-6 (b). The function of the fitted curved surface can be expressed as:

$$\theta_{fitted-3\mathrm{D}} = \theta_{2\mathrm{D}} - [\mathrm{A}_0 + \mathrm{A}_1 \times \theta_{2\mathrm{D}} \times f - A_4 \times \theta_{2\mathrm{D}} \times e^{(\mathrm{A}_5 \times \bar{R})}]$$

$$f = \frac{1}{1 + e^{-(\mathrm{A}_2 + \mathrm{A}_3 \times \theta_{2\mathrm{D}} - \bar{R})}}$$

$$(0^{\circ} < \theta_{2\mathrm{D}} < 90^{\circ}, 1 < \bar{R} < 6.7)$$

…… (3-9)

The coefficients, A_0, A_1, A_2, A_3, A_4, A_5, were listed in Table 3-1, $\theta_{\text{fitted-3D}}$ represents the angle between GFs basal-plane and heat flow direction in the 3D model. This function can effectively convert θ_{2D} into θ_{3D} and improve the reliability of the ETC calculated by 2D image simulations. The deviation between the $\theta_{\text{fitted-3D}}$ and θ_{3D} was within 6°.

Table 3-1. Calculation parameters in equation (3-9)

Equation	A_0	A_1	A_2	A_3	A_4	A_5
(3-6)	0.64	0.86	0.62	0.059	1.80	3.15

To determine the reliability of function Equation (3-9), a comparison between the TCs of GFs calculated with θ_{3D} and $\theta_{\text{fitted-3D}}$ was conducted. Figure 3-7 shows the GFs' TCs calculated with θ_{3D} and $\theta_{\text{fitted-3D}}$ by Equation (3-3). The solid black line represents TCs calculated with θ_{3D}, and grey circles were for $\theta_{\text{fitted-3D}}$. The circles were tightly bound around the solid black line, and the errors were so minor that they can be ignored. Thus, Figure 3-7 indicated that equation (3-6) is successful in converting θ_{2D} to θ_{3D}.

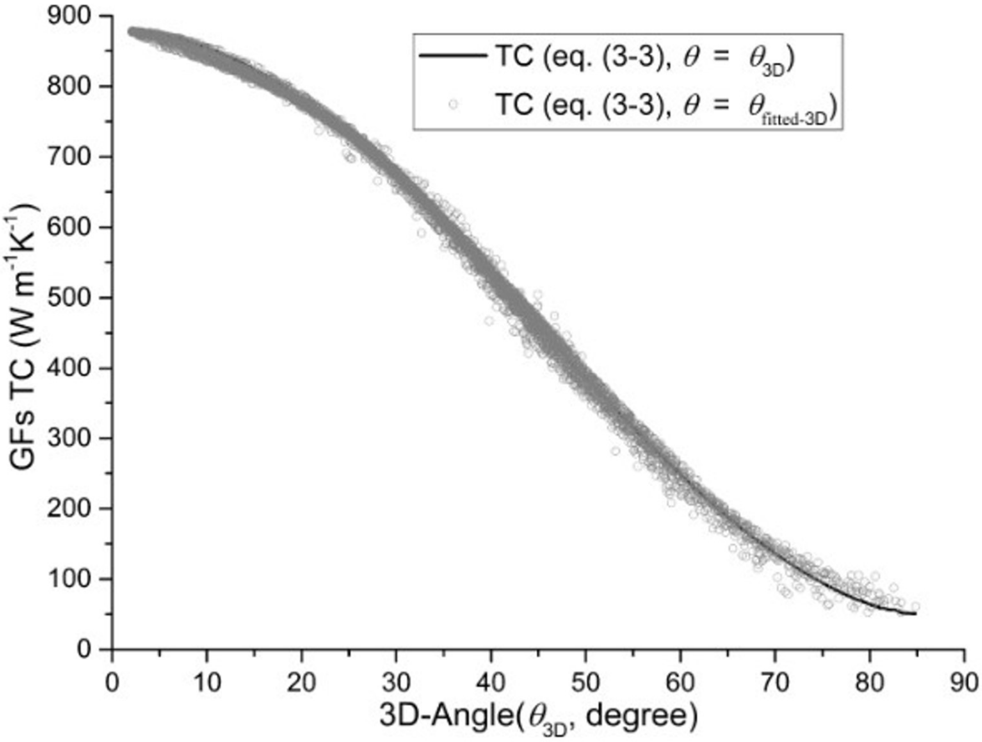

Figure 3-7. TC of GFs calculated by equation (3-3), θ was equal to the $\theta_{3\mathrm{D}}$ for the black solid line and $\theta_{fitted\text{-}3\mathrm{D}}$ for the gray circle.

3.3.3 ETC calculation of GFs/Al composites

10 vol.% GFs/Al composites were fabricated via spark plasma sintering. The diameter of the GFs was 137.02 μm (98% purity), and the average particle of Al powder was 30 μm (99.9% purity). The relative density of the samples was 99.4%. The ETC of the sample, measured using a steady-state thermal-conductivity-measuring device, was 238 W m^{-1} K^{-1}. The microstructures of the samples were observed using an optical microscope. Figure 3-8 (a) shows the microstructures of the 10 vol.% GFs/Al composites. To evaluate the TC distributions of GFs in the microstructures, different colors were used to mark the GFs according to the orientations of the GFs, as shown in Figure 3-8(b). For example, the red color indicates that the orientation of the GFs was parallel to the heat flow direction, and the GFs had high TC; the other colors indicate that the GFs tilt from the heat flow direction, decreasing TC.

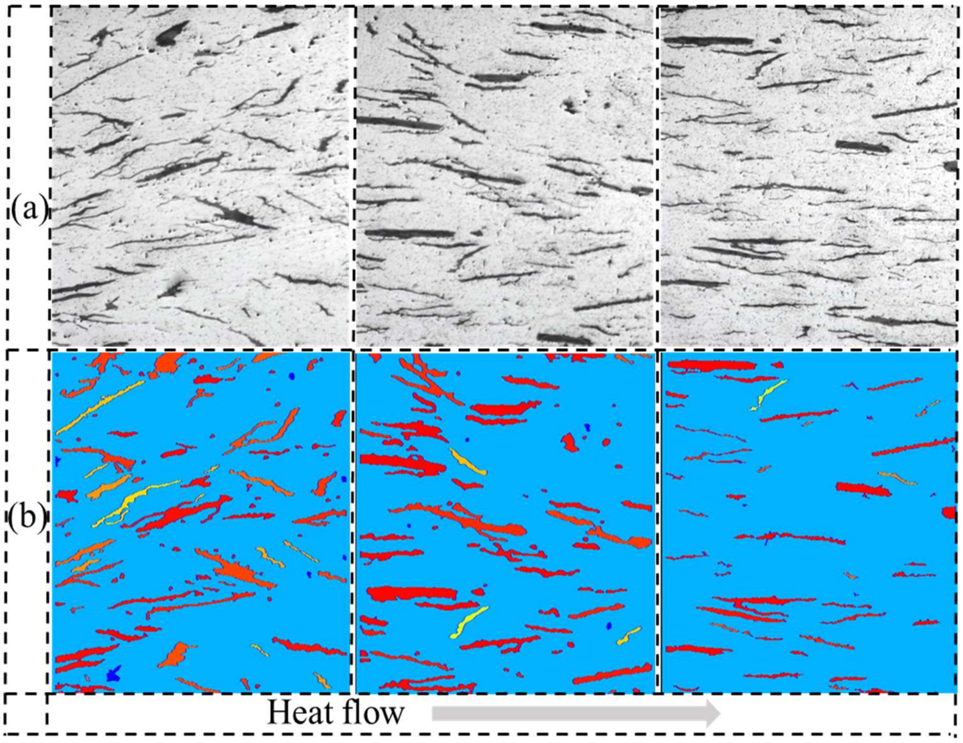

Figure 8 Microstructure images of the 10 vol.% GFs/Al composite; (a) The OM images; (b) Distribution of the GFs TC.

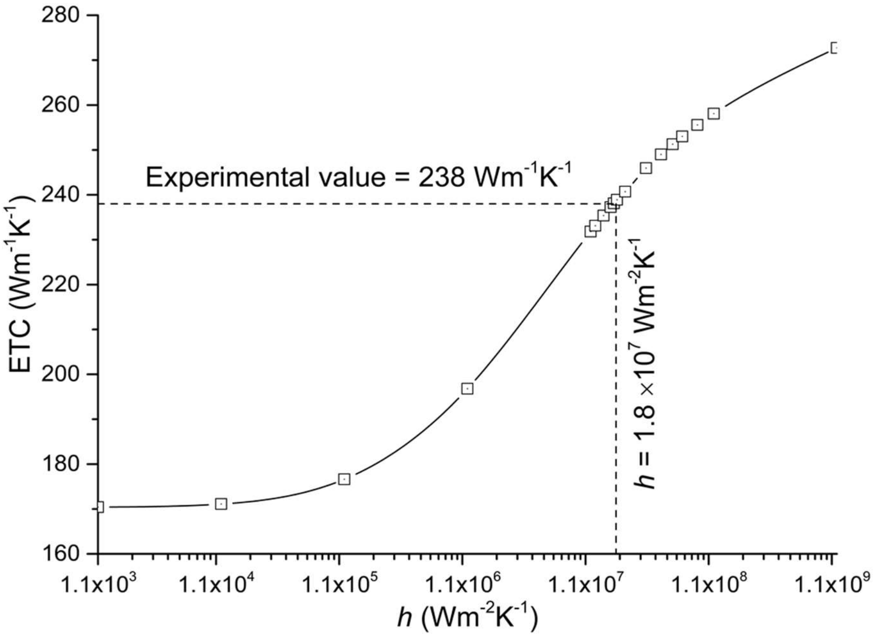

Figure 9. ETC of the 10 vol.% GFs/Al composite considering the interfacial thermal conductance (h) from 1.1×10^3 to 1.1×10^9 W m^{-2} K^{-1}.

To calculate the ETC of 10 vol.% GFs/Al composites using 2D image-based simulation, the orientations of GFs in the microstructures were corrected using Equation (9), and the TC of GFs was calculated using Equation (3-3). The TC of the Al matrix ($\lambda_{\text{Al-matrix}}$) was calculated using the following equation [15]:

$$\lambda_{\text{Al-matrix}} = \frac{1}{4}\Big[\lambda_p(3v_p - 1) + \lambda_{\text{Al}}(3v_{\text{Al}} - 1) + \Big(\big[\lambda_p(3v_p - 1) + \lambda_{\text{Al}}(3v_{\text{Al}} - 1)\big]^2 + 8\lambda_p\lambda_{\text{Al}}\Big)^{\frac{1}{2}}\Big] \quad \text{...... (3-10)}$$

where the TCs of the raw material Al powder (λ_{Al}) was taken as 228 W m^{-1} K^{-1} as in our previous works, TC of the pores (λ_p) was 0.214 W m^{-1} K^{-1}, volume fraction of Al (v_{Al}) was 0.994, and volume fraction of pores (v_p) was 0.006. The pores in this study were assumed to be embedded in the Al matrix. The $\lambda_{\text{Al-matrix}}$ was 226 W m^{-1} K^{-1}. Figure 3-9 shows the calculated ETC considering the interfacial heat conduction (h) from 1.1 × 10^3 to 1.1 × 10^9 W m^{-2} K^{-1}. When the calculated ETC was equal to the experimental ETC, h was 1.8 × 10^7 W m^{-2} K^{-1}. This value (1.8 × 10^7 W m^{-2} K^{-1}) was the same order of magnitude as the h given by Xue, Zhou, and Schmidt (4.5 ~ 5 × 10^7 W m^{-2} K^{-1}) [2, 8, 16]. Moreover, the calculated ETC was 250 W m^{-2} K^{-1} when h was in 4.5 ~ 5 × 10^7 W m^{-2} K^{-1}.

To view the Al-GFs interface (see Figure 3-10), pores can be observed. Additionally, Li [4], Zhou [5], and Huang [17] reported that an amorphous layer interface could be readily formed at the Al-GFs interface. Therefore, the small difference between h calculated in this work and h reported by Xue, Zhou, and Schmidt can be attributed to the pores and amorphous layer at the interface.

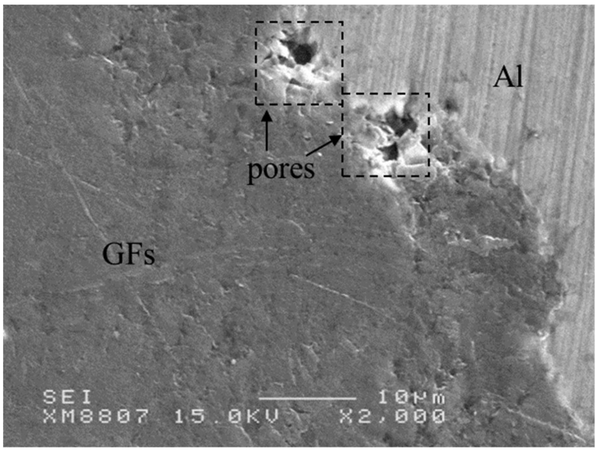

Figure 10. A SEM image of the microstructure at the Al-GFs interface.

3.4 Summary

This study aimed to calculate the ETC of GFs/Al composites using 2D image-based simulations. However, the ETC calculated from the microstructure images might not be equivalent to that measured using experimental methods. Because the 2D microstructure image cannot reveal the depth information related to the observation surface, the orientation of GFs in the 2D microstructure image differs from that of the experimental sample. Thus, we studied the relationships between the orientation of GFs in 2D cross-sectional images, the orientation of GFs in 3D models, and the aspect ratio of GFs in the 2D cross-sectional images.

The GFs in the modeled 3D models are elliptical cylinders. In light of the morphological characteristics of GFs, the conclusions of this study are limited to the study of the thermal conductivity of flake graphite reinforced aluminum matrix composites. GFs orientation was defined by the angle between GFs basal plane and heat flow direction in this study. Angles were marked as θ_{2D} in the 2D cross-section and θ_{3D} in the 3D model. Based on the research results, the following conclusions were drawn:

1) θ_{2D} was generally larger than θ_{3D}, and the difference between them could cause the TC error to be as high as 840 $Wm^{-1}K^{-1}$. No regularity was observed between the θ_{2D} and θ_{3D} differences.
2) The data for θ_{2D}, θ_{3D}, and aspect ratio were on a curved surface, and the curved surface function can be used to convert θ_{2D} into θ_{3D}. The difference between the actual θ_{3D} and θ_{3D} values calculated using the curved surface function was less than 6°.
3) The ETC of the 10 vol.% GFs/Al composite was evaluated using 2D image-based simulation, where the suggested converting θ_{2D} into θ_{3D} was employed.
4) The calculated interfacial thermal conductance was 1.8×10^7 W m^{-2} K^{-1}, and it is the same order of magnitude with the reference value ($4.5\sim5 \times 10^7$ W m^{-2} K^{-1}).

3.5 References

[1] Chen JK, Huang IS. Thermal properties of aluminum–graphite composites by powder metallurgy. Composites Part B: Engineering. 2013;44(1):698-703.

[2] Xue C, Bai H, Tao PF, Wang JW, Jiang N, Wang SL. Thermal conductivity and mechanical properties of flake graphite/Al composite with a SiC nano-layer on graphite surface. Materials & Design. 2016;108:250-8.

[3] Etter T, Schulz P, Weber M, Metz J, Wimmler M, Löffler JF, et al. Aluminium carbide formation in interpenetrating graphite/aluminium composites. Materials Science and Engineering: A. 2007;448(1-2):1-6.

[4] Li W, Liu Y, Wu G. Preparation of graphite flakes/Al with preferred orientation and high thermal conductivity by squeeze casting. Carbon. 2015;95:545-51.

[5] Zhou C, Ji G, Chen Z, Wang M, Addad A, Schryvers D, et al. Fabrication, interface characterization and modeling of oriented graphite flakes/Si/Al composites for thermal management applications. Materials & Design. 2014;63:719-28.

[6] Xue C, Bai H, Tao PF, Jiang N, Wang SL. Analysis on Thermal Conductivity of Graphite/Al Composite by Experimental and Modeling Study. Journal of Materials Engineering and Performance. 2016;26(1):327-34.

[7] Kurita H, Miyazaki T, Kawasaki A, Lu Y, Silvain J-F. Interfacial microstructure of graphite flake reinforced aluminum matrix composites fabricated via hot pressing. Composites Part A: Applied Science and Manufacturing. 2015;73:125-31.

[8] Zhou C, Huang W, Chen Z, Ji G, Wang ML, Chen D, et al. In-plane thermal enhancement behaviors of Al matrix composites with oriented graphite flake alignment. Composites Part B: Engineering. 2015;70:256-62.

[9] Gori F, Corasaniti S. Effective thermal conductivity of composites. International Journal of Heat and Mass Transfer. 2014;77:653-61.

[10] Wejrzanowski T, Grybczuk M, Chmielewski M, Pietrzak K, Kurzydlowski KJ, Strojny-Nedza A. Thermal conductivity of metal-graphene composites. Materials & Design. 2016;99:163-73.

[11] Czabaj MW, Riccio ML, Whitacre WW. Numerical reconstruction of graphite/epoxy composite microstructure based on sub-micron resolution X-ray computed tomography. Composites Science and Technology. 2014;105:174-82.

[12] Sugio K, Kono K, Choi YB, Sasaki G. Evaluation of Effective Thermal Conductivity of Metal Matrix Composites by Using Image-Based Calculation. Materials Science Forum: Trans Tech Publ; p. 1939-43.

[13] Sugio K, Choi Y-B, Sasaki G. Effect of the Interfacial Thermal Resistance on the Effective Thermal Conductivity of Aluminum Matrix Composites. Materials Transactions. 2016;57(5):582-9.

[14] Kelly B. Physics of Graphite (Applied Science. London/New Jersey. 1981:267.

[15] Landauer R. The electrical resistance of binary metallic mixtures. Journal of Applied Physics. 1952;23(7):779-84.

[16] Schmidt AJ, Collins KC, Minnich AJ, Chen G. Thermal conductance and phonon transmissivity of metal–graphite interfaces. Journal of Applied Physics. 2010;107(10):104907.

[17] Huang Y, Ouyang Q, Guo Q, Guo X, Zhang G, Zhang D. Graphite film/aluminum laminate composites with ultrahigh thermal conductivity for thermal management applications. Materials & Design. 2016;90:508-15.

Chapter 4

Effect of the orientation of GFs and interfacial thermal resistance on the effective thermal conductivity of GFs/Al composites

4.1 Introduction

Graphite flakes (GFs) have excellent thermal properties, including high thermal conductivity (TC) and low coefficient of thermal expansion (CTE). In the basal plane, GFs TC and CTE are 2800 W m^{-1} K^{-1}[1-4] and -1.5 ppm K^{-1} [5, 6], respectively. Therefore, GFs/Al composites have attracted much attention from researchers of thermal management materials. Many experimental and theoretical studies have been conducted to study the effective thermal conductivities of GFs/Al composites. GFs/Al composites exhibit high effective thermal conductivities [7-20], e.g., Chen et al.[7] reported that the ETC of 80 vol.% GFs/Al composites (783 W m^{-1} K^{-1}) was higher than that of 80 vol.% diamond/copper composites (724 W m^{-1} K^{-1}). Li et al. [14] reported that the ETC of 70 vol.% GFs /Al composite was 714 W m^{-1} K^{-1} in the plane parallel to the GFs layers.

However, the past studies [7, 11, 19, 21-23] also revealed that the ETCs of GFs/Al composites were affected by the orientation of GFs, interfacial thermal resistance, and interface reaction. The ETCs of GFs/Al composites are not as high as the expected theoretical values. The TCs of GFs are significant anisotropy, and its TC in the out-plane is 38 W m^{-1} K^{-1} [3, 4, 12]. The anisotropic TC of GFs causes its orientation to influence the ETC of GFs/Al composites greatly. Moreover, it is almost impossible to control perfectly the orientation of GFs; thus, the orientations of GFs may be diverse in composites. On the other hand, the interfacial thermal resistance at the Al-GFs interface may be anisotropic due to the anisotropic crystal structure of GFs. Therefore, if the orientations of GFs in composites cannot be obtained, it would be difficult to calculate the effects of the orientation of GFs and the interfacial thermal resistance on the ETC using theoretical models, such as the rule of mixture [24, 25], Fricke model [26], Nan model and effective medium approximation (EMA) approach [27].

The interface reaction is a chemical reaction. Al_4C_3 [10, 21, 28, 29] and amorphous layers [9, 14, 17] are easily formed at the Al-GFs interface. Al_4C_3 phase is brittle and harmful for the bonding between Al and GFs. Meanwhile, Al_4C_3 has low TC and can hinder the heat transfer in the Al-GFs interface [7, 11, 21]. Fortunately, some approaches can suppress the interface reaction while fabricating the GFs/Al composites. The approaches include lowing the sintering temperature [7, 13, 17, 19] or reducing the reaction time [9, 21, 30, 31], or adding Si or SiC particles to the starting materials [8, 9, 12, 13, 15, 19], etc. Besides, the amorphous layer at the Al-GFs interface may act as the nucleation site for Al_4C_3 [32]. The amorphous layer thus can also hinder the heat transfer itself [9, 33].

Therefore, in this chapter, 10~20 vol.% GFs/Al composites were prepared. two-dimensional(2D) image-based simulation method [34] is used to calculate the ETC of GFs/Al composites considering the effect of the orientations of GFs and the interfacial thermal resistance. In addition, the interfacial thermal resistances in the in-plane and the out-of-plane of GFs were calculated.

4.2 Experimental and calculation procedures

4.2.1 Experiments

Al powder (99.9%, 30 *μ*m in diameter) and GFs (98%, average particle size: 137.02 *μ*m) were used. The nominal TC of the Al powder was 236 W m^{-1} K^{-1}, while that of GFs was 880 and 38 W m^{-1} K^{-1} at the basal-plane and out-of-plane directions, respectively. Al powders were mixed with 10 vol.% and 20 vol.% of GFs, respectively. Subsequently, appropriate amounts of alumina balls were added through a wet process for 2 *h* using a V-type mixer at 50 rpm. Then, spark plasma sintering (SPS) was conducted at 873 K and 60 MPa pressure for 0.5 h under a vacuum of 1.3 × 10^{-2} Pa. In order to avoid the interface reaction between Al and GF, the sintering temperature was maintained lower than the melting point of Al. The temperature was raised by 200 K/min: one pure Al sample, 10 vol.% GF/Al (Samples 1-2), and 20 vol.% GF/Al (Samples 3-4) composites were fabricated. Figure 4-1 depicts the shape of the samples sintered using SPS.

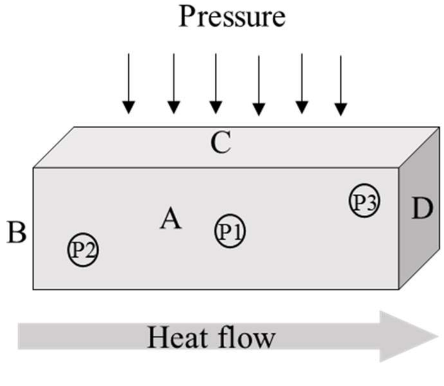

Figure 4-1. Shape of the sample sintered by SPS; P1, P2, and P3 at the A plane denote the regions that correspond to the optical micrographs. The grey arrow illustrates that the heat flow was from B to D during ETC measurement, C is the plane bearing the pressure during sintering.

The microstructure images of the sintered samples were obtained via optical microscopy from the P1, P2, and P3 regions on A plane in Figure 4-1. The relative densities of the sintered samples were measured using the Archimedes method. ETCs of the sintered samples were measured at 25 °C using a steady-state thermal-conductivity device.

4.2.2 Numerical methods

2D image-based simulations were performed in two steps. First, the ETCs of composites were calculated considering the effect of the orientations of GFs. Then, ETCs of the composites were calculated considering the orientations of the GFs and the interfacial thermal resistance at the Al-GFs interface. The obtained microstructure images of the experimental samples were used to perform 2D image-based simulations.

4.2.2.1 Temperature distribution

We calculated 2D-temperature distributions using the finite volume method as follows:

$$T_{x,y}^{n+1} = T_{x,y}^{n} + \frac{\Delta t}{\rho c}\left(\frac{q_{x+1,y}^{n} - q_{x-1,y}^{n} q_{x-1,y}}{\Delta x} + \frac{q_{x,y+1}^{n} - q_{x,y-1}^{n}}{\Delta y}\right)$$

…… (4-1)

where *x* and *y* denote the coordinate positions of the element, $T_{x,y}^{n}$ is the temperature of element at (*x*, *y*) coordinates, and $T_{x,y}^{n+1}$ is the element's temperature at (*x*, *y*) coordinates after a time $\triangle t$, ρ is density, c is specific heat, $\triangle x$ and $\triangle y$ denote the sizes of elements along the *x*-axis and the *y*-axis, respectively, q^n denotes heat flow. When q^n is the heat conduction between adjacent elements (e.g., as depicted in Figure 4-2, q^n moves from the E to adjacent elements M or N), q^n can be calculated as follows:

$$q_{x+1,y}^{n} = \lambda_{x+\frac{1}{2},y}\left(\frac{T_{x+1,y}^{n} - T_{x,y}^{n}}{\triangle x}\right), \qquad q_{x-1,y}^{n} = \lambda_{x-\frac{1}{2},y}\left(\frac{T_{x,y}^{n} - T_{x-1,y}^{n}}{\triangle x}\right)$$

$$q^n_{x,y+1} = \lambda_{x,y+\frac{1}{2}}\left(\frac{T^n_{x,y+1}-T^n_{x,y}}{\Delta y}\right), \quad q^n_{x,y-1} = \lambda_{x,y-\frac{1}{2}}\left(\frac{T^n_{x,y}-T^n_{x,y-1}}{\Delta y}\right)$$

$$\lambda_{x+\frac{1}{2},y} = \frac{2\lambda_{x,y}\lambda_{x+1,y}}{\lambda_{x,y}+\lambda_{x+1,y}}, \quad \lambda_{x-\frac{1}{2},y} = \frac{2\lambda_{x,y}\lambda_{x-1,y}}{\lambda_{x,y}+\lambda_{x-1,y}}$$

$$\lambda_{x,y+\frac{1}{2}} = \frac{2\lambda_{x,y}\lambda_{x,y+1}}{\lambda_{x,y}+\lambda_{x,y+1}}, \quad \lambda_{x,y-\frac{1}{2}} = \frac{2\lambda_{x,y}\lambda_{x,y-1}}{\lambda_{x,y}+\lambda_{x,y-1}}$$

…… (4-2)

where $\lambda_{(x,\,y)}$ denotes the TC of element at (x, y) coordinates, $\lambda_{(x+1,y)}$, $\lambda_{(x-1,y)}$, $\lambda_{(x,y+1)}$, and $\lambda_{(x,y-1)}$ denote the TC of elements adjacent to (x, y), and $\lambda_{(x+1/2,y)}$, $\lambda_{(x-1/2,y)}$, $\lambda_{(x,y+1/2)}$, and $\lambda_{(x,y-1/2)}$ denote the harmonic mean of TC.

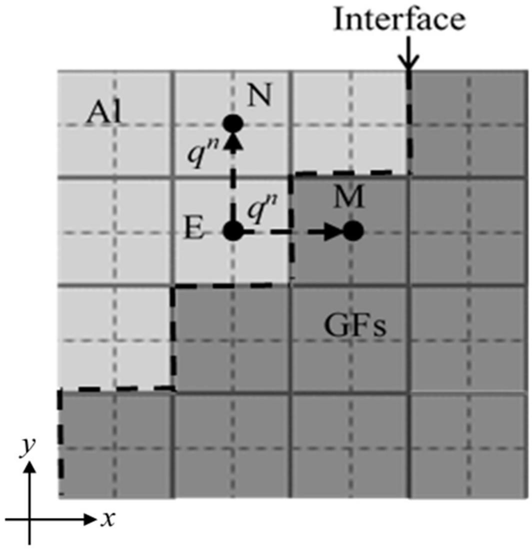

Figure 4-2. Schematic diagram of heat flow at the interface. The dashed line denotes the Al–GF interface, q^n denotes the heat flow in the direction of the dashed arrows.

Considering the effect of the interfacial thermal resistance in the composite, if q^n moves by heat transfer between different types of elements, the interfacial heat transfer coefficient (h) must be considered. For example, as depicted in Figure 4-2, considering that q^n moves from E to M and through the interface between Al and GFs (Al-GF), q^n can be calculated as follows:

$$q_{x+1,y}^{n} = h(T_{x+1,y}^{n} - T_{x,y}^{n}), \qquad q_{x-1,y}^{n} = h(T_{x,y}^{n} - T_{x-1,y}^{n})$$

$$q_{x,y+1}^{n} = h(T_{x,y+1}^{n} - T_{x,y}^{n}), \qquad q_{x,y-1}^{n} = h(T_{x,y}^{n} - T_{x,y-1}^{n})$$

…… (4-3)

4.2.2.2 Calculation of effective thermal conductivity

As depicted in Figure 4-3, the simulation model is comprised of two heat sources and composite components. The top and bottom surfaces correspond to the periodic boundary, while the left and right sides correspond to the adiabatic boundary. The composite part is based on the microstructure images of Samples 1–4. Therefore, the size of the composite part ($N_x \times N_y$) was 450 × 600 elements for Samples 1, 2, and 4, and it was 570 × 450 elements for Sample 3. The heat source size was 5 × 600 elements for Samples 1, 2, and 4, and it was 5 × 450 elements for sample 3 ($N_L = N_R =$ 5 elements). The size of each element was 1.18×10^{-6} m. The initial TC of the GFs was set to be (880, 38) W m^{-1} K^{-1} in the (x, y) directions.

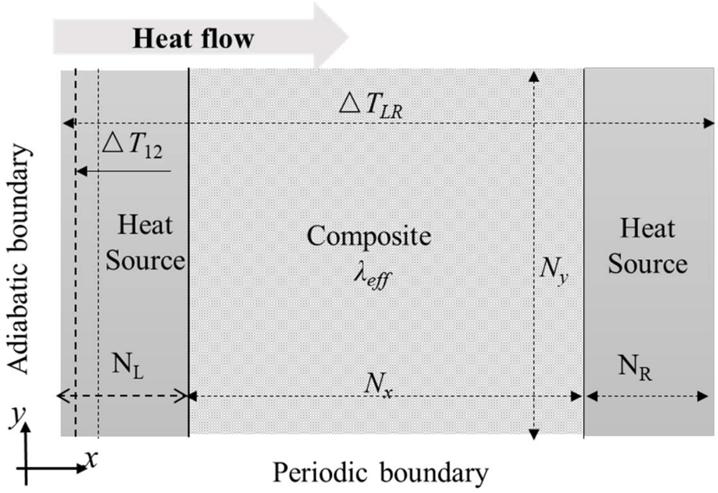

Figure 4-3 Simulation model for the ETC calculation.

The temperature of the left edge elements was set to 301 K, and the initial temperature of the other elements was set to 300 K. The temperatures at the left and right sides were fixed. The temperature of the remaining elements was iterated until the temperature variation was lower than 10^{-13} K, and the temperature distribution in the steady-state was obtained. The ETC values of the GF/Al composites, $\lambda_{\text{s-eff}}$, were calculated when the temperature distribution was in the steady-state, as follows:

$$\lambda_{s-eff} = \frac{\lambda_{Al-e} \quad \triangle T_{12} N_x}{\triangle T_{LR} - N_L \triangle T_{12} - N_R \triangle T_{12}}$$

…… (4-4)

where $\lambda_{Al\text{-}eff}$ denotes the TC of the Al matrix considering the effect of pores, and $\triangle T_{12}$ is the average temperature difference between the first and the second columns; N_L and N_R denote the numbers of elements in the heat sources, N_x and N_y are the numbers of elements in the composite region.

4.2.2.3 Thermal conductivity of GFs

This study used an angle (θ) between the basal plane of GFs and the direction of heat flow to characterize the GFs' orientation in composites. Thus, by using the following equation (4-5) [18], the TC of GFs can be calculated along the direction of the basal plane of GFs parallel ($\lambda_{//}$) and perpendicular ($\lambda_{\perp}$) to the heat flow direction.

$$\lambda_{//} = \lambda_a \left[1 - (1 - \frac{\lambda_c}{\lambda_a}) sin^2\theta\right]$$
$$\lambda_{\perp} = \lambda_a \left[1 - (1 - \frac{\lambda_c}{\lambda_a}) cos^2\theta\right]$$

…… (4-5)

where λ_a and λ_c are the TC in the basal-plane and the out-of-plane directions of GFs, respectively.

Figure 4-4 illustrates the relationship between the TC of GFs and the angle θ. It can be observed that TC decreased significantly from 880 to 38 W m^{-1} K^{-1} when the angle increased from 0° to 90°, revealing that the orientation of the GFs significantly affects the ETC of composites. In addition, Figure 4-4 shows that the TC of GFs was lower than that of the Al matrix (236 W m^{-1} K^{-1}) if the angles were greater than 61°, indicating that the ETC of composites could be enhanced at critical angles smaller than or equal to 61°.

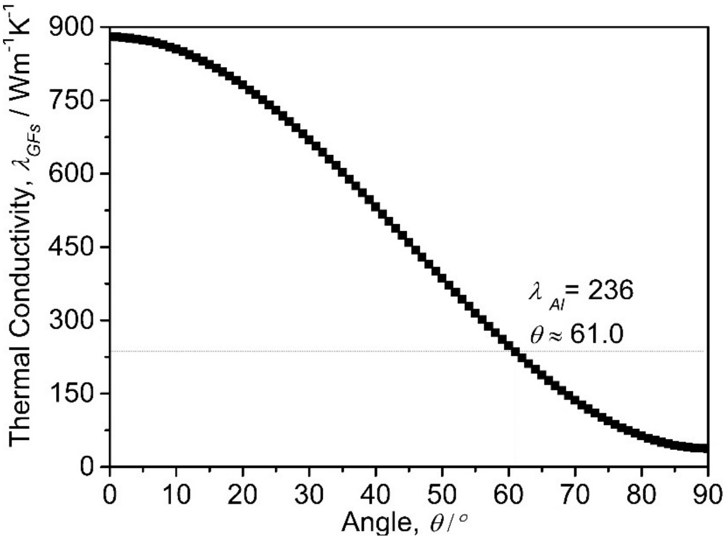

Figure 4-4 TC of GFs as a function of angle (θ). The nominal TC of Al matrix, λ_{Al}, was 236 W m^{-1} K^{-1} (gray horizontal dotted line).

4.2.2.4 Interfacial thermal resistance

The interfacial thermal conductance in the in-plane and the out-of-plane may be different due to the anisotropic crystal structure of GFs. Thus, the interfacial thermal conductance, *h*, at the Al-GFs interface was calculated by the DMM method. *h* can be calculated as follows:

$$h = \frac{\hbar^2}{8\pi^2 K T^2} \sum_j \left[\frac{1}{v_{1,j}^2\, v_{2,j}^2 (v_{1,j}^{-2} + v_{2,j}^{-2})} v_{1,j} \int_0^{\omega_{1,j}^c} \frac{\omega^4 e^{\frac{\hbar\omega}{KT}}}{\left(e^{\frac{\hbar\omega}{KT}} - 1\right)^2} d\omega \right] \qquad \text{...... (4-6)}$$

where $\hbar$ is Planck's constant, *K* is Boltzmann constant, *T* is temperature, ω is phonon angular frequency, and $\omega_{1,j}^c$ is the maximum phone angular frequency. The phono sound velocity, *v*, can be written as:

$$\sum_j v_j = v_L + 2v_T$$

$$v_L = \sqrt{\frac{E}{\rho} \cdot \frac{(1-\mu)}{(1+\mu)(1-2\mu)}}$$

$$v_T = \sqrt{\frac{E}{\rho} \cdot \frac{1}{2(1+\mu)}}$$

…… (4-7)

where v_L is longitudinal sound velocity, v_T is transverse sound velocity, E is Young's modulus, ρ is density, μ Poisson's ratio. The maximum phone angular frequency is calculated:

$$\omega_{1,j}^{c} = v_{1,j}\left(6\pi^2 \frac{\rho_1 N_A}{M_1}\right)^{\frac{1}{3}}$$

…… (4-8)

where N_A is Avogadro constant, M_1 is relative molecular mass. The material parameters are given in Table 4-3.

4.3 Results and discussion

4.3.1 Microstructures

Figure 4-5 illustrates the microstructures of the samples. The GFs were homogeneously distributed in the Al matrix. However, GFs' orientations were not uniform in the samples. As shown in Figures 4-5, the orientations of GFs were almost parallel to each other in Samples 1 and 4. However, GFs' orientations were partially disordered in Samples 2 and 3, forming different angles between GFs' basal-plane and heat flow direction. The orientations of GFs in Figures 4-5 were determined and shown in Figures 4-6. As depicted in Figures 4-6 (a), GFs were bounded by the smallest circumscribed rectangle, and the angle θ represents the orientation of GFs. The θ values in the microstructures were measured as depicted in Figure 4-6 (b), excluding GFs smaller than 5 × 5 pixels. The measured $|\theta|$ values were shown in Figure 4-6 (c)–(f). Most of the angles ranged from 0° to 30° in all the samples. Nevertheless, for the angles ranging between 50° and 90°, the relative frequency in Samples 1 and 4 was < 10%, while it was > 10% in Samples 2 and 3. Additionally, as depicted in Figures 4-4, the TC of GFs along the heat flow direction was smaller than that of the Al matrix when the angle was > 61.0°. Thus, it can be derived from Figure 4-6 that the average TCs of GFs in Samples 2 and 3 along the heat flow direction were smaller than the average TCs of GFs in Samples 1 and 4. Moreover, the average angle was calculated for each sample, as shown in Figure 4-6 (c)–(f).

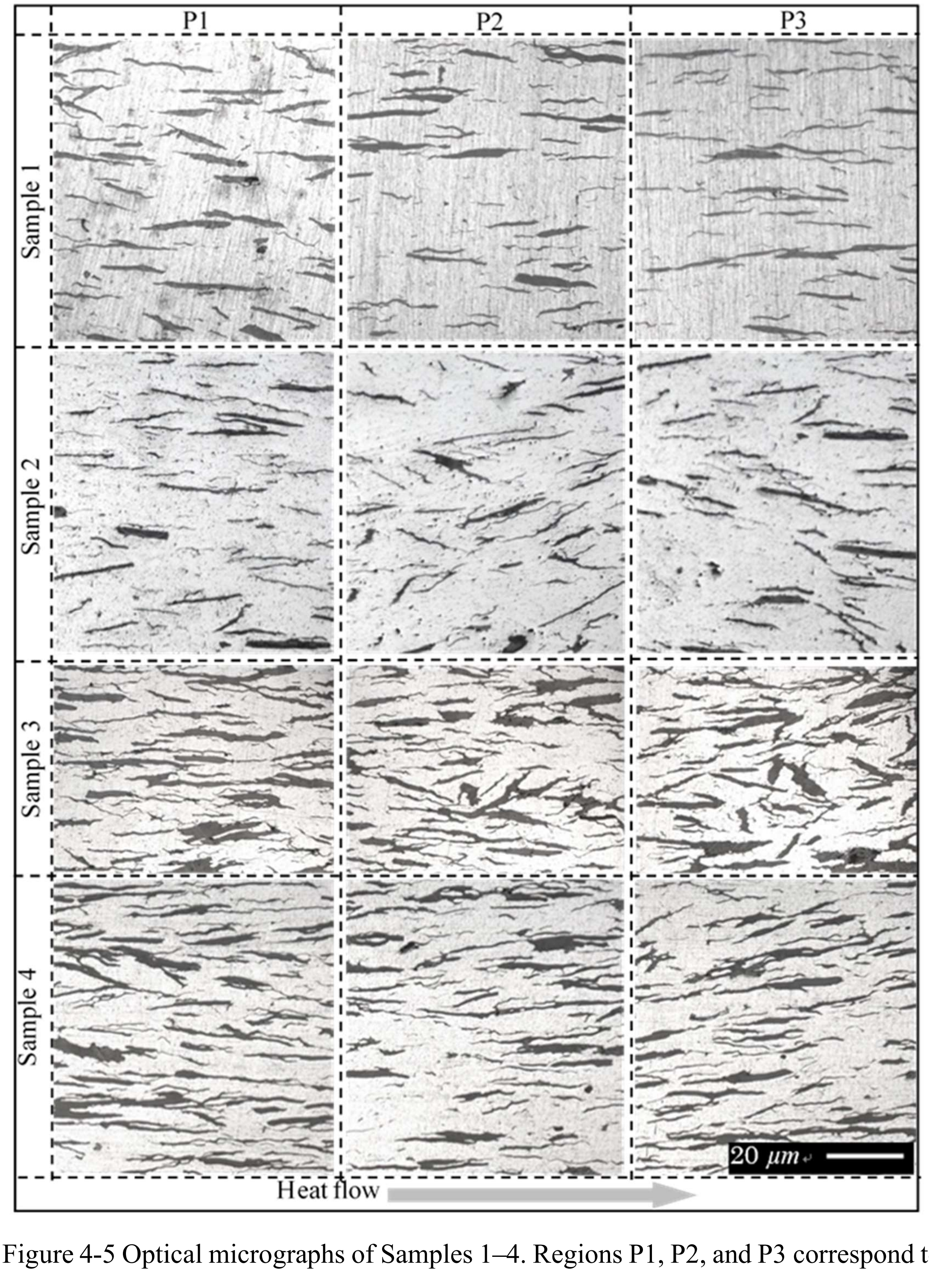

Figure 4-5 Optical micrographs of Samples 1–4. Regions P1, P2, and P3 correspond to the black circles at the A-plane in Figure 1. The gray arrow represents the heat flow direction during the ETC measurements. The brighter phases correspond to the Al matrix and the elongated dark phases to the GFs.

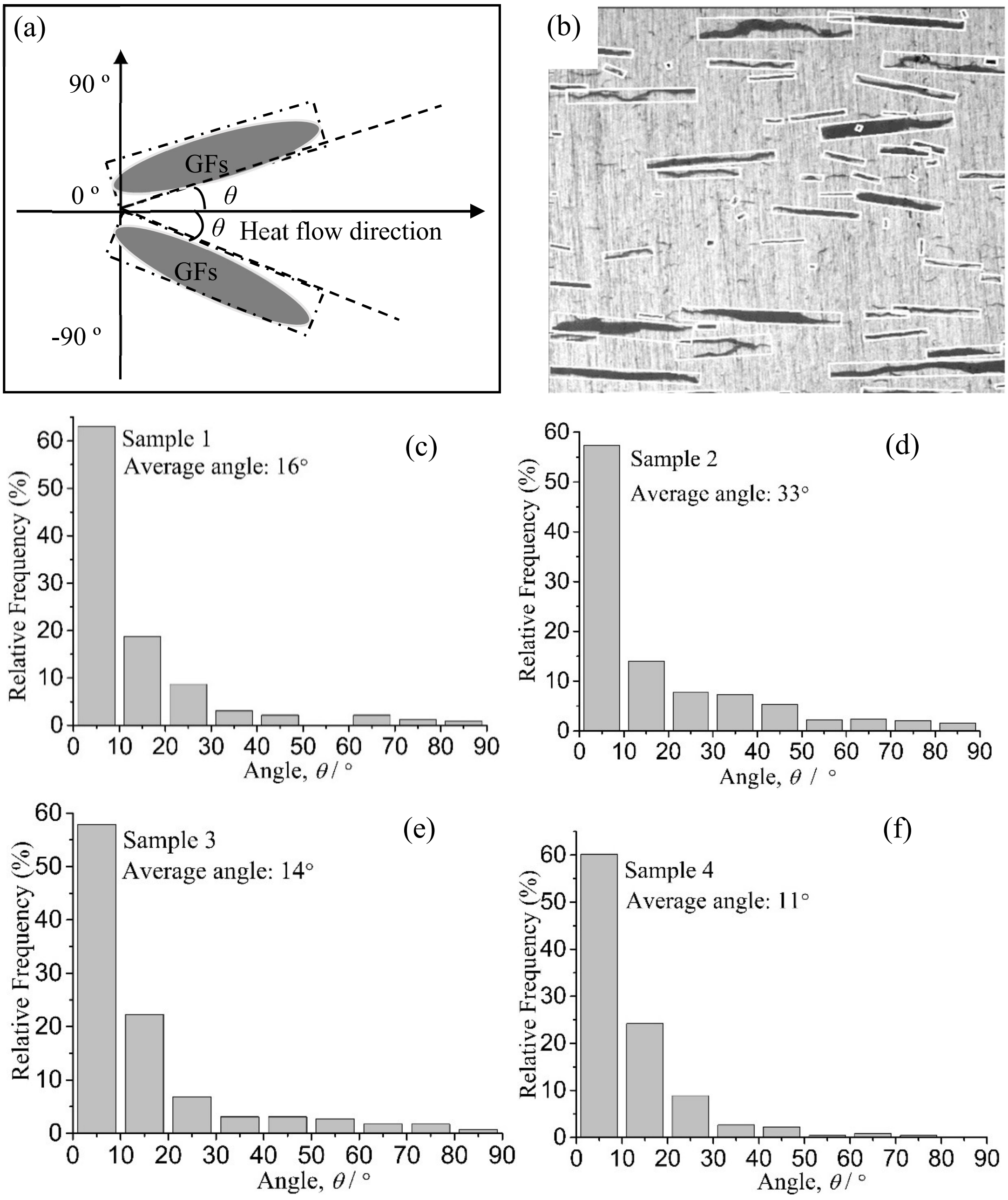

Figure 4-6 Distribution of the GF orientations in the Al matrix. Gray and white rectangles in (a) and (b) represent the smallest circumscribed rectangles and were used to measure the angle (θ) between the basal-plane of GFs and the heat flow direction; in case $-90° < \theta < 0°$, θ was taken as the absolute value.

4.3.2 Effect of porosity on TC of Al

The measured ETCs and the relative densities of the experimental samples were listed in Table 4-1. The ETC of Sample 1 was higher than that of Sample 2, and the ETC of Sample 3 was lower than that of Sample 4. These measurement results agree with the results shown in Figures 4-6.

Table 4-1 Volume fraction of GFs (v_{GFs}), measured ETCs (λ_{eff}), and relative densities of Samples 1–4 and pure Al sample.

Sample	v_{GFs}	λ_{eff}	Relative density
	%	$\mathrm{Wm^{-1}K^{-1}}$	
1	10	248	99.2%
2	10	238	99.4%
3	20	273	98.0%
4	20	280	99.3%
Al	0	217	97.0%

The measured relative density (Table 4-1) indicated that some pores existed in the composites. Therefore, in this study, the pores for all the samples were assumed to be in the Al matrix. The following equation derived by Landauer [35] was used to eliminate the pores' effect on the TC of Al-matrix:

$$\lambda_{Al-eff} = \frac{1}{4}\Big[\lambda_p\big(3v_p - 1\big) + \lambda_{Al}(3v_{Al} - 1) + \Big(\big[\lambda_p\big(3v_p - 1\big) + \lambda_{Al}(3v_{Al} - 1)\big]^2 + 8\lambda_p\lambda_{Al}\Big)^{\frac{1}{2}}\Big] \quad \text{...... (4-9)}$$

where $\lambda_{Al\text{-}eff}$ denotes the TC of Al matrix, λ_{Al} and λ_p are the TCs of the raw material Al powder and pores, respectively, v_{Al} is the volume fraction of Al, and v_p is the volume fraction of the pores. In addition, v_{Al}, $\mathrm{v_p}$, and λ_p are listed in Table 4-2. First, the measured TC of the pure Al sample ($\lambda_{Al\text{-}eff}$, 217 W m^{-1} K^{-1}) and its relative density (97%) were substituted in equation (4-9), and λ_{Al} was determined to be 228 W m^{-1} K^{-1}, as shown in Table 4-2. Second, the TCs of the Al-matrix for Samples 1–4, $\lambda_{Al\text{-}eff}$, were calculated by substituting v_{Al}, v_p, λ_p, and λ_{Al} from Table 4-2 in equation (4-9). The calculated values of $\lambda_{Al\text{-}eff}$ are 225.3, 225.9, 221.2, and 225.6 W m^{-1} K^{-1} for Samples1–4, respectively. The ETCs (λ_{ROM}) of Samples 1–4 were calculated using the rule of mixture (*ROM*), i.e., $\lambda_{ROM} = (v_{GFs})(\lambda_{GFs}) + (1-v_{GFs})(\lambda_{Al\text{-}eff})$, where the orientations of all the GFs were assumed to be aligned with the heat flow direction in the composites. The TC of the GFs (λ_{GFs}) was set to 880 W m^{-1} K^{-1} along the heat flow direction. The values of λ_{ROM} were 291, 291, 353, and 357 Wm^{-1}K^{-1} for Samples 1–4, respectively. The calculated λ_{ROM} was considerably higher than the measured ETC. Furthermore, We performed 2D image-based simulations to confirm the effect of the orientation of GFs on the ETC of composites.

Table 4-2 Calculation parameters in equation (10) and calculated effective thermal conductivities of composites.

Sample	v_{Al}	v_p	λ_p	λ_{Al}	$\lambda_{Al\text{-}eff}$	λ_{ROM}	$\lambda_{s\text{-}eff}$
			Wm^{-1}K^{-1}				
Al	0.97	0.03	0.214	228	217		
1	0.992	0.008	0.214		225.3	291	270
2	0.994	0.006			225.9	291	263
3	0.98	0.02			221.2	353	318
4	0.993	0.007			225.6	357	323

4.3.3 Effect of the orientation of GFs on the effective thermal conductivity

The TC values of GFs in the experimental samples were calculated using equation

(4-5), and Figure 4-7 illustrated the results. GFs were denoted in different colors according to the orientations of GFs in the Al matrix. When the orientation of GFs was parallel to the heat flow direction, GFs exhibited high TC, and they were marked in red.

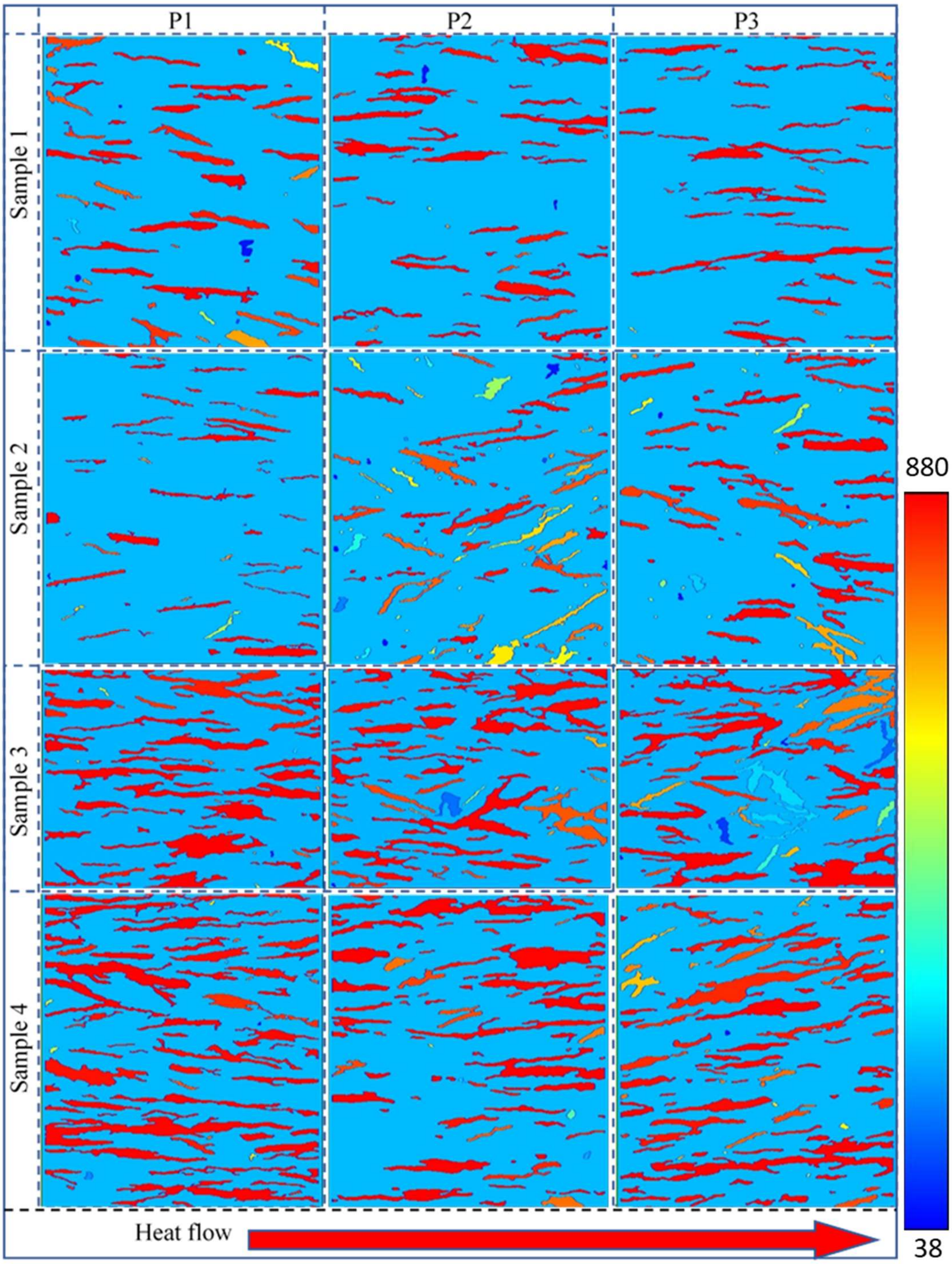

Figure 4-7 TC values of GFs in Samples1-4. Regions denoted as P1, P2, and P3 correspond to the microstructures in Figure. 5; The color bar shows the TCs of GFs in different orientations; The red arrow indicates the heat flow direction.

In contrast, if the GFs tilted from the heat flow direction, color changes indicated a decrease in TC. Figure 4-7 showed that most GFs were colored in red for Samples 1 and 4, which implied that GFs had a high TC, while the yellow, blue, and other colors appeared in the P2 and P3 regions for Samples 2 and 3. Table 4-2 listed the simulated ETCs ($\lambda_{s\text{-}eff}$) based on 2D image-based simulations. Figure 4-8 further compared the measured ETC, λ_{ROM}, and $\lambda_{s\text{-}eff}$ of Samples 1–4. The values of $\lambda_{s\text{-}eff}$ were smaller than those of λ_{ROM}, and the deviations between λ_{ROM} and $\lambda_{s\text{-}eff}$ for Samples1–4 were 7.2%, 9.6%, 9.9%, and 9.5%, respectively. Comparing the ETC loss in Samples1–4, the difference between Samples 1 and 2 in ETC loss was 2.4%, while it was only 0.4% between Samples 3 and 4. Those deviations may be explained by the angle deviations depicted in Figure 4-6 (c)-(f), where the angle difference between samples 1 and 2 was 17°, and between samples 3 and 4 was 3°. Furthermore, compared the $\lambda_{s\text{-}eff}$ values and the measured ETC values, the deviations between $\lambda_{s\text{-}eff}$ and the measured ETCs were 8.1%, 9.5%, 14.2%, and 13.3% for Samples1–4, respectively. These deviations can be attributed to the effect of the interfacial thermal resistance between Al and GFs.

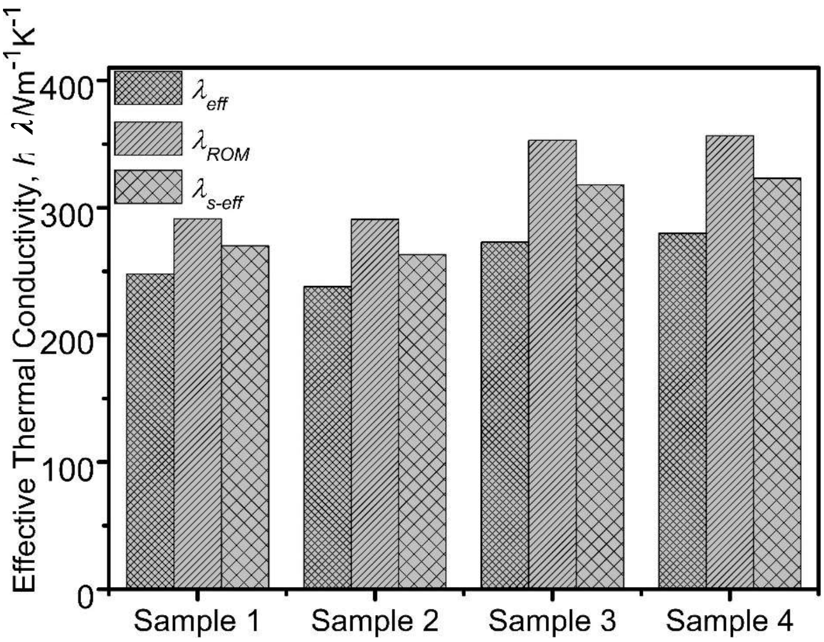

Figure 4-8 ETCs of the composite samples. λ_{eff} denotes the measured ETC, λ_{ROM} is the ETC calculated using the rule of mixture, and $\lambda_{s\text{-}eff}$ is the ETC calculated using the 2D image-based simulation considering GF orientations.

4.3.4 Effect of interfacial thermal resistance on the effective thermal conductivity

A series of 2D image-based simulations were performed to study further the effect of the interfacial thermal resistance on the ETC of the composites. The heat transfer coefficient, *h*, ranged from 10^3 to 10^9 W m^{-2} K^{-1} at the Al–GF interface. Figure 4-9 illustrated ETC values as a function of *h* for composites.

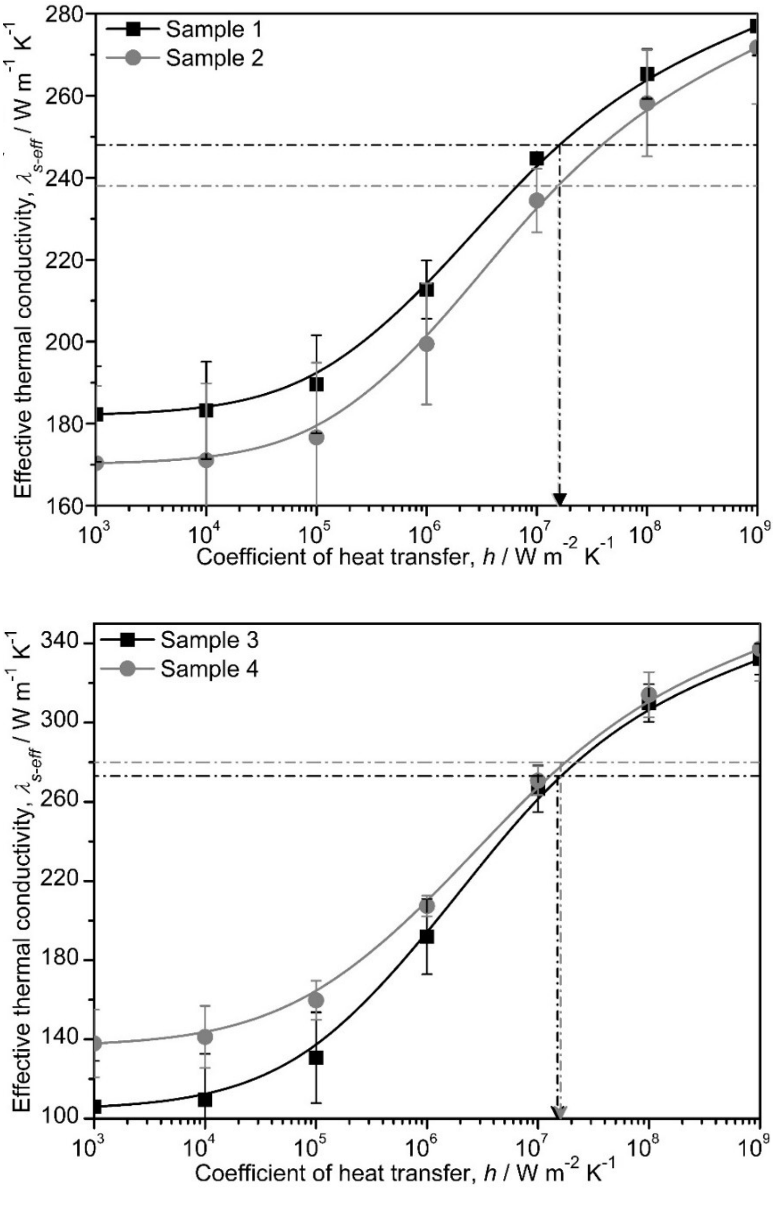

Figure 4-9 ETC as a function of the heat transfer coefficient, *h*. The dashed lines represent the experimental ETCs and the arrows denote the *h* value at the Al-GF interface.

The ETC curve was similar to KJMA [36] equation, and ETC values rapidly increased as *h* increased from 10^5 to 10^9. Moreover, the ETC curves for Sample 1 and Sample 2 did not overlap in the *h* value range between 10^3 and 10^9, further proving that the orientations of GFs affected the composite ETC significantly. In Figure 4-9, the dashed lines represented the experimental ETC, and the arrows denoted the heat transfer coefficients (*h*) at the Al-GF interface. Table 4-3 showed the *h* values evaluated via inverse analysis, and the values showed the same order of magnitude for all samples, i.e., 10^7. Moreover, a reference value of *h* calculated using the AMM model was listed in Table 4-3. The order of magnitude of the reference value is also 10^7, and the minor differences between the *h* reference value and the simulated *h* for Samples 1–4 can be attributed to the misfits at the interface. However, the values of *h* calculated by DMM were 1.1×10^8 $\mathrm{Wm^{-2}K^{-1}}$ in the in-plane and 1.32×10^9 $\mathrm{Wm^{-2}K^{-1}}$ in the out-of-plane. Thus, the values were greater than the simulated *h*.

Table 4-3 Material parameters of the DMM calculation[37], interfacial thermal conductance (*h*), and interfacial thermal resistance (*R*); Sim. is the simulated *h* using 2D-image, Cal. is calculated *h* using DMM method, Ref. is the reference value of *h*.

Sample		*T*	*E*	*P*	μ	M_1	*h* / 10^7 $\mathrm{Wm^{-2}K^{-1}}$			*R / 10^{-8}*
		(*K*)	(GPa)	(g/cm^3)			*Sim.*	*Cal.*	*Ref.*	$\mathrm{m^2KW^{-1}}$
Al	/		70.0	2.7	0.3	27				
GFs	In-plane	300	1153.0	2.2	0.195	12		11	4.8[19]	
	Out-of-plane		39.511	2.2	0.0002	12		130		
1							1.62			6.17
2							1.56			6.41
3							1.64			6.10
4							1.78			5.62

The interfacial thermal resistance, R, is the reciprocal of heat transfer coefficient, i.e., $R = 1 / h$, R values for Samples 1–4 were listed in Table 4-3. It should be noted that R values were sufficiently small and even negligible. However, as shown in Figure 4-8, R affected the ETC of the composites significantly, leading to a significant decrease in ETC. The reason can be attributed to the considerable number of interfaces formed in the GF/Al composites.

4.4 Summary

10 vol.% GF/Al and 20 vol.% GF/Al composites were fabricated via SPS. The microstructures images of the composites were observed, and their relative density and ETCs were measured. The measured ETC values were 248, 238, 273, and 280 W m^{-1} K^{-1} for Samples 1–4, which were smaller than the ETCs calculated through the *ROM* (291, 291, 353, and 357 W m^{-1} K^{-1}, for Samples 1–4, respectively).

The average angles of the GFs with respect to the heat flow direction were calculated to be 16°, 33°, 14°, and 11° for Samples 1–4, respectively. The ETCs of composites considering the orientations of GFs were evaluated using 2D image-based simulations. Compared with the ETC calculated using *ROM*, the results showed that ETCs decreased due to the anisotropic TC of GFs by 7.2%, 9.6%, 9.9%, and 9.5% for Samples 1–4, respectively. Due to the interfacial thermal resistance effect, the ETCs decreased by 8.1, 9.5, 14.2, and 13.3% for Samples 1–4, respectively. The R values at the Al–GF interface were evaluated to be 6.17×10^{-8}, 6.41×10^{-8}, 6.10×10^{-8}, and 5.62×10^{-8} W m^{-2} K^{-1} for Samples 1–4, respectively.

4.5 References

[1] Smith AW, Rasor NS. Observed Dependence of the Low-Temperature Thermal and Electrical Conductivity of Graphite on Temperature, Type, Neutron Irradiation, and Bromination. Physical Review. 1956;104(4):885-91.

[2] Zhou S, Chiang S, Xu J, Du H, Li B, Xu C, et al. Modeling the in-plane thermal conductivity of a graphite/polymer composite sheet with a very high content of natural flake graphite. Carbon. 2012;50(14):5052-61.

[3] Inagaki M, Kaburagi Y, Hishiyama Y. Thermal management material: graphite. Advanced Engineering Materials. 2014;16(5):494-506.

[4] Dresselhaus MS, Dresselhaus G, Eklund PC. Science of fullerenes and carbon nanotubes: their properties and applications: Elsevier; 1996.

[5] Schapery RA. Thermal Expansion Coefficients of Composite Materials Based on Energy Principles. Journal of Composite Materials. 1968;2(3):380-404.

[6] Nelson J, Riley D. The thermal expansion of graphite from 15 c. to 800 c.: Part I. Experimental. Proceedings of the Physical Society. 1945;57(6):477.

[7] Chen JK, Huang IS. Thermal properties of aluminum–graphite composites by powder metallurgy. Composites Part B: Engineering. 2013;44(1):698-703.

[8] Zhou C, Huang W, Chen Z, Ji G, Wang ML, Chen D, et al. In-plane thermal enhancement behaviors of Al matrix composites with oriented graphite flake alignment. Composites Part B: Engineering. 2015;70:256-62.

[9] Zhou C, Ji G, Chen Z, Wang M, Addad A, Schryvers D, et al. Fabrication, interface characterization and modeling of oriented graphite flakes/Si/Al composites for thermal management applications. Materials & Design. 2014;63:719-28.

[10] Prieto R, Molina JM, Narciso J, Louis E. Fabrication and properties of graphite flakes/metal composites for thermal management applications. Scripta Materialia. 2008;59(1):11-4.

[11] Ueno T, Yoshioka T, Ogawa J-i, Ozoe N, Sato K, Yoshino K. Highly thermal conductive metal/carbon composites by pulsed electric current sintering. Synthetic

Metals. 2009;159(21-22):2170-2.

[12] Prieto R, Molina JM, Narciso J, Louis E. Thermal conductivity of graphite flakes–SiC particles/metal composites. Composites Part A: Applied Science and Manufacturing. 2011;42(12):1970-7.

[13] Kurita H, Miyazaki T, Kawasaki A, Lu Y, Silvain J-F. Interfacial microstructure of graphite flake reinforced aluminum matrix composites fabricated via hot pressing. Composites Part A: Applied Science and Manufacturing. 2015;73:125-31.

[14] Li W, Liu Y, Wu G. Preparation of graphite flakes/Al with preferred orientation and high thermal conductivity by squeeze casting. Carbon. 2015;95:545-51.

[15] Zhou C, Chen D, Zhang XB, Chen Z, Zhong SY, Wu Y, et al. The roles of geometry and topology structures of graphite fillers on thermal conductivity of the graphite/aluminum composites. Physics Letters A. 2015;379(5):452-7.

[16] Amateau MF. Progress in the Development of Graphite- Aluminum Composites Using Liquid Infiltration Technology. Journal of Composite Materials. 2016;10(4):279-96.

[17] Huang Y, Ouyang Q, Guo Q, Guo X, Zhang G, Zhang D. Graphite film/aluminum laminate composites with ultrahigh thermal conductivity for thermal management applications. Materials & Design. 2016;90:508-15.

[18] Xue C, Bai H, Tao PF, Jiang N, Wang SL. Analysis on Thermal Conductivity of Graphite/Al Composite by Experimental and Modeling Study. Journal of Materials Engineering and Performance. 2016;26(1):327-34.

[19] Xue C, Bai H, Tao PF, Wang JW, Jiang N, Wang SL. Thermal conductivity and mechanical properties of flake graphite/Al composite with a SiC nano-layer on graphite surface. Materials & Design. 2016;108:250-8.

[20] Chang J, Zhang Q, Lin Y, Wu G. Layer by layer graphite film reinforced aluminum composites with an enhanced performance of thermal conduction in the thermal management applications. Journal of Alloys and Compounds. 2018;742:601-9.

[21] Etter T, Schulz P, Weber M, Metz J, Wimmler M, Löffler JF, et al. Aluminium carbide formation in interpenetrating graphite/aluminium composites. Materials

Science and Engineering: A. 2007;448(1-2):1-6.

[22] Tjong SC. Recent progress in the development and properties of novel metal matrix nanocomposites reinforced with carbon nanotubes and graphene nanosheets. Materials Science and Engineering: R: Reports. 2013;74(10):281-350.

[23] Wu S, Li TX, Yan T, Dai YJ, Wang RZ. High performance form-stable expanded graphite/stearic acid composite phase change material for modular thermal energy storage. International Journal of Heat and Mass Transfer. 2016;102:733-44.

[24] Truong H, Zinsmeister GE. Experimental study of heat transfer in layered composites. International Journal of Heat and Mass Transfer. 1978;21(7):905-9.

[25] Progelhof R, Throne J, Ruetsch R. Methods for predicting the thermal conductivity of composite systems: a review. Polymer Engineering & Science. 1976;16(9):615-25.

[26] Fricke H. A Mathematical Treatment of the Electric Conductivity and Capacity of Disperse Systems I. The Electric Conductivity of a Suspension of Homogeneous Spheroids. Physical Review. 1924;24(5):575-87.

[27] Nan C-W, Birringer R, Clarke DR, Gleiter H. Effective thermal conductivity of particulate composites with interfacial thermal resistance. Journal of Applied Physics. 1997;81(10):6692-9.

[28] Lin RY. Interface Evolution in Aluminum Matrix Composites During Fabrication. Key Engineering Materials. 1995;104-107:507-22.

[29] Liu ZY, Xiao BL, Wang WG, Ma ZY. Singly dispersed carbon nanotube/aluminum composites fabricated by powder metallurgy combined with friction stir processing. Carbon. 2012;50(5):1843-52.

[30] Leng J, Wu G, Zhou Q, Dou Z, Huang X. Mechanical properties of SiC/Gr/Al composites fabricated by squeeze casting technology. Scripta Materialia. 2008;59(6):619-22.

[31] Etter T, Kuebler J, Frey T, Schulz P, Löffler JF, Uggowitzer PJ. Strength and fracture toughness of interpenetrating graphite/aluminium composites produced by the indirect squeeze casting process. Materials Science and Engineering: A. 2004;386(1-2):61-7.

[32] Khalid FA, Beffort O, Klotz UE, Keller BA, Gasser P. Microstructure and interfacial characteristics of aluminium–diamond composite materials. Diamond and Related Materials. 2004;13(3):393-400.

[33] Kim KT, Cha SI, Gemming T, Eckert J, Hong SH. The role of interfacial oxygen atoms in the enhanced mechanical properties of carbon-nanotube-reinforced metal matrix nanocomposites. Small. 2008;4(11):1936-40.

[34] Sugio K, Choi Y-B, Sasaki G. Effect of the Interfacial Thermal Resistance on the Effective Thermal Conductivity of Aluminum Matrix Composites. Materials Transactions. 2016;57(5):582-9.

[35] Landauer R. The electrical resistance of binary metallic mixtures. Journal of Applied Physics. 1952;23(7):779-84.

[36] Sugio K, Tatsuno S, Fukushima H, Yanagisawa O. Modification of Kolmogorov-Johnson-Mehl-Avrami Equation for Clustered Nucleation. Materials Transactions. 2009;50(6):1563-71.

[37] Cho J, Luo J, Daniel I. Mechanical characterization of graphite/epoxy nanocomposites by multi-scale analysis. Composites science and technology. 2007;67(11-12):2399-407.

Chapter 5

Conclusions

Graphite flake reinforced aluminum matrix composites (GFs/Al composite) are lightweight, low cost, and exhibit outstanding thermal conductivity and low coefficient of thermal expansion. Especially for the excellent thermal conductivity, GFs/Al composites have been proposed as one of the most promising electronic packaging materials.

Lots of studies have been carried out to explore the thermal properties of GFs/Al composites. However, past studies reported that the high thermal conductivity of GFs could not be fully displayed in the GFs/Al composites. The effective thermal conductivity of GFs/Al composites was influenced by the volume fraction, dispersion, size, orientation of GFs, interface reaction, and interface thermal resistance, in particular the orientation of GFs and the interfacial thermal resistance. Unfortunately, until today, no method has been proposed to control the orientation of GFs well, and the theoretical models such as mixture rules, Maxwell, Fricke, Every, Nielsen, and the effective medium approximation cannot be considered the effect of the orientation of GFs. Moreover, interface thermal resistance seems to be an inherent property of carbon materials reinforced metal-matrix composites, and the value of interface thermal resistance is affected by the structure, composition, and state of the Al-GFs interface. AMM and DMM models are commonly used to calculate interface thermal resistance. However, the AMM and DMM models calculate the interface thermal resistance by assuming an ideal interface, but in reality, there may be gaps and lattice defects at the interface. Therefore, the interface thermal resistance evaluated by the AMM and DMM methods is not completely reliable.

This study aims to study the effective thermal conductivity of GFs/Al composites by two-dimensional image simulations, considering the orientation of GFs and the interface thermal resistance. The works were performed in three steps: first, 10-40 vol.% GFs/Al composites were prepared by spark plasma sintering. Moreover, we investigated the relative density of composites, orientation and distribution of GFs, interface reaction between Al and GFs, effective thermal conductivity, and thermal expansion coefficient of GFs/Al composites. Second, since the orientation of GFs in two-dimensional images may differ from that of GFs in three-dimensional images, some three-and two-dimensional models of GFs/Al composites were created to investigate the relationships between the orientations of GFs in three- and two-dimensional models. As a result, a fitted function was obtained to convert the two-dimensional orientation to three-dimensional orientation. Third, the effects of GFs' orientation and the interfacial thermal resistance on the effective thermal conductivities of GFs/Al composites were calculated by two-dimensional image simulations, and the interface thermal resistances at the Al-GFs interface were calculated by inverse analysis, AMM, and DMM methods. Through the above research, this thesis draws the following conclusions:

1) 10-40 vol.% GFs/Al composites were fabricated by spark plasma sintering; Most of the GFs were stacked by layers and parallel to each other in the composites; With GFs content up to 40%, GFs exhibit a state of aggregation and tends to form the network by connecting GFs; The formation of Al_4C_3 was absent in the 10-40 vol.% GFs/Al composites; The relative density was up to 99% for the GFs/Al composites; With GFs content up to 40%, the relative density of composites decreased to 97.1%. The measured effective thermal conductivities were 248, 280, 313, and 346 W m^{-1} K^{-1} for 10-40 vol.% GFs/Al composites, respectively; Due to the orientation of GFs and the interface thermal resistance, the experimental values of effective thermal conductivity of the GFs/Al composites were lower than the theoretical values. The experimental values of the coefficient of thermal expansion were 26.2, 24.4, 23.4, and 22.1 ppm/K for 10-40 vol.% GFs/Al composites, respectively. Moreover, because of the effects of the pores embedded in composites

and the disorder orientations of GFs, the experimental values for the composites with 10-20 vol.% GFs were higher than the calculated values perpendicular to GFs basal plane, and the experimental values exceeded even the coefficient of thermal expansion of Al and GFs (25 ppm/K along the direction perpendicular to the basal plane.

2) A small difference between the orientations can cause the difference in the thermal conductivity of GFs to be as high as 840 $Wm^{-1}K^{-1}$; The orientations of GFs in two-dimensional and three-dimensional images and two-dimensional aspect ratio of GFs have a strong correlation, and the correlation function can be obtained and use to convert the orientation of GFs from two-dimensional to three-dimensional. Moreover, the ETC of 10 vol% GFs/Al composite was evaluated using 2D image-based simulation and the correlation function. The results showed that the calculated ETC was equal to the experimental ETC 238 $W\ m^{-1}\ K^{-1}$ when the interfacial thermal conductance at the GFs-Al interface was $1.8 \times 10^7\ W\ m^{-2}\ K^{-1}$, and the calculated ETC was 250 $Wm^{-1}K^{-1}$ when the interfacial thermal conductance value was the same as that in a reference ($4.5 \sim 5 \times 10^7\ W\ m^{-2}\ K^{-1}$).

3) A two-dimensional image simulation code was developed to calculate the effective thermal conductivity of GFs/Al composites considering the effects of the orientation of GFs and interfacial thermal resistance; Orientations of GFs with respect to the heat flow direction were from 11° to 33° in 10-20 vol.% GFs/Al composites, and the orientation of GFs resulted in a loss of the effective thermal conductivity by7.2% to 9.9%. According to the DMM method, the interfacial thermal conductance at the Al-GFs interface was $1.1 \times 10^8\ W\ m^{-2}\ K^{-1}$ in the in-plane and $1.3 \times 10^9\ W\ m^{-2}\ K^{-1}$ in the out-plane. In contrast, the result ($1.1 \times 10^8\ W\ m^{-2}\ K^{-1}$ in the in-plane) was much larger than the result of two-dimensional image simulation ($1.56 \sim 1.78 \times 10^7\ Wm^{-2}K^{-1}$) and reference value ($4.8 \times 10^7\ Wm^{-2}K^{-1}$).

Acknowledgments

I would like to express my sincere gratitude to Assistant Professor Kenjiro Sugio for his guidance and insight throughout this study. He gave me full support in my research and life, which has played an important role in my professional and personal development. I am also greatly indebted to Professor Gen Sasaki and Assistant Professor Yongbum Chio. They gave me much positive help in the research, the accumulation of the knowledge, and my life, and I have learned much from them. In addition, I want to express my heartfelt thanks to Professor Kazuhiro Matsugi at Hiroshima University and Professor Jinku Yu at Yanshan University for their technical advice and experimental assistance. Finally, I would like to acknowledge the helpful comments and suggestions from Assistant Professor Zhefeng Xu.

Then, I would like to thank Mr. Lu Yang, Mr. Yongqiang Yao, Mr. Shaoming Kang, Mr. Fei Gao, Mr. Xilong Ma, and Mr. Yujiao Ke for their considerable assistance and help in my experiments. Moreover, I would like to thank all the past and present members of the Materials physics Laboratory in the Department of Mechanical Physical Engineering, Hiroshima University, for their enthusiastic help to my life and study.

Finally, my thanks would go to my beloved family for their loving considerations and great confidence in me all through these years. I also owe my sincere gratitude to my friends who gave me their help and time in helping me work out my problems during the challenging course of the thesis.

Published Papers in Regards to This Thesis

1. Yan Zhao, Kenjiro Sugio, Sasaki Gen, Zhefeng Xu, Jinku Yu. Evaluation of Effective Thermal Conductivity of Graphite Flake/Aluminum Composites by Two-Dimensional Image Simulation under a Correction Function. Material transactions, 62 (2021) 1625-1631. (Chapter 3)

2. Yan Zhao, Kenjiro Sugio, Yongbum Choi, Sasaki Gen, Zhefeng Xu, Jinku Yu. Effect of Anisotropic Thermal Conductivity of Graphite Flakes and Interfacial Thermal Resistance on the Effective Thermal Conductivity of Graphite Flakes/Aluminum Composites. Material transactions, 62 (2021) 98-104. (Chapter 4)

3. Yan Zhao, Kenjiro Sugio, Yong Bum Choi, Gen Sasaki and Jinku Yu. The relationship between the effective thermal conductivity and the orientation of graphite flakes in Al matrix composites. Processing of the 10th Pacific Rim International Conference on Advanced Materials and Processing (PRICM10). (2019) 815-820. (Chapter 4)

Presentations

1. Yan Zhao, Kenjiro Sugio, Yong Bum Choi, Gen Sasaki and Jinku Yu. Effect of Anisotropic Thermal Conductivity of Carbon Fiber in Aluminum Matrix Composite. 日本金属学会 2018年春期講演大会. March 19-21, 2018, Tokyo, Japan; Chiba Institute of Technology University.
2. Yan Zhao, Kenjiro Sugio, Yong Bum Choi, Gen Sasaki and Jinku Yu. The relationship between the effective thermal conductivity and the orientation of graphite flakes in Al matrix composites. The Tenth Pacific Rim International Conference on Advanced Materials and Processing (PRICM10). August 18-22, 2019, Xian, China, Qujiang International Conference Center.
3. Yan Zhao, Kenjiro Sugio, Sasaki Gen. Effect of anisotropic thermal conductivity and interfacial thermal resistance on the effective thermal conductivity of graphite flake/Al composites. 日本金属学会 2019 年秋期講演大会. September 11-13, 2019, Okayama, Japan; Okayama University Tsushima Campus.
4. Yan Zhao, Kenjiro Sugio, Sasaki Gen. Kenjiro Sugio, Sasaki Gen. Effect of anisotropic thermal conductivity and interfacial thermal resistance on the effective thermal conductivity of graphite flake/Al composites. 2018年12月 日本金属学会 日本鉄鋼協会 中国四国支部 第43回若手フォーラム 広島，日本.